Investigation of Optical Damage, Energy Partitioning

and Scaling Laws

at Extremely High Velocities

J.A.M. McDonnell

Unit for Space Sciences

University of Kent at Canterbury

Canterbury, Kent CT2 7NR

U.K.

Contract No. EOARD -93-0003

Contract Supervisor: Dr Firooz Allahdadi

REPORT DOCUMENTATION PAGE

Public reporting burden for this collection of information is estimated to average 1 hour per response, including the time for reviewing instructions, searching existing data sources, gathering and maintaining the data needed, and completing and reviewing the collection of information. Send comments regarding this burden estimate or any other aspect of this collection of information, including suggestions for reducing this burden, to Washington Headquarters Services, Directorate for information Operations and Reports, 1215 Jefferson Davis Highway, Suite 1204, Arlington, VA 22202-4302, and to the Office of Management and Budget, Paperwork Reduction Project (0704-0188), Washington, DC 20503.

1. AGENCY USE ONLY (Leave blank)	2. REPORT DATE	3. REPORT TYPE AND DATES COVERED
	Ocober 1994	Contract Report Aug 93–Aug 94

4. TITLE AND SUBTITLE

Investigation of Optical Damage, Energy Partitioning and Scaling laws

5. FUNDING NUMBERS

c

F49620-93-1-0487

6. AUTHOR(S)

J.A.M. McDonnell, P.R. Ratcliff, L. Kay, D.H. Niblett, M.J. Burchell

7. PERFORMING ORGANIZATION NAME(S) AND ADDRESS(ES)

University of Kent
Unit for Space Sciences
Physics Laboratory
Canterbury Kent
CT2 7NR

8. PERFORMING ORGANIZATION REPORT NUMBER

9. SPONSORING / MONITORING AGENCY NAME(S) AND ADDRESS(ES)

AFOSR/PKA
110 Duncan Avenue Suite B115
Bolling (202) 767-6836/ec

10. SPONSORING / MONITORING AGENCY REPORT NUMBER

TR-95-05

11. SUPPLEMENTARY NOTES

−

12a. DISTRIBUTION / AVAILABILITY STATEMENT

Approved for public release.
Distribution unlimited.

12b. DISTRIBUTION CODE

"A"

13. ABSTRACT (Maximum 200 words)

Optical damage assessment is presented from analysis of retrieved space damaged material (solar cell arrays); results, show a peak in the space environment damage effects in millimetre region and a dominance by meteoroids in this region. Impact damage features on glass will be folded with the results of the energy partitioning which derive from the unique 2 MV Van de Graaff facility achieving (in this report) velocities of up to 42 km sec^{-1}. Results from experimental campaigns incorporating simultaneous measurement of impact plasma, impact light flash and momentum enhancement provide new data on the fundamental features of energy partitioning in hypervelocity impacts phenomena such as ejecta momentum and kinetic energy, plasma and vapour production, and light flash energies. Hydrocode simulations are also described, which give insight into energy partitioning.

Results from a study of the impact light flash are presented which have proven principles of the prototype chamber design. Results which complement the energy partitioning data obtained from the plasma studies show readily the sensitivity of this technique as a study tool on the Van de Graaff facility.

14. SUBJECT TERMS

Hypervelocity Impact: Impact Morphology Optical damage;
Impact Plasma

15. NUMBER OF PAGES

109

16. PRICE CODE

n/a

17. SECURITY CLASSIFICATION OF REPORT	18. SECURITY CLASSIFICATION OF THIS PAGE	19. SECURITY CLASSIFICATION OF ABSTRACT	20. LIMITATION OF ABSTRACT
Unclassified	Unclassified	Unclassified	−

NSN 7540-01-280-5500

Standard Form 298 (Rev. 2-89)
Prescribed by ANSI Std. 239-18

TR-95-05

This report has been reviewed and is releasable to the National Technical Information Service (NTIS). At NTIS it will be releasable to the general public, including foreign nations.

This technical report has been reviewed and is approved for publication.

VICTORIA H. COX
Chief, Physics and BMD Coordinator

DONALD R. ERBSCHLOE, Lt Col, USAF
Chief, International Programs

TR-95-05

Investigation of Optical Damage, Energy Partitioning

and Scaling Laws
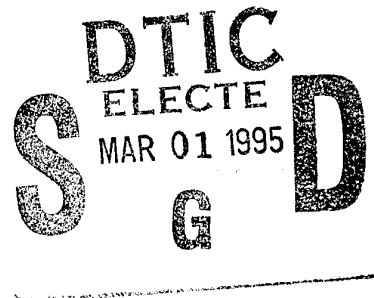
at Extremely High Velocities

J.A.M. McDonnell

Unit for Space Sciences

University of Kent at Canterbury

Canterbury, Kent CT2 7NR

U.K.

**DTIC
ELECTE
S MAR 01 1995
G D**

Contract No. EOARD -93-0003

Contract Supervisor: Dr Firooz Allahdadi

Accesion For		
NTIS CRA&I		☒
DTIC TAB		☐
Unannounced		☐
Justification		
By		
Distribution /		
Availability Codes		
Dist	Avail and / or Special	
A-1		

OVERVIEW

Advancing several key research themes of importance both to the University of Kent and the Phillips Laboratories, results of the 12 month research project, commencing 15th August 1993, are presented. The project addresses: optical damage; impact damage and scaling laws; energy partitioning (experimental and hydrocode); diagnostic impact facility design.

Optical damage assessment presents initial analysis of a large database of retrieved space damaged material (solar cell arrays); results to be analysed in more detail in the future show a peak in the space environment damage effects in the millimetre region and a dominance by meteoroids in this region. Impact damage features on glass will be folded with the first results of the energy partitioning results which derive from the unique 2 MV Van de Graaff facility achieving (in this report) velocities of up to 42 km sec^{-1}. Experimental campaigns incorporating simultaneous measurement of impact plasma, impact light flash and momentum enhancement have been shown to allow derivation of many of the fundamental features of energy partitioning in hypervelocity impacts: ejecta momentum and kinetic energy, plasma and vapour production, and light flash energies. Use of hydrocode simulations in support of these experiments allows further investigation of internal and comminution/distortional energy.

First results from a study of the impact light flash have proven principles of the prototype chamber design which was commissioned with support by the University of Kent. Results which complement the energy partitioning data obtained from the plasma studies show readily the sensitivity of this technique as a study tool on the Van de Graaff facility, but the data has relevance to the optical flash generated in space on satellite by natural meteoroids and space debris.

The project has achieved the objectives defined within the study and in some areas exceeded expectations. It has, further, provided the starting point for publication in these areas and laid the basis for a continued collaboration between the Phillips Laboratory and the University of Kent.

CONTENTS

1. Surface Damage Due to Impacts on Optical Components - Dr. L. Kay

1.1 Methodology

Although the objective focussed on laboratory hypervelocity impact, which were commenced in house on the 2 MV microparticle accelerator, factors during the contract led to a change of emphasis which favoured the analysis context of this objective, of space impact data from the Eureca spacecraft.

A video microscope has been used to record images of impact features on solar cell cover glasses retrieved on the Eureca satellite. All 10 panels of the solar array were surveyed and the digitised images were then stored on compact discs (photo CD's). Selection of impact features for image storage corresponded to spall diameters (or equivalent diameters, see below) greater than about 0.4 mm. In addition, the features with spall diameters to below 0.1 mm were recorded over a single swath on each panel; each swath covers about 10% of the panel area.

Measurements of impact features have been made on all the digitised images. For each impact exhibiting circular symmetry, the diameters of the central pit, shatter zone and spall (conchoid) zone were recorded. For each elliptical impact feature, corresponding pairs of measurements were made along and perpendicular to the major axis; equivalent diameters were then calculated as the geometric means of pairs of measurements. The resulting data set is the largest in existence for in-orbit impacts on solar arrays; it complements the LDEF meteoroid debris database which, although larger, mostly refers to impacts on targets other than glass.

1.2 Results

The first histrogram (Figure 1.1) shows the number of impact features with spall zone diameter (or equivalent diameter) in each 0.2 mm interval for diameters greater than about 0.4 mm. The number does not decrease monotonically with spall diameter. A minimum occurs, at about 1.5 mm, between peaks at 0.7 mm and 1.9 mm. The peak at 0.7 mm is not an artefact resulting from loss of detection efficiency at low values of spall diameter. It is present in the second histogram (Figure 1.2) which shows the results of a high-resolution scan (to below 0.1 mm diameter) of about 10% of the total area of the array.

The optically damaged area $\pi D^2 / 4$, where D is the equivalent spall diameter (see above), was calculated for each impact and summed for all the impacts in each bin. Figures 1.3 and 1.4 show the resulting histograms. They correspond in first approximation to Figures 1.1 and 1.2 with the number of impacts in each bin multiplied by the square of the spall diameter at the bin centre.

The total area affected by all the measured impact features is found to be a fraction 2.13×10^{-5} of the area of the array. The satellite spent 10.8 months in orbit and so the average rate of spall-area formation was a fraction 2.0×10^{-6} per month.

2

IMPACTS ON EURECA SOLAR ARRAY: NUMBER DIFFERENTIAL DISTRIBUTION USING 0.2MM BINS

Figure 1.1 Number histogram for low-resolution scan showing a minimum at 1.5mm between peaks at 0.7mm and 1.9mm.

IMPACTS ON EURECA SOLAR ARRAY: NUMBER DIFFERENTIAL
DISTRIBUTION USING 0.2MM bins

Figure 1.2 Histogram for high-resolution scan showing persistence of peak at 0.7mm.

4

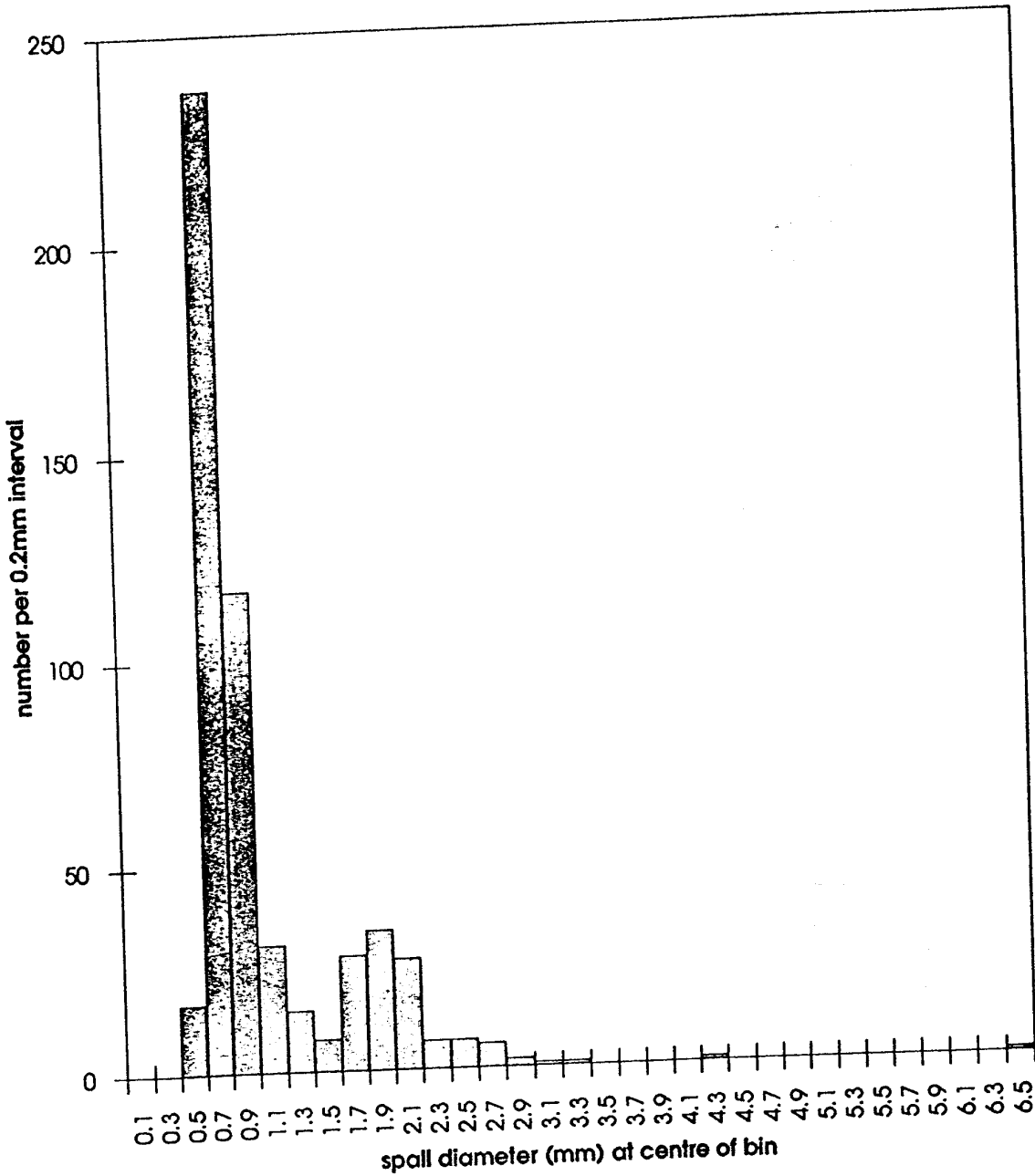IMPACTS ON EURECA SOLAR ARRAY: AREA DIFFERENTIAL
DISTRIBUTION USING 0.2MM BINS

Figure 1.3 Area histogram for low resolution scan showing a minimum at 1.5mm between peaks at
0.7mm and 1.9mm.

IMPACTS ON EURECA SOLAR ARRAY: AREA DIFFERENTIAL
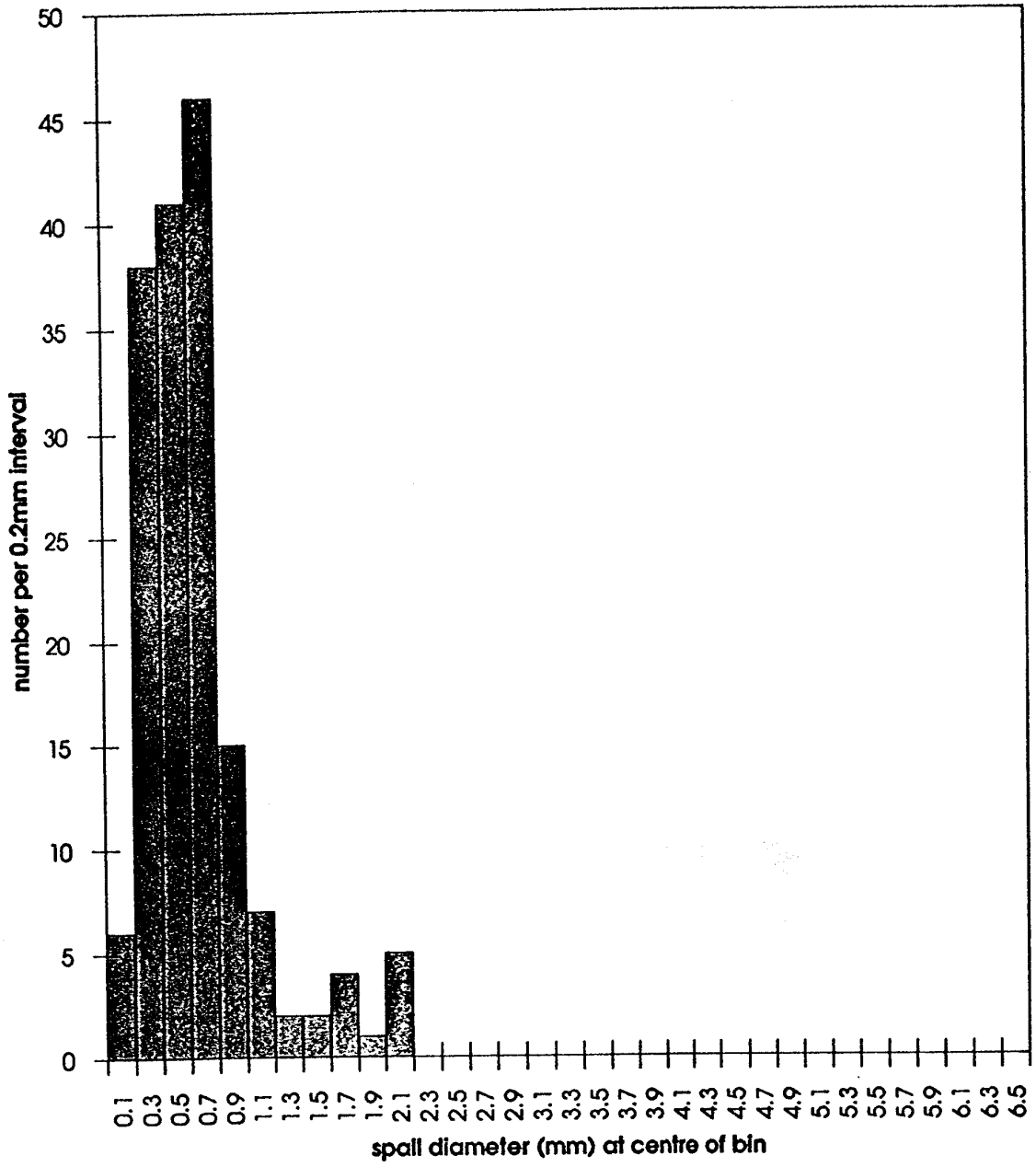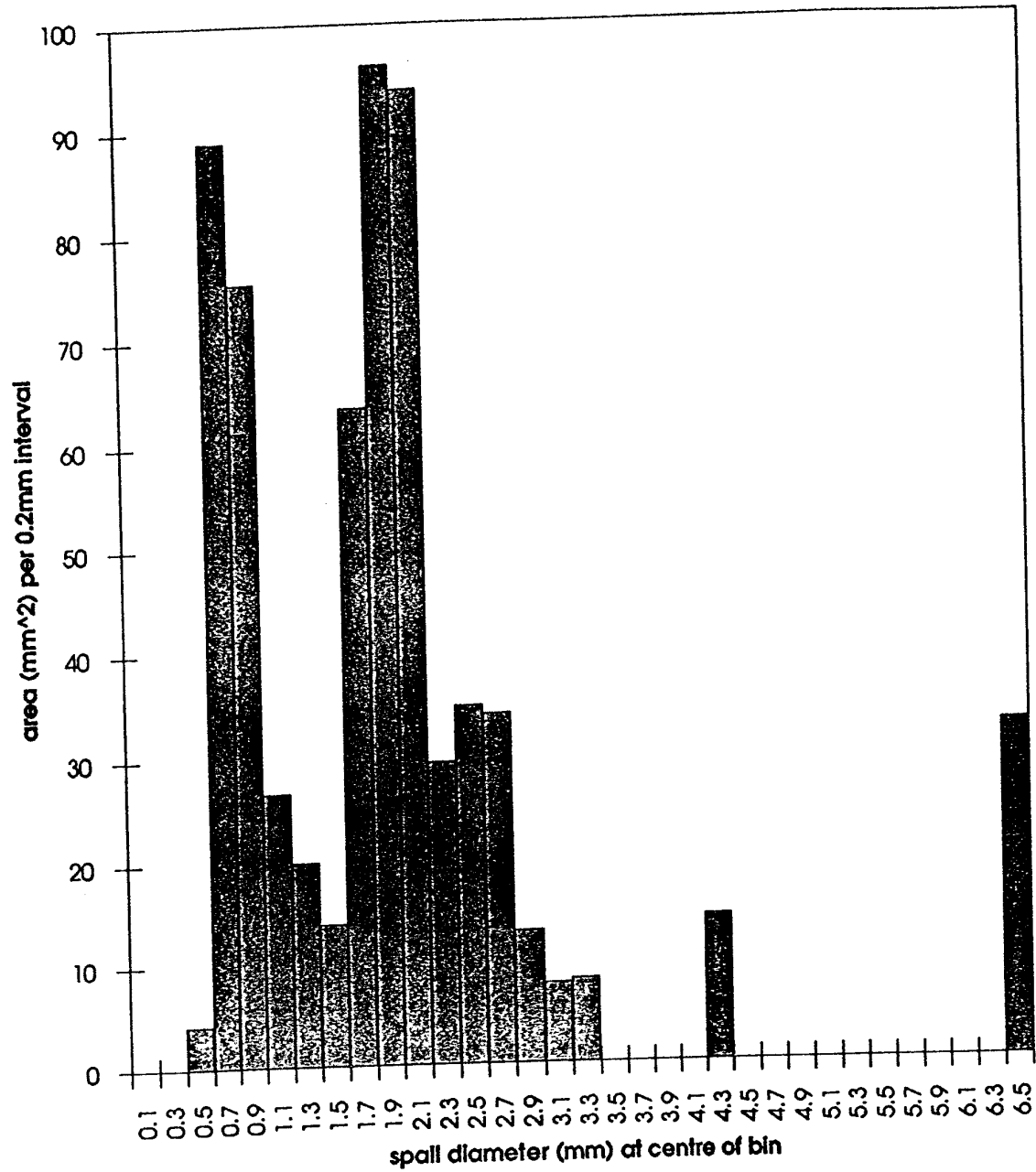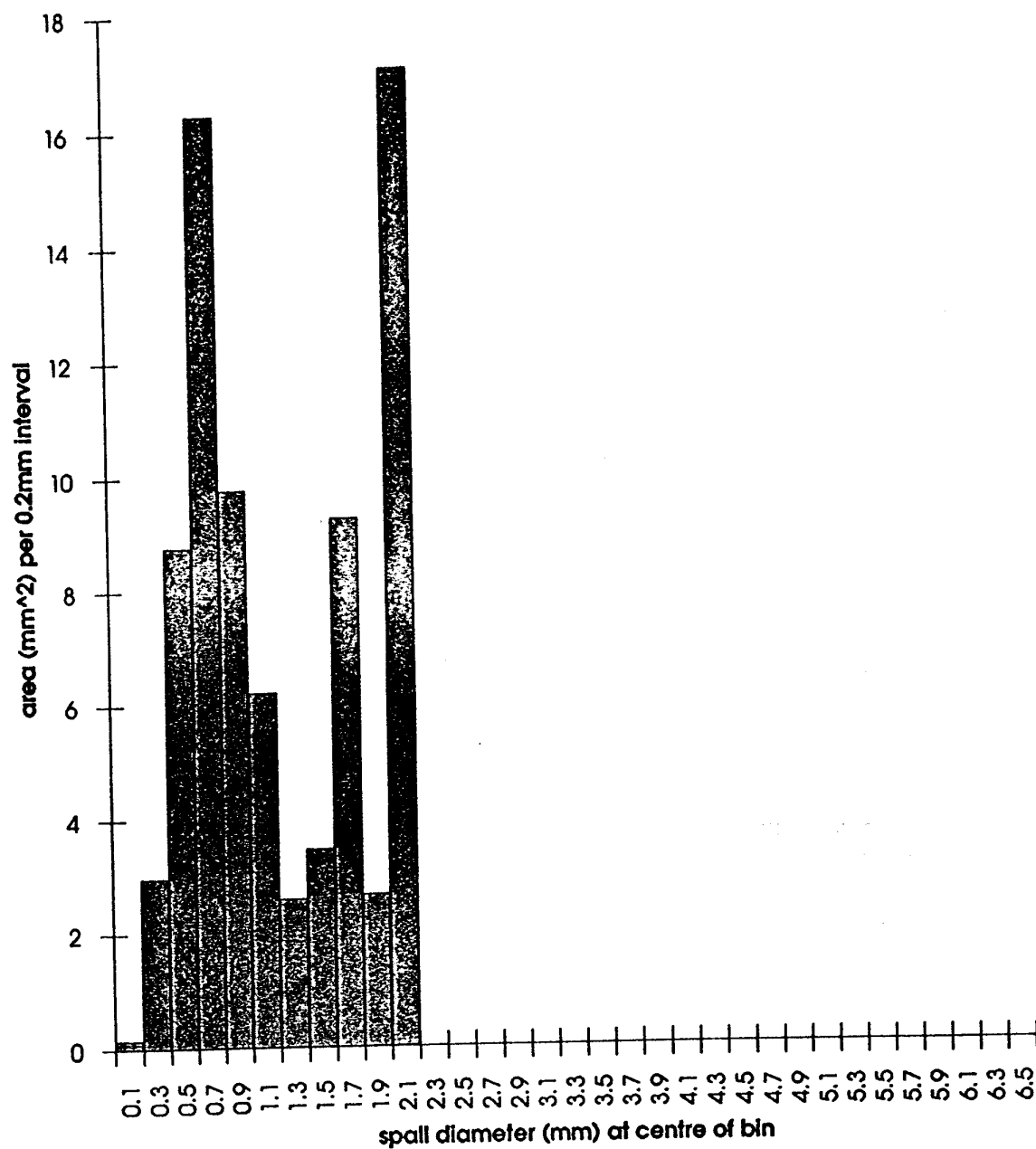## DISTRIBUTION USING 0.2MM BINS

Figure 1.4 Area histogram for high-resolution scan showing persistence of peak at 0.7mm.

Projections of the total area of solar array affected by impacts may be obtained from the formula:

$$A = 2.37 \times 10^{-5} (f^Y - 1/f - 1)$$

where A is the fraction area affected, Y is the time in years of exposure to in-orbit impacts and f is the factor by which the micrometeoroid and debris (MMD) flux increases annually. Figure 1.5 shows plots of A versus Y for 3 values of f:

i)   f = 1 (continuous line) corresponding to no growth in MMD flux.

ii)   f = 1.02 (dashed curve) corresponding to growth in MMD flux of 2% per annum.

iii) f = 1.05 (dotted curve) corresponding to growth in MMD flux of 5% per annum.

We also compute the area of conchoidal spall damage in each interval (Figures 1.3 and 1.4). Clearly showing peaks at diameters of 0.7 mm and 1.9 mm, this corresponds to a regime where, even in the LEO impact scenario, the meteoroid-to-debris ratio is high.

1.3   Discussion

Studies of simulated microcraters in glass have been published by Vedder (1971), Mandeville and Vedder (1971), Mandeville (1972) and Vedder and Mandeville (1974). Spalling phenomena are totally absent for sub-micrometer craters (Mandeville, 1972). However, this observation cannot account for either of the peaks shown in Figures 2.1 to 2.4, since even the lower peak (at 700 μm) is at a value much too high to be influenced by an absence of spalls of diameter less than (say) 10 μm. (Spalls occur in almost all cases for craters greater than about 1 μm diameter; also the ratio of spall diameter to crater diameter never exceeds 8 for projectiles of polystyrene, aluminium or iron in the velocity range 0.5 km s^{-1} to 15 km s^{-1} (Vedder and Mandeville, 1974)).

For the same reason, the suggestion (Mandeville, 1993) that a cut-off in the natural particle size distribution in low earth orbit (LDEF) occurs for crater sizes less than 1.5 μm in aluminium cannot provide an explanation for even the lower of the two peaks in Figures 1.1 to 1.4.

A more promising line of understanding we will pursue to explain the occurrence of peaks considers the effect of the structure of the solar array panels shown in Figure 1.6. The first 3 layers consist of a glass cover slide (thickness 150 μm) and a sheet of silicon (thickness 180 μm) separated by 30 μm of adhesive. The observed peaks may be associated with penetration of one or more of these layers.

Hörz et al (1994a, 1994b) have suggested that "penetration" may best be defined in terms of relative shock pulse duration in target and projectile. Their criterion corresponds to a much larger ratio of projectile diameter to target thickness than corresponds to the ballistic limit. They show that, before penetration occurs, the extent of spall zones at the target's front surface remains essentially the same as for

PROJECTION OF TOTAL AREA OF SOLAR ARRAY AFFECTED BY IMPACTS
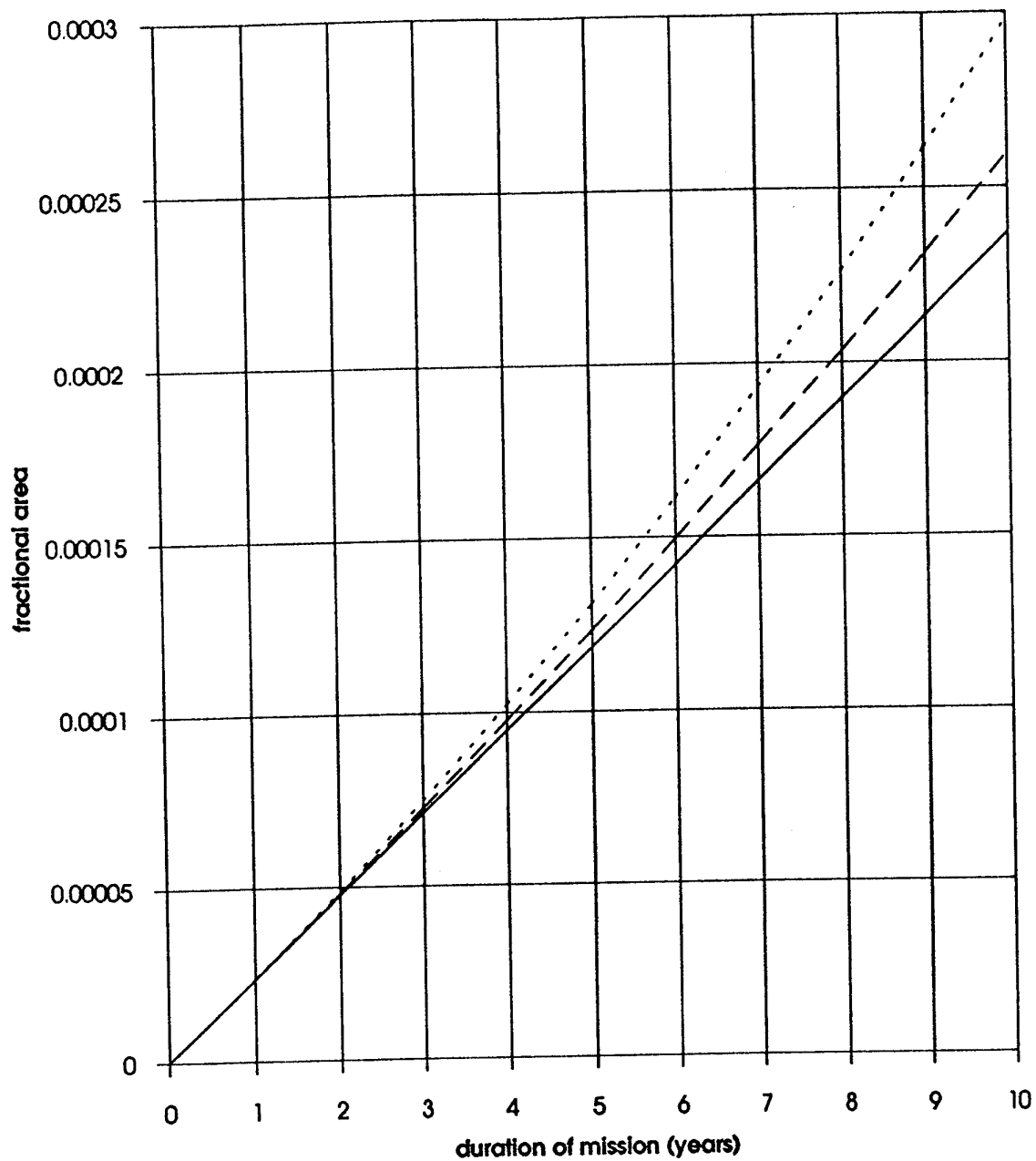
Figure 1.5 Projections of the fractional area affected, assuming no annual increase in MMD flux (lower curve), 2% annual increase (middle curve) and 5% annual increase (upper curve).
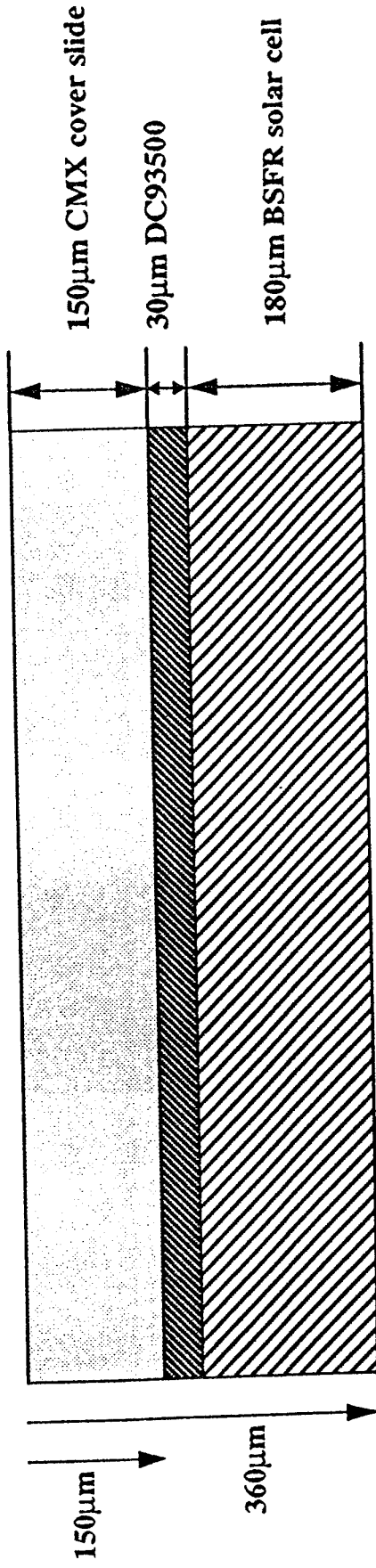
EURECA Solar Array Cell Cross-Section

150μm CMX cover slide

30μm DC93500

180μm BSFR solar cell

150μm

360μm

Ratio total cell thickness to cover slide thickness = 2.4

Figure 1.6. Schematic of the solar array structure.

a"standard" crater, i.e. a crater in a semi-infinite target. After penetration occurs, both crater and spall diminish in size as the ratio of projectile diameter to target thickness increases (for otherwise constant projectile parameters). Assuming that the scaling suggested by Hörz et al (1994) is applicable, the foregoing provides a mechanism whereby peaks may occur, at least for spherical projectiles of fixed density and velocity but different diameters. This possibility is verified mathematically using a simple model, for the purpose of illustration only, in Appendix A. Whether this process should result in a peak after summing over the real distribution of projectile velocity and composition cannot be determined by calculation as yet.

1.4 Summary

Measurements of impact features on the Eureca solar array have resulted in number and area differential distributions for a range of spall-zone equivalent diameters from 0.1 mm to 6.5 mm. The fractional area corresponding to the above impacts has been found. Projections of the fractional area affected as a function of mission duration have been presented for 3 values of rate of growth of MMD flux. A mechanism whereby a peak in a differential distribution curve may be linked to penetration has been illustrated mathematically.

2. Impact Damage Characteristics - Dr. D.H. Niblett

2.1 Introduction

The objective of this Work Package was to develop scaling laws of impact damage characteristics as a function of the dynamics of projectile/target interactions and material properties. The first stage of this consisted of a validation of AUTODYN hydrocode simulations by comparison of the simulation results with experimental data for hypervelocity impacts. A programme of impact simulations using the AUTODYN-3D hydrocode for oblique impacts was then carried out to determine how the depth, diameter and ellipticity of impact craters in semi-infinite aluminium targets depend on the projectile density, velocity and impact angle.

The results were applied to an investigation of the craters observed on some aluminium clamps which fastened experiment trays to the framework of the Long Duration Exposure Facility (LDEF). The distribution of impact angles was calculated for a surface exposed to an isotropic distribution of incident particles. This was then used to determine the distribution of crater shapes produced by projectiles with a given density and velocity and the results were compared with those observed on LDEF. The aim of this application was to obtain information about the properties of the particles which produced the craters. Improved definition of the microparticulate environment, together with a better understanding of hypervelocity impact processes, would provide valuable information for the deployment of optical systems in space.

2.2 Validation of AUTODYN Hydrocode Simulations

The impact simulations in this work were performed using AUTODYN, which is an interactive, integrated hydrocode available on a wide range of computers (Birnbaum et al, 1987). It is available in a 2D version for normal impacts and in a 3D version for oblique impacts.

A number of analyses were carried out to validate AUTODYN for hypervelocity impacts by comparison with experimental impact data and to select the equation of state and material model and the associated parameters for iron and aluminium. A database of published experimental impact data was compiled; the most relevant to our investigations were those of Christman and Gearing (Anderson et al, 1992), Stradling et al (1993) and Christiansen et al (1993). The Tillotson equation of state (Tillotson, 1962) was selected because it accounts for phase changes by modelling a solid to gas transition. The Johnson-Cook strength model (Johnson and Cook, 1983) was chosen so that the important effects of strain and strain-rate hardening and thermal softening could be taken into account. AUTODYN-3D uses a Lagrange processor, with a grid of cells which distort with the material. The ability of the Lagrange processor to simulate impact problems with large deformations can be enhanced by the use of an erosion algorithm, which removes cells which have reached a certain user-specified strain. AUTODYN-2D simulations were performed for iron particles impacting copper for velocities ranging from 5.5 to 16.5 km s^{-1}, using different values of this erosion strain. The results were compared with experimental

data (Stradling et al, 1993) in Figure 2.1. There is good agreement between the experiment and the calculations at the lower velocities, but the calculations using an erosion strain of 1.5 do not agree with the experimental data at higher velocities. Unfortunately the use of high erosion strains leads to long computation times, so a compromise is necessary and an erosion strain of 2.0 was used in this work. Correction factors were applied to the results to compensate for the errors introduced by using this erosion strain.

2.3   Hydrocode Oblique Impact Results

AUTODYN-3D was used to carry out a programme of oblique impact simulations, involving aluminium and iron spheres of 1 μm diameter impacting semi-infinite aluminium targets at velocities up to 16 km s^{-1}. The hydrocode calculations determined values of the crater depth T_c (relative to the original surface plane) and the maximum and minimum diameters of the crater, a and b, (measured in the original surface plane) for a number of impact angles θ (measured relative to the normal to the target surface) between 0 and 85 degrees. Further details of the hydrocode simulations and their validation will be presented at the 1994 Hypervelocity Impact Symposium at Sante Fe (Hayhurst et al, 1994).

Parameters of particular interest are the ratio of the crater depth T_c to the crater diameter D_c defined by

$$D_c = (ab)^{1/2} \qquad\qquad (2.1)$$

and also the crater ellipticity e defined by

$$e = (1 - b^2/a^2)^{1/2} \qquad\qquad (2.2)$$

Figures 2.2 and 2.3 show values of T_c/D_c and e computed from the hydrocode results plotted against the impact angle for aluminium and iron projectiles at velocities of 10 and 16 km s^{-1}. We see that the material is much more significant than the velocity in determining the shapes of the graphs. In particular, iron produces deeper craters than aluminium at normal incidence, as would be expected because of its higher density.

2.4   Distributions of Impact Angles

An application of the dependence of the crater shape on the impactor parameters determined in 2.3 above is to predict the distributions of values of T_c/D_c and e to be expected for craters on a spacecraft surface after exposure to the space environment. To do this it is necessary to determine the angular dependence of the impacts on that surface. A precise determination of this requires three-dimensional models of the velocity and mass distributions for natural micrometeoroids and space debris (Mackay et al, 1993).

A much simplified treatment used here is to restrict our attention to the larger craters, with diameters greater than 20 μm, which have been seen (Niblett et al, 1993)
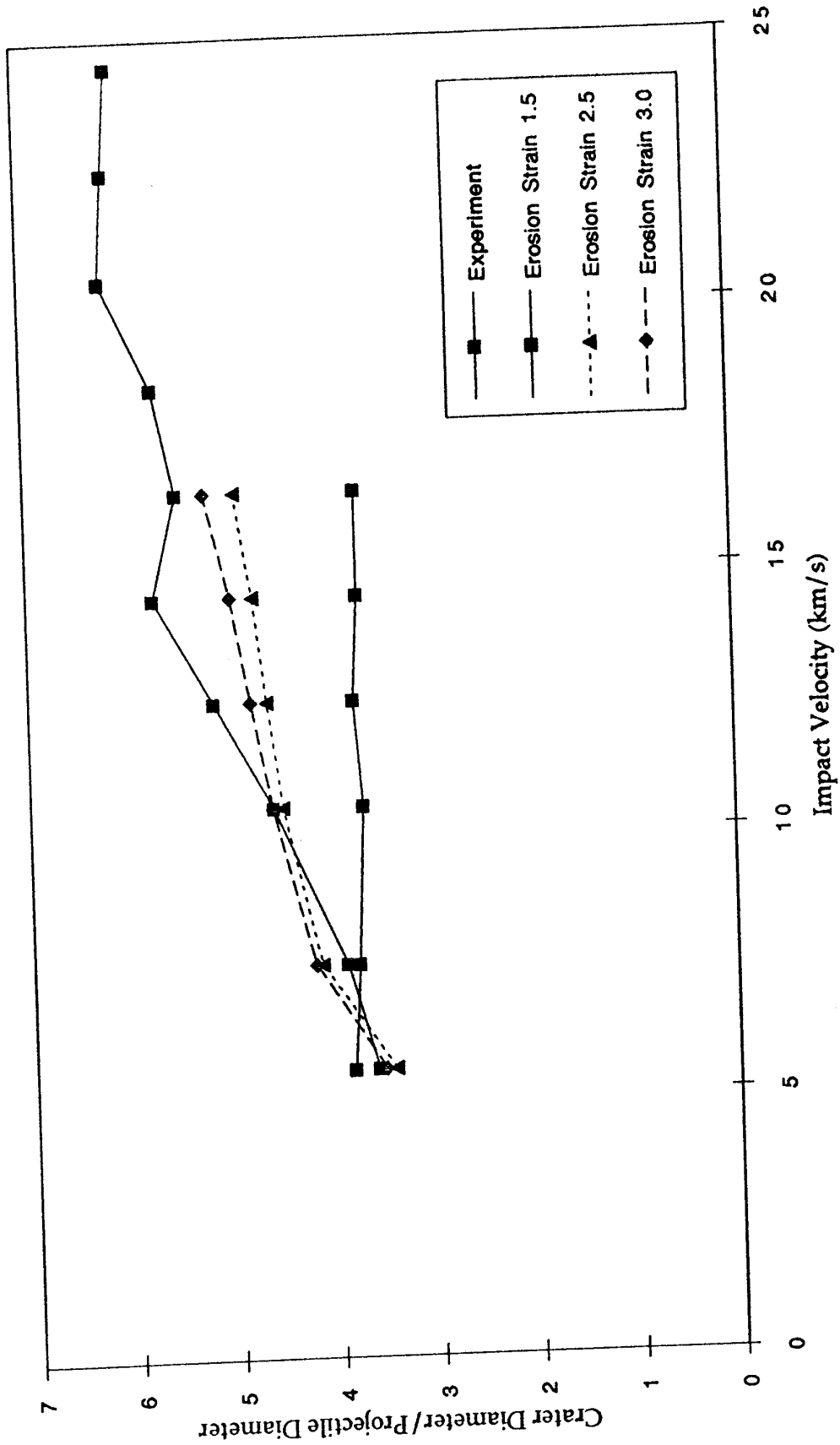
Figure 2.1   AUTODYN-2D results for different erosion strains compared with experimental results
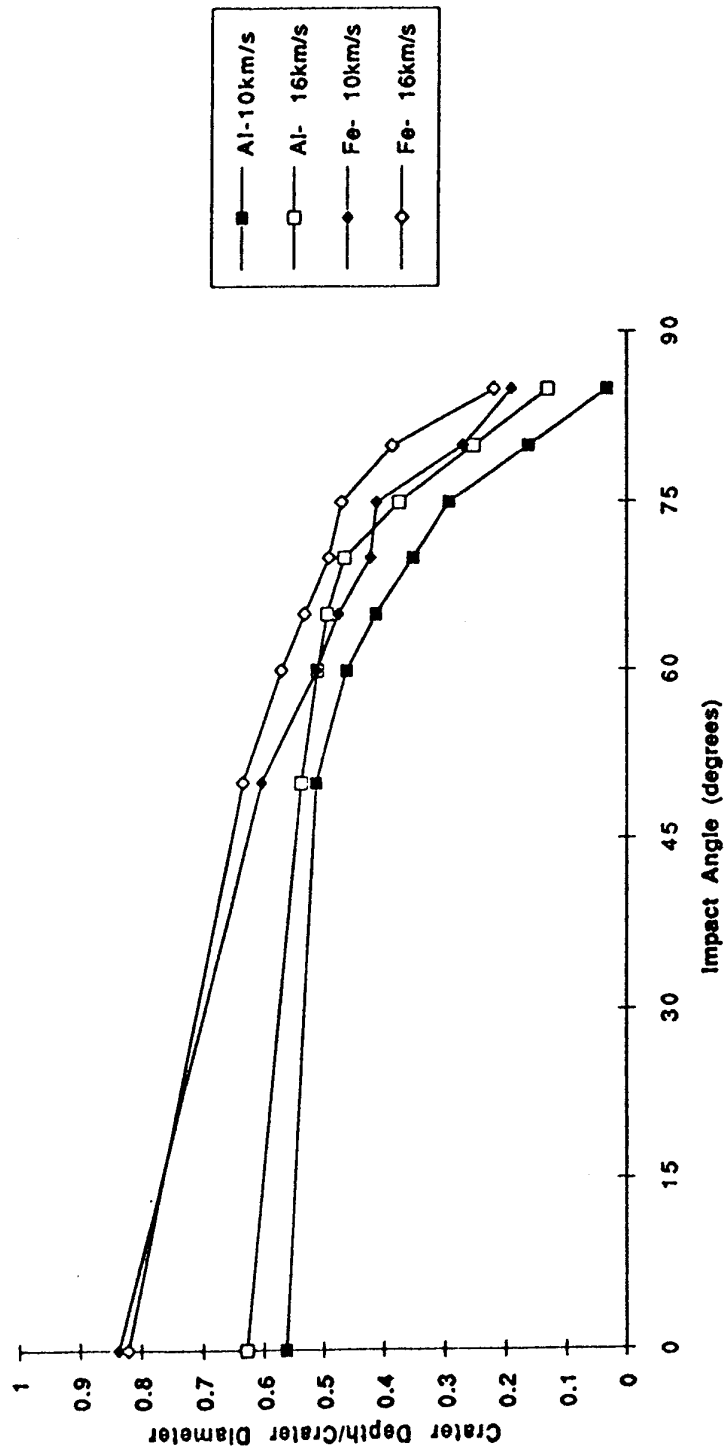
Figure 2.2   AUTODYN-3D results for crater depth/crater diameter ratios as a function of impact angle
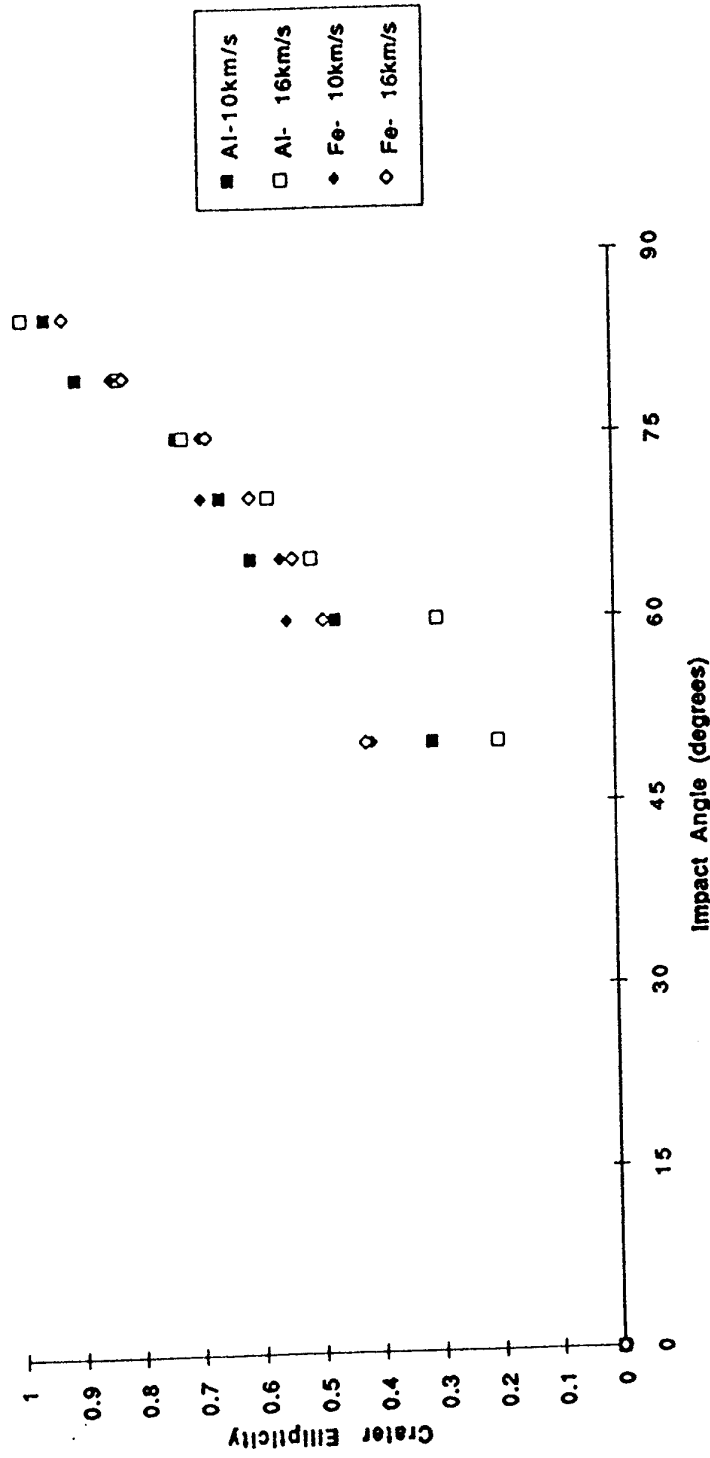
14

Figure 2.3   AUTODYN-3D results for crater ellipticity as a function of impact angle

to be predominantly caused by natural micrometeoroids, to assume that this micrometeoroid population can be represented by an isotropic flux and to neglect the effects of the spacecraft's motion and any possible Earth shielding. It then follows that the probability of an impact occurring on a stationary plane surface at an impact angle between θ_1 and θ_2 is given by:

$$P = \sin 2\theta \, d\theta = (\cos 2\theta_1 - \cos 2\theta_2) \qquad (2.3)$$

This gives a distribution of impact angles with a maximum value at 45° and symmetrical about this impact angle.

Calculations based on models for the micrometeoroid population show (Niblett et al, 1994) that this calculation for a stationary surface gives a good approximation to the distribution of impact angles on an orbiting spacecraft surface unless the spacecraft's velocity vector is near the normal to the surface (as, for example, for the East or West faces of LDEF).

2.5 Crater Depth/Crater Diameter Ratio Distributions

We are now in a position to calculate the expected distribution of T_c/D_c ratios which would be observed if all the impacting particles were of the same material (aluminium or iron) and travelling at the same speed (10 or 16 km s^{-1}) but with a range of impact angles. The first stage is to use the appropriate graph in Figure 2.2 to determine the range of impact angles which would produce craters with T_c/D_c ratios within a certain range. For example, for iron projectiles at 10 km s^{-1} impact angles between 56° and 62° produce T_c/D_c ratios between 0.50 and 0.55. We then use equation 2.3 to calculate the probability of an impact occurring within that range of impact angles. This enables us to plot the probability distributions expected for T_c/D_c for each impactor material and speed (Figure 2.4).

These results can be compared with measurements of T_c/D_c for craters in the aluminium clamps which fastened the experiment trays to the framework of LDEF (McDonnell et al, 1993b). Figure 2.5 shows the distributions of T_c/D_c ratios for 36 craters in clamps on the North and South faces of LDEF and for 15 craters on the Space-facing clamps. It is appropriate to compare these observed distributions with those calculated for a stationary surface. It is seen that, in both cases, the observed T_c/D_c distributions spread over a wider range of values than those calculated for any of the projectile materials and speeds, showing that a range of projectile properties is required. The majority of the observed T_c/D_c values come in the region near the peaks of the calculated distributions for aluminium impactors. However, a significant number of craters were observed with T_c/D_c values greater than 0.65, in the region where the calculated distributions for iron have their most probable values and higher than the maximum value of T_c/D_c calculated for aluminium. This implies that the impacting particles must contain some with densities greater than that of aluminium, e.g. iron meteorites.
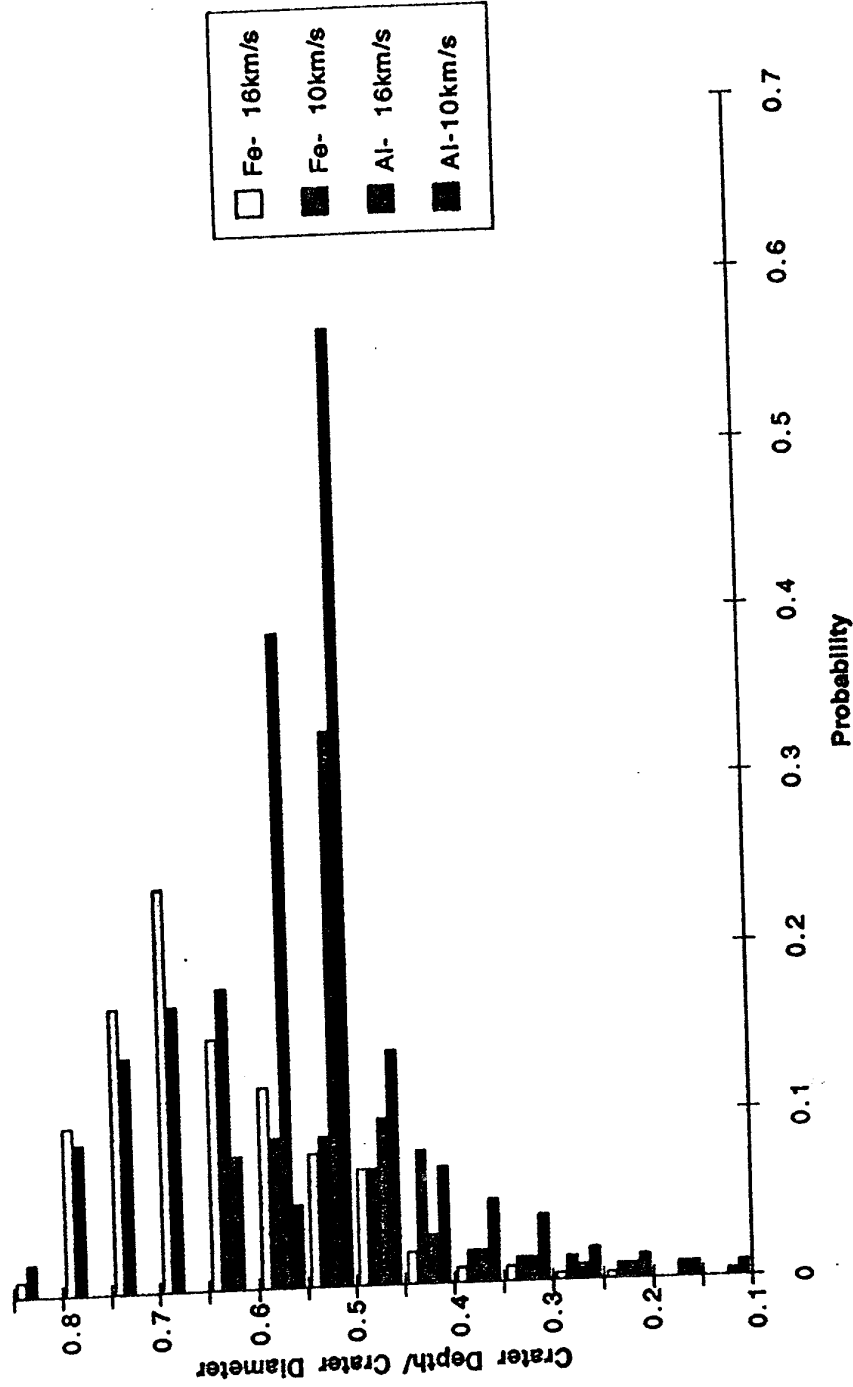
Figure 2.4   Calculated distributions of depth/diameter ratio for craters on a stationary surface
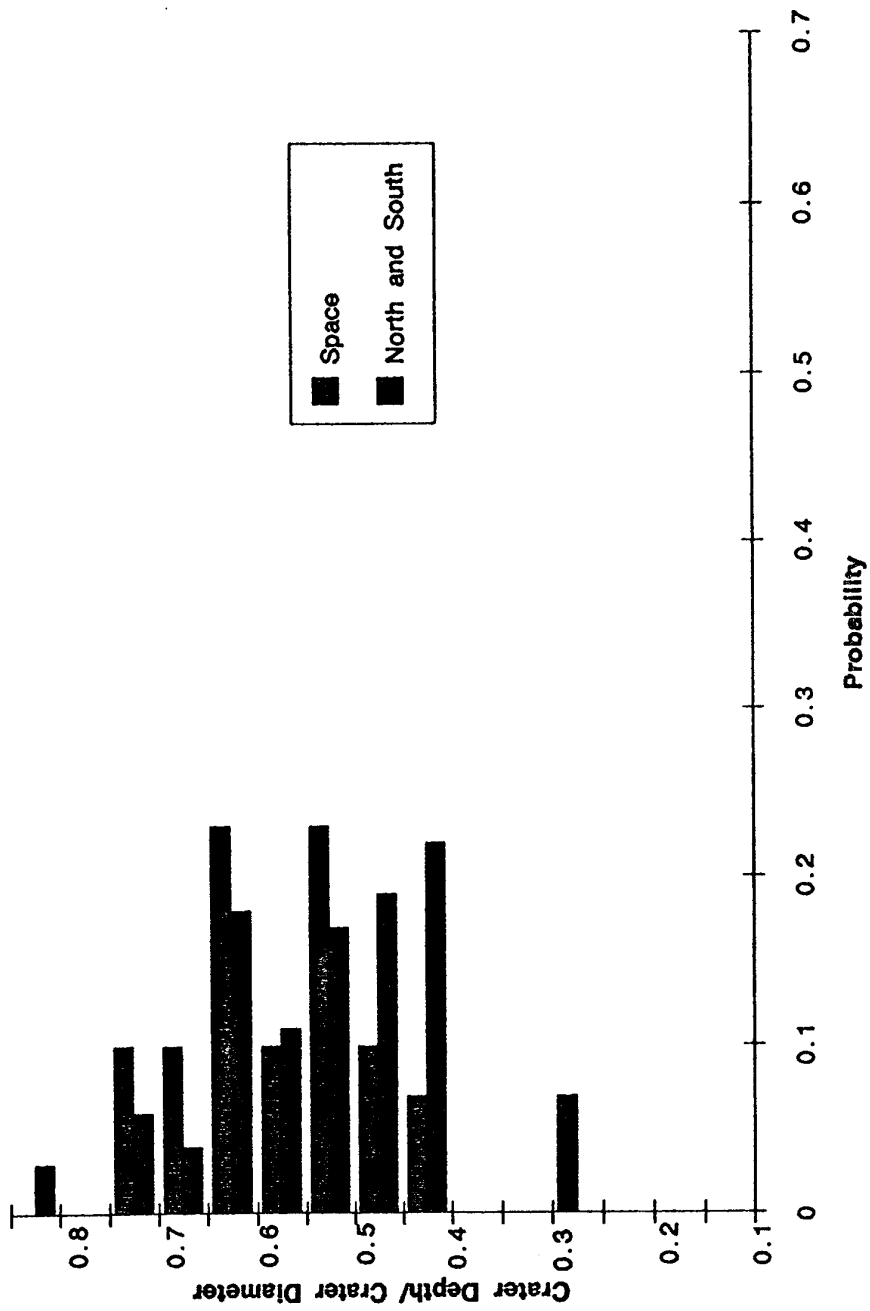
Figure 2.5   Distributions of depth/diameter ratio for craters on aluminium clamps on LDEF

18

2.6   Ellipticity Distributions

We have also calculated the expected distribution of ellipticity values for a given impacting material and speed, using a similar procedure to that for calculating the T_c/D_c distribution. The hydrocode data in Figure 2.3 are used together with equation 2.3 to give the distributions of ellipticity values for a stationary surface shown in Figure 2.6. These are then compared with the ellipticity distributions observed for the craters on the North and South and Space clamps on LDEF (Figure 2.7). The calculations show that aluminium, particularly at 16 km s^{-1}, is more likely to produce near-circular craters (ellipticity < 0.2) than iron is. The proportions of near-circular craters observed on the LDEF clamps were even higher than those calculated for aluminium, which implies that the impacting particles included a substantial fraction with low density and high velocity.

2.7   Conclusions

AUTODYN-3D simulations have been used to determine how the depth, diameter and ellipticity of impact craters in semi-infinite aluminium targets depend on impact angle for aluminium and iron projectiles at 10 and 16 km s^{-1}. In view of the different forms of angular dependence of the crater shapes obtained for different projectile properties, it has not been possible to deduce a simple empirical formula to relate the impact characteristics to the projectile properties. However, we have been able to devise a procedure for using hydrocode calculations for oblique impacts together with impact angular distributions for a spacecraft surface to determine the distributions of crater shapes (depth to diameter ratios, ellipticities) to be expected for craters on that surface. This procedure has been used to compare the distribution of crater shapes observed on aluminium clamps on LDEF with those expected for a stationary surface exposed to an isotropic micrometeoroid flux. This comparison shows that particles with a wide range of densities were responsible for these craters, including both chondritic and iron meteorites. The procedure needs to be extended to include orbital debris as well as interplanetary meteoroids in order to interpret the smaller craters on LDEF, which were mostly produced by orbital particles.

To enable more precise conclusions to be made about the properties of the particles which impacted the surface of an exposed system or detector in space it would be necessary to refine the calculations. In particular, there is a need to make more hydrocode simulations for:

(a)   impactors with more different densities, especially some with densities lower than that of aluminium;

(b)   impactors with more different velocities;

(c)   more impact angles, especially between 0 and 50 degrees;

(d)   alternative target materials.

The accuracy of the AUTODYN results should be verified by comparing them with similar calculations using different hydrocodes and by obtaining more experimental
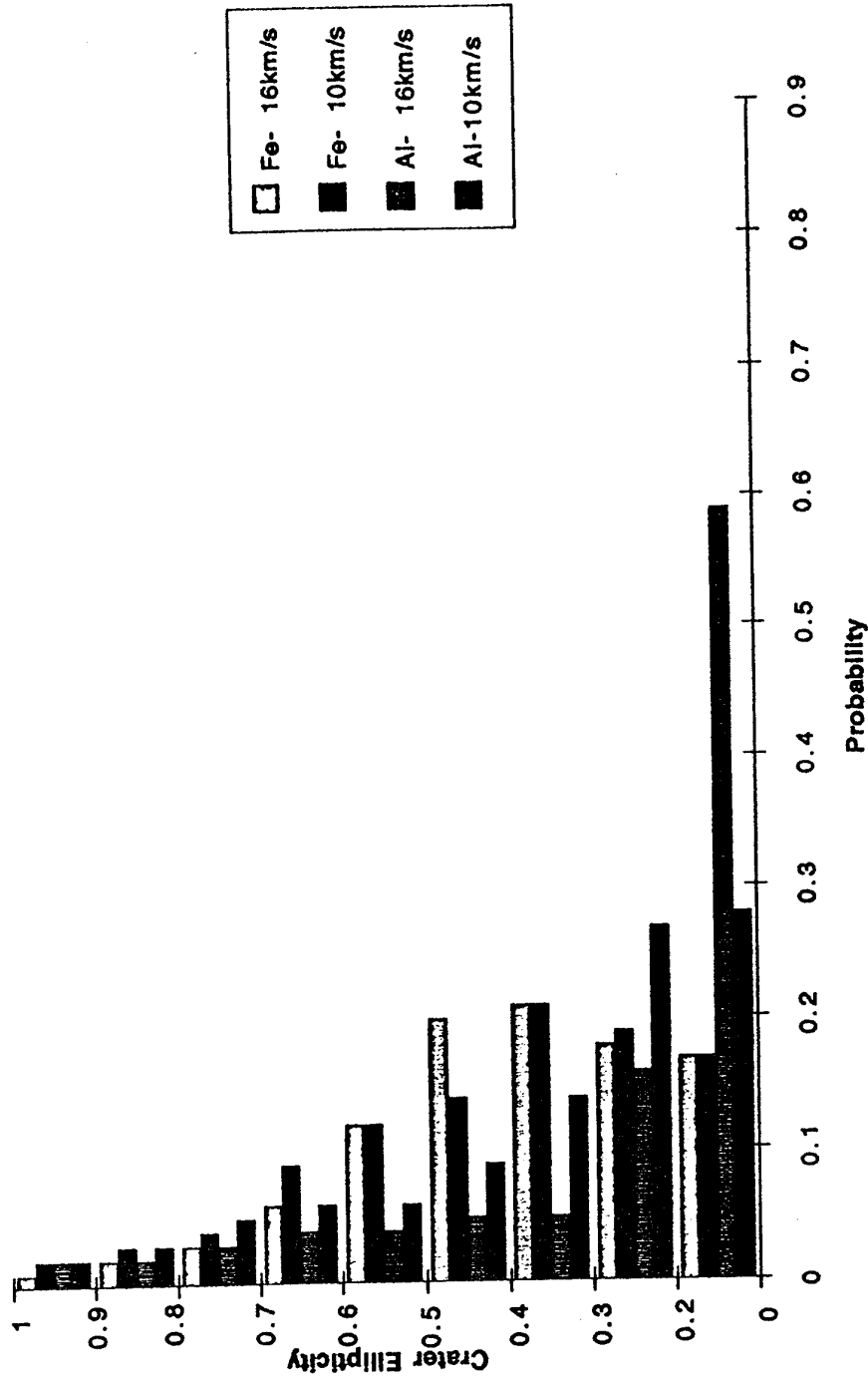
Figure 2.6   Calculated distributions of crater ellipticity for a stationary surface
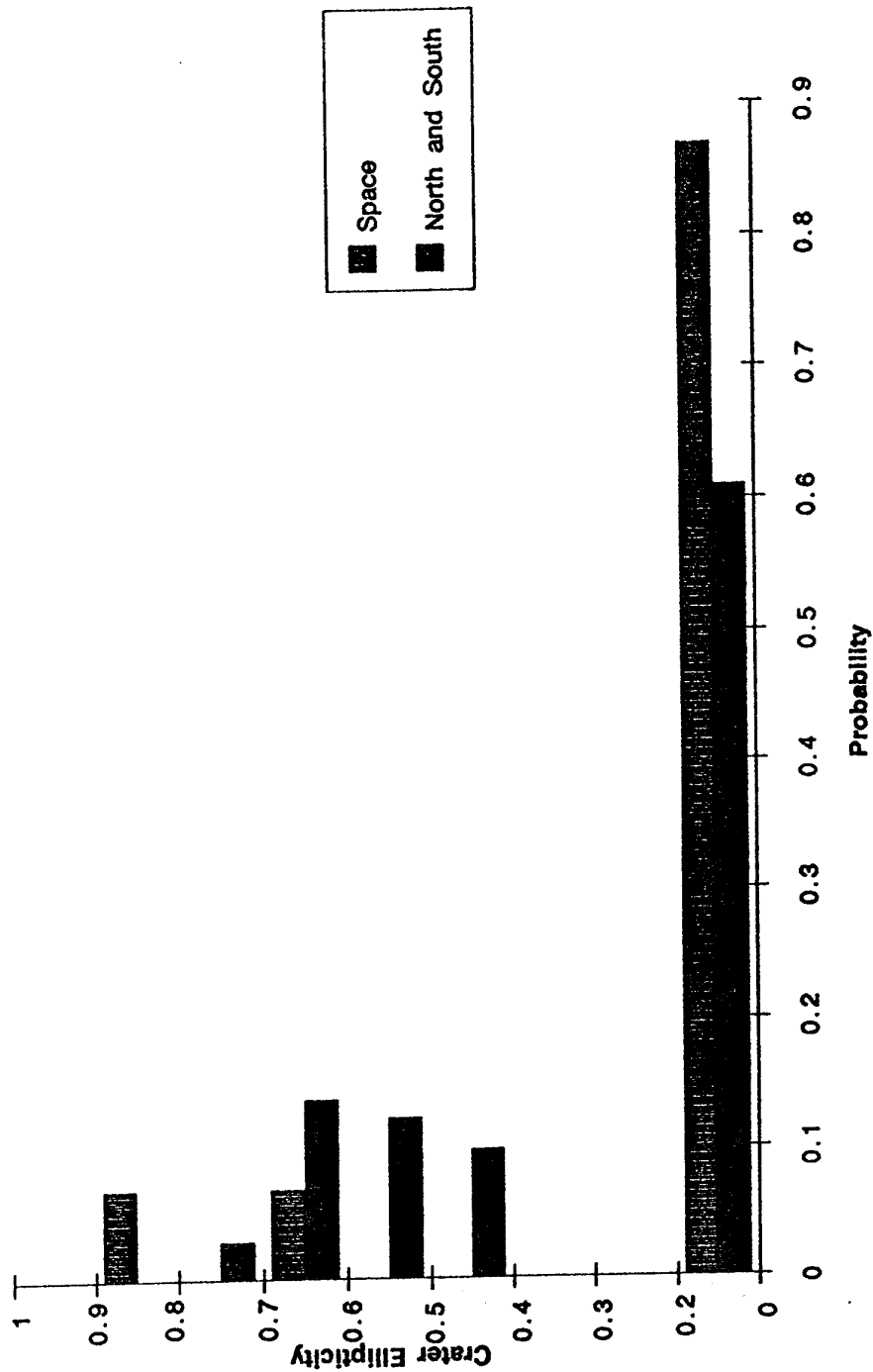
Figure 2.7   Distributions of ellipticity for craters on aluminium clamps on LDEF

hypervelocity impact data for validation. In particular, the CTH hydrocode has been used for a detailed study of normal impacts (Tanner et al, 1994) and this should be extended to include oblique impacts.

3. Energy Partitioning in Hypervelocity Impacts - Theoretical and (Pilot) Experimental Study of the Energy Partitioning During Hypervelocity Impact Events - Dr. P.R. Ratcliff

3.1. Specified Objective

The objective of this Workpackage, as defined in the contract proposal, was:

"Characterisation of energy partitioning will be performed by a synergistic approach uniquely available at the hypervelocity accelerator facility which is required to achieve ultra high speeds. At the maximum achieved velocity of 94 kms^{-1}, entirely new regimes of energy partitioning could pertain.

"The synergistic approach comprises:-

1. Hydrocode modelling. Using 2D axisymmetric modelling (Century Dynamics Alternate Euler-Lagrange coupling) internal energy and states of matter and ejecta velocities will be tracked. Results will be used to develop the experimentation for:

2. Hypervelocity impact measurements of:

a) ion velocities (detected by 400 MHz time of flight resolved spectral measurement of each elemental line);

b) time resolved measurements of the light flash of impact, resolved in initial pilot experiments spatially only in two areas, namely the *impact crater area* and *expanding debris cloud and late stage expansion*;

c) acoustical wave measurements, via 200 kHz piezoelectric transducers, in the target material (but due to the momentum spectrum of the accelerator) only at velocities of up to 7 kms^{-1}.

These questions have been fully addressed using a combination of the techniques proposed and others developed during the study.

3.2. Introduction and Methodology

When an object strikes a surface at extremely high velocity, the kinetic energy of the impactor is distributed through several paths. These include:

- Internal energy in the impactor and target (i.e. heating)

- Kinetic energy of ejecta

- Inducing material phase change (i.e. overcoming material heats of fusion and vaporisation)

- Material comminution and/or compaction

- Light emission

- Elastic wave propagation

The importance of each of these paths depends on the impacting and target materials, and on the impact velocity.

Hydrocode simulations and experimental investigations have been performed to investigate the energy partitioning as a function of the velocity of the incident particle. The two techniques have different merits for measuring the energy in different paths, and so the two approaches provide some degree of both complimentarity and cross-calibration rather than exclusively one or the other.

Some aspects of the hydrocode work were performed in common with Workpackage P2, and some aspects of the experimental work in common with Workpackage P4. Repetition in this report is avoided by reference to these sections where appropriate.

3.3. Terminology

Every attempt has been made to use standard terminology, and SI units are used throughout. One comment that needs to be made concerns possible confusion over the use of the phrase *particle velocity*. To a cosmic dust (or space debris) dynamicist, *particle* refers to an individual grain of material, and the *particle velocity* is its speed in the chosen reference frame. When considering impacts, this frame is usually that in which the target is at rest, so *particle velocity* is the speed of impact. When considering impact physics, however, *particle velocity* is the speed of the particles (i.e. atoms or molecules) in the material after the impact, as opposed to the wave velocity of the expanding shock waves. In this report, the phrase *particle velocity* will be reserved for the impact physics usage, and *impact velocity* will be used for the velocity of the impacting particle.

3.4. Results

3.4.1 Hydrocode Simulations

The hydrocode used for this work was AUTODYN[TM] (e.g. Birnbaum and Cowler, 1987, Birnbaum et al., 1987, Robertson et al., 1993), developed and marketed by Century Dynamics Inc. The impactor-target system modelled was chosen to represent a typical experiment geometry that could be achieved with the 2 MV Van de Graaff accelerator facility of the University of Kent (Burchell et al., 1993) - the impact of a 1 μm diameter iron sphere on a semi-infinite target. The target material was chosen to

24

be aluminium 2024, an alloy of aluminium commonly used in spacecraft applications, and one with well-characterised physical properties.

AUTODYN offers three processing methods: Lagrangian, Eulerian and ALE (Arbitrary Lagrangian-Eulerian). In addition to not allowing the generation of ejecta, the Lagrangian processor utilises an erosion algorithm which discards material exceeding a (user-defined) strain criterion. Experience showed that this material is eroded before material phase change occurs, so although this material plays a minimal role in determining subsequent evolution of the impact crater, it is still significant when considering energy partitioning. Use of the Lagrangian processor for this investigation was therefore precluded. The ALE processor imposes a Lagrangian surface on a semi-Eulerian material interior, and so does not allow the generation of ejecta although it allows 'exact' tracking of material interfaces. For these reasons, the Eulerian processor was selected, which in turn limited the calculations to two dimensions (the 3D version of the code does not yet incorporate an Eulerian processor) and normal incidence particles.

For the range of velocities to be considered, material phase change will occur. The Tillotson equation of state was thus used (Tillotson, 1962), with the Johnson-Cook (Johnson and Cook, 1983) material strength model which allows for the important effects of strain and strain rate hardening and thermal softening of material.

3.4.1.1. Verification and Cross-calibration of Hydrocodes

3.4.1.1.1 Verification of AUTODYN

AUTODYN has been extensively verified for impact velocities up to 2.5 kms^{-1} (e.g. Holland et al., 1990). For this work, and for other research topics being pursued by the University of Kent, verification had to be extended to much higher velocities.

Verification using the Lagrangian processor was performed initially, by comparison of crater diameters with experimental data published by Stradling et al. (1992) (see Workpackage P2). This established that the adopted material parameters (see Appendix B) enabled good results to be achieved with the choice of an appropriate erosion strain.

The same material parameters were used for the Eulerian calculations described here. It is, of course, possible to 'tweak' material parameters to fit the results to any chosen verification data set. However, in the absence of any physical justification for changing parameters it was deemed preferable to make no changes, to establish the precision of the simulation results for which verification is possible (particularly crater dimensions) and to bear this precision in mind for those parameters for which verification is not possible.

AUTODYN simulations of a 1 μm iron particle impact on semi-infinite aluminium 2024 were performed for impact velocities in the range 2-30 kms^{-1} and the final dimensions of the craters measured. Figure 3.1 shows a comparison of crater

Figure 3.1. Crater Diameters
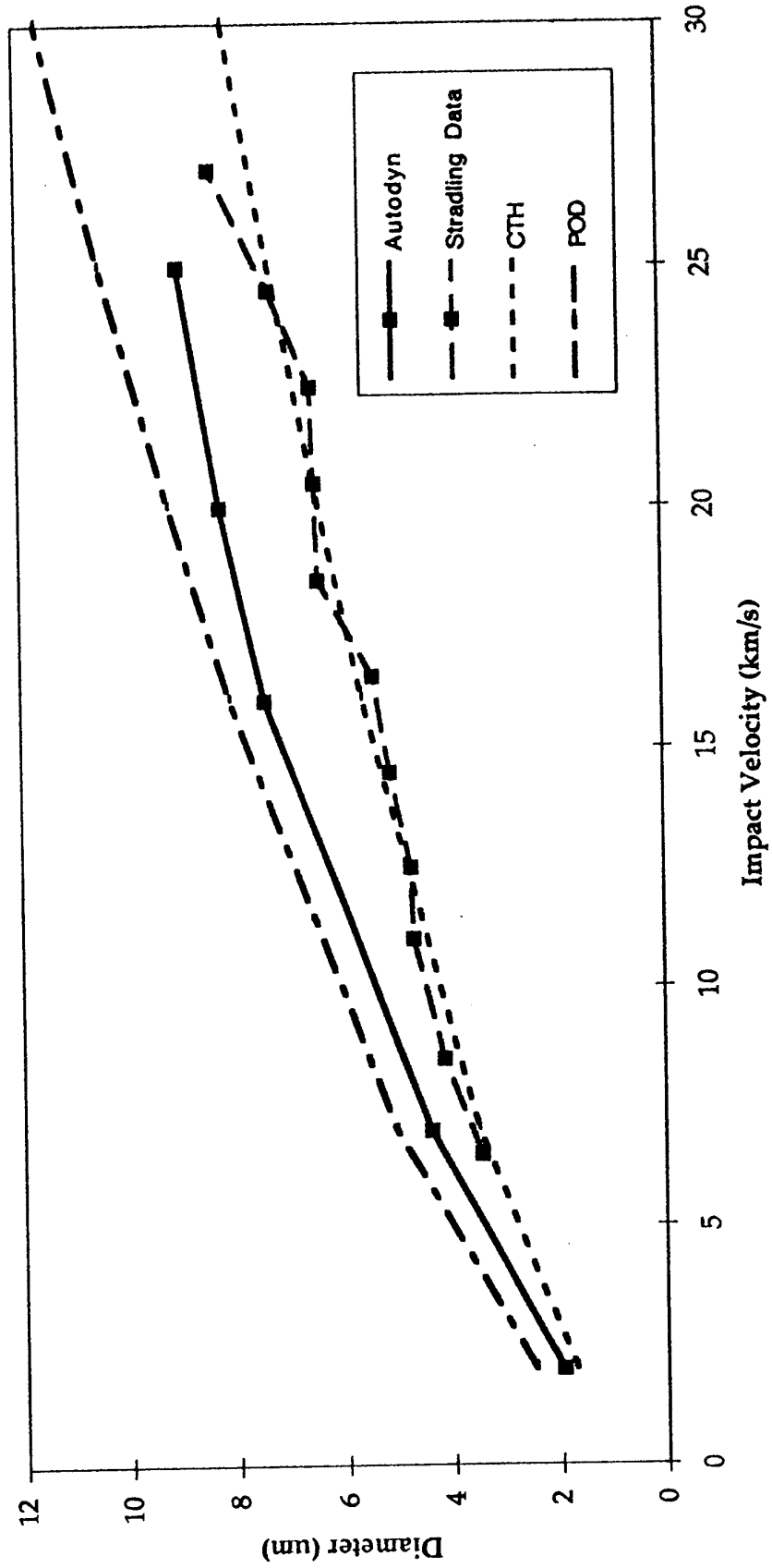
diameter with other sources of data; Figure 3.2 shows a similar comparison for crater depth.

The experimental diameters shown in Figure 3.1 (Stradling et al. 1992) are the average diameters of craters observed in a finite (but narrow) velocity range. Since the experiments were performed on an electrostatic accelerator facility, different particle sizes pertain to the different velocities: the published results have thus been scaled to the 1 μm projectile used in the AUTODYN runs. The Cour-Palais equation (Cour-Palais, 1987) is an empirical fit to an extensive set of experimental data. The 'POD' depth and diameter equations (Watts et al., 1993) are based on a theoretical analysis of crater formation. The CTH equations are empirical fits to the data derived from simulations of aluminium-on-aluminium impacts (Watts et al., 1993). In their study, the material parameters (density, yield strength) were varied in order to assess their influence on the crater dimensions, which allows us to use the same equations even though we have iron projectiles. The McDonnell and Sullivan equation (McDonnell and Sullivan, 1992) is an empirical perforation equation giving the maximum foil thickness that is penetrated at a given velocity. Conversion to a crater depth in a semi-infinite target is achieved by scaling the foil thickness by a factor of 1.5. These cratering equations are given in Appendix C.

The AUTODYN results are broadly consistent with the other data for both crater diameter and depth. Agreement with the POD equations and the Cour-Palais depth formula are particularly good. The experimental crater diameters of Stradling et al. are lower than those obtained using AUTODYN or the POD equation, but here the target material was 'single crystal aluminium' rather than aluminium 2024. Without knowing the material properties of 'single crystal aluminium' it is hard to assess the difference this would make, although intuitively one may have expected <u>larger</u> craters due to a lower yield strength.

The CTH crater depth equation produces significantly lower values, particularly at higher velocities. The CTH diameter equation contains an unspecified exponent of the ratio of sound speeds in the two materials (see Appendix C) as this effect was not investigated in the study of Watts et al. Varying this value allows fits to be obtained to either the Stradling data (requiring a value of 2.5, shown in Figure 3.1) or the AUTODYN and POD predictions (requiring a value of 6).

The good correlation of the AUTODYN predictions of crater depth and diameter with other sources of data appears to merit a high degree of confidence in the results. The discrepancy of the CTH depth predictions may be explained by the fact that the predictive equation is based on a different material for the impacting particle - a true comparison should be achieved by performance of directly comparable simulations, using the same materials and material properties, and similar mesh definitions.

However, Figure 3.2 shows that AUTODYN predicts a lower velocity dependence for crater depth than is given by any of the predictive equations. The effect of this is clearly seen in a plot of crater depth:diameter ratios (Figure 3.3). AUTODYN predicts a much larger depth:diameter ratio at low velocities, and the opposite trend with increasing velocity: the ratio reduces in the case of the AUTODYN predictions and increases for the POD equations. Since the diameters predicted by the
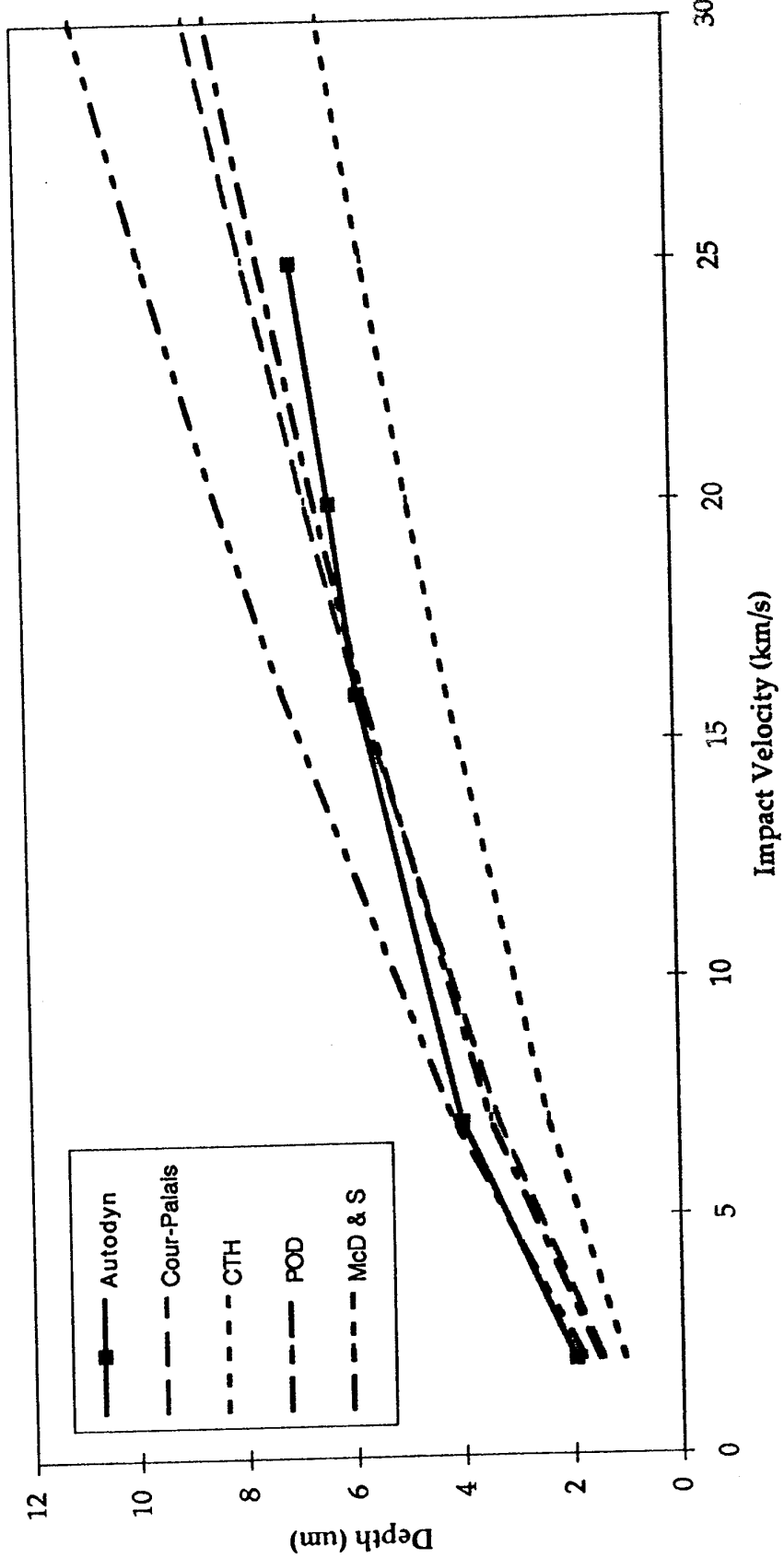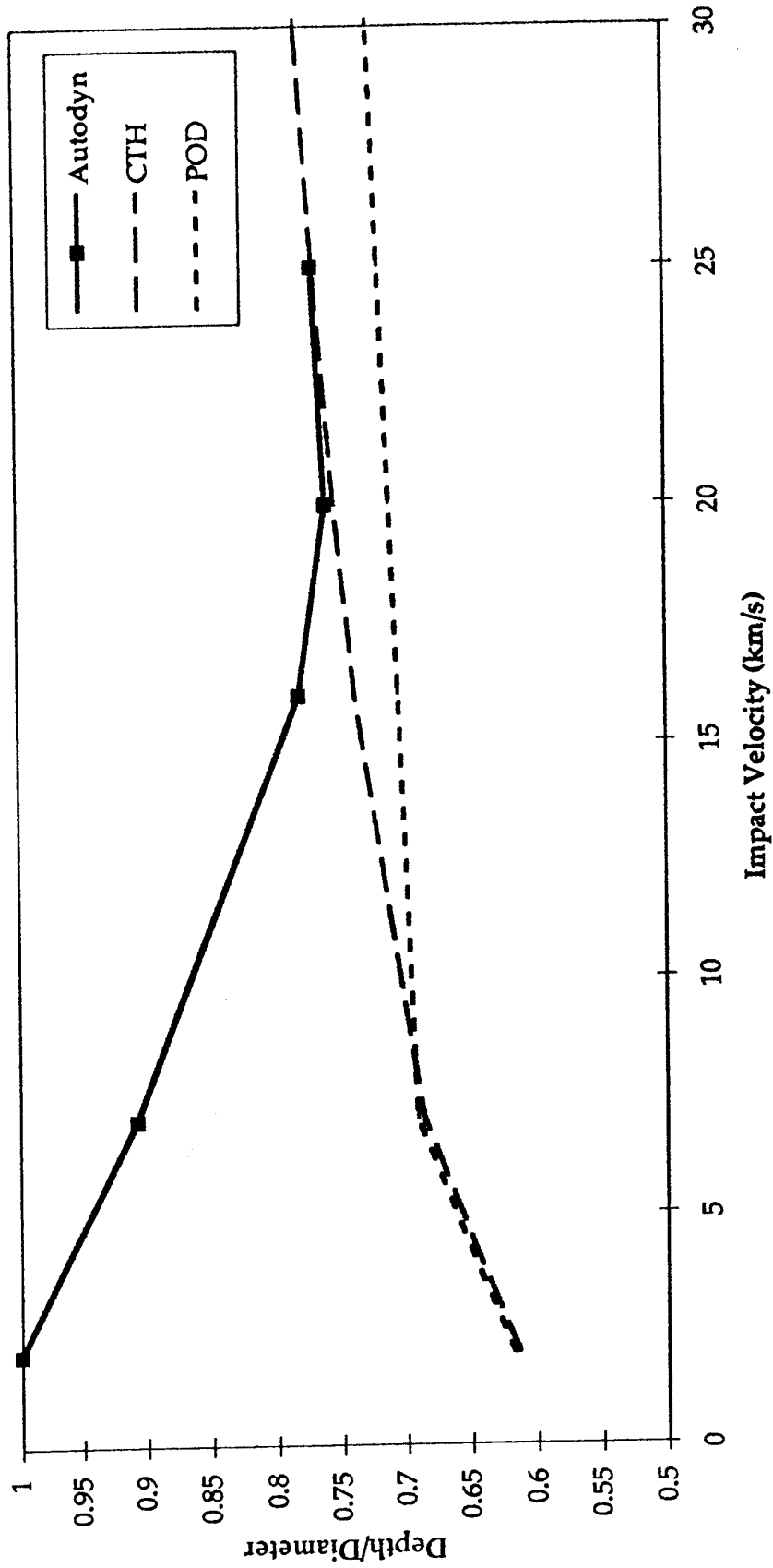
Figure 3.2. Crater Depths

Figure 3.3. Crater Depth to Diameter Ratios vs Impact Velocity

CTH equation are set by the arbitrary choice of the velocity-of-sound exponent, the absolute value of the depth:diameter ratio is also arbitrary, but the trend with increasing velocity is not, and is again upward.

The trend of increasing depth:diameter ratio with increasing velocity in the case of the POD and CTH equations is evident from the formulation of the equations (see Appendix C) - the velocity exponent of the depth equation is greater than that of the diameter equation in each case. The opposite trend predicted by AUTODYN has been reported elsewhere (McDonnell et al. 1993). The question arises as to which trend is 'correct'. Intuitively one may expect the crater to tend towards hemispheric (i.e. depth:diameter ratio of 0.5) at high velocity, which implies a reducing ratio as found with AUTODYN, but the theoretical analysis of Watts et al (1993) gives the reverse dependence. In a recent paper (Shanbing et al, 1994) experimental results are presented which support the AUTODYN results. A decreasing depth-to-diameter ratio is observed for steel impacts on aluminium and copper and an increasing ratio for aluminium impacts on steel and for impacts of any materials on the same material. For each projectile-target system the ratio tends to 0.5 at high velocity. The implication of this is that the velocity exponent of cratering equations must also depend on the material parameters, or that use of 'ground state' material properties is not appropriate at all velocities.

The discrepancy between the AUTODYN results and the other predictions is thus not of concern and the reliability of the crater depth and diameter predictions of AUTODYN suggest that reasonable confidence can be placed in the results obtained from the simulations that will be used for deriving information on the energy partitioning in impact events.

3.4.1.1.2 Cross-Calibration of Hydrocodes

Some hydrocode cross-calibration has been achieved by the comparison of AUTODYN with CTH results described in the section above. However, the CTH data are in the form of empirical equations describing trends observed in a series of runs of aluminium-on-aluminium impacts with varying impact velocity and material parameters. For a true cross-calibration, identical problems must be run using identical material parameters and simulation geometries. Such runs using CTH are planned for the near future, but have not yet been implemented.

3.4.1.1.3 Further Observations

Although the primary objective of this study is derivation of data pertaining to energy partitioning, and the code verification is based on comparison with data on final crater dimensions, a by-product of the AUTODYN simulations performed is the time profile of the development of the crater. It is interesting to look at this data in the form of the evolution of the depth:diameter ratio through the impact process. This is shown in Figure 3.4 for impact velocities of 2, 7, 16, 20 and 25 kms^{-1}. The depth is defined as the depth of the cavity in the target material (the particle material within the crater is omitted). At the end of the calculation time this is equal to the crater depth as the thickness of particle material lining the crater becomes negligible except

Figure 3.4. Depth to Diameter Ratio Evolution
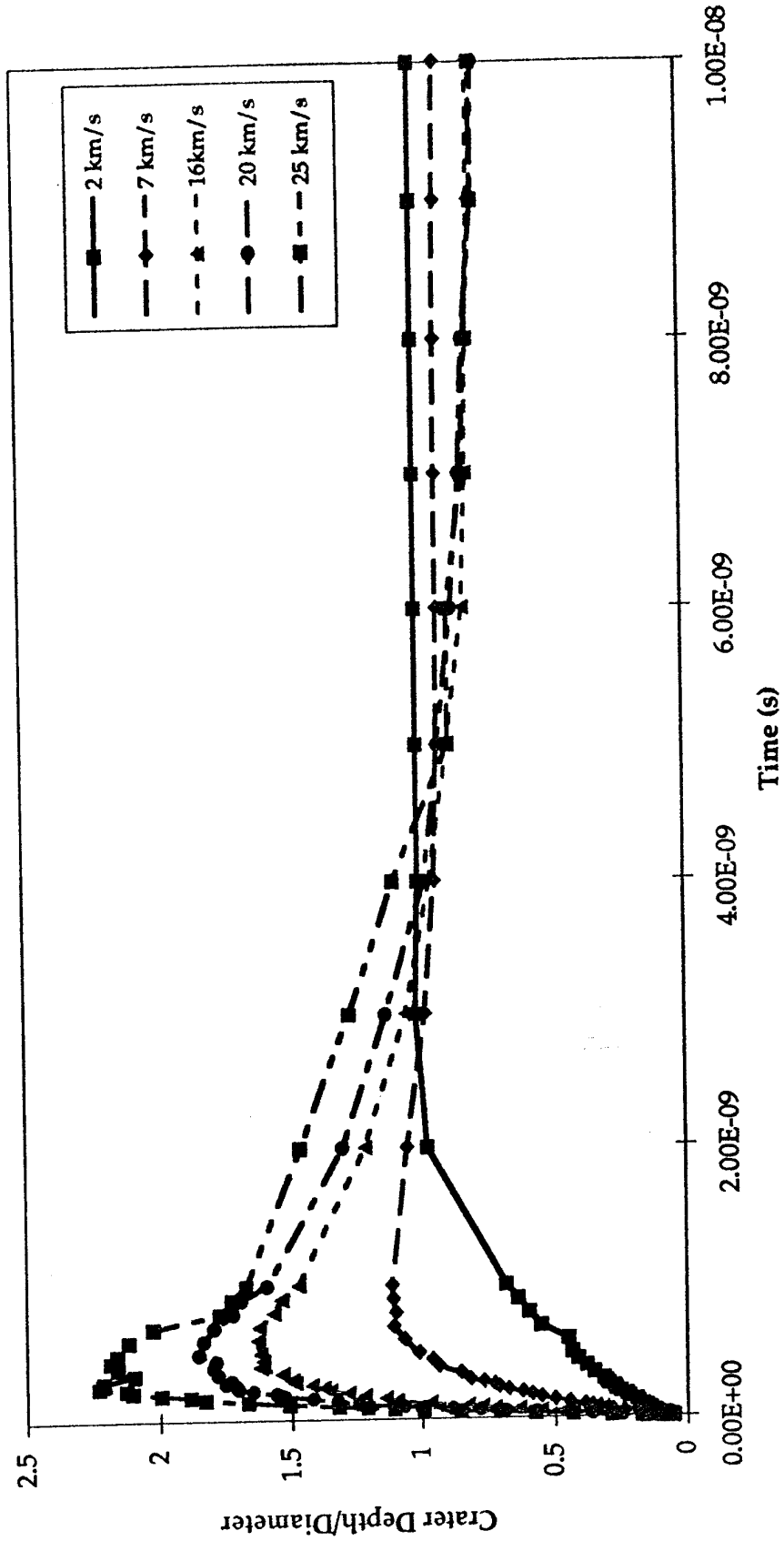
in the case of the 2 kms^{-1} impact. The diameter is defined as the smaller of the width of the entrance aperture or the width at the original surface plane of the target.

The time profiles at each velocity follow a characteristic form. As the particle penetrates the target surface the crater diameter increases rapidly to the diameter of the particle while the depth increases much more slowly. The depth:diameter ratio is thus small. Once the particle has fully penetrated the target surface, the depth is excavated much more rapidly than the diameter expands, and so the ratio rises. However, the crater depth reaches its final value while the crater diameter is still expanding, so the ratio then decreases to its final value when the crater has 'frozen'. The peak depth:diameter ratio increases with increasing impact velocity, and the time at which it occurs decreases. The final value decreases from 1.00 at 2 kms^{-1} to 0.76 at 20 kms^{-1}. This may be the limiting value for high velocity as there is no further reduction at 25 kms^{-1}, although runs at higher impact velocities are required to confirm or refute this.

3.4.1.2 Energy Partitioning Measurements

The following parameters pertaining to energy partitioning have been derived:

i) peak local internal energy and temperature in the particle and the target;
ii) material phase change in the particle and target;
iii) characteristic temperature of the particle and target vapour;
iv) final internal energy of the particle and target;
v) ejecta kinetic energy;
vi) ejecta momentum.

3.4.1.2.1 Peak Internal Energy

The highest local value of the internal energy and temperature has been recorded as a function of the impact velocity. The results are shown in Figures 3.5 and 3.6.

The peak values of internal energy and temperature occur approximately 10^{-11} s after the impact. The dependence of this time on impact velocity has not been investigated in detail, but can not be larger than a factor of 2 over the velocity range covered. The peak temperatures exceed the melting points of both target and particle at velocities above 2 kms^{-1}, exceed the boiling points for velocities above 7 kms^{-1}, and reach extremely high values (66,000 and 35,000 K respectively) at 30 kms^{-1}. However, this does not imply that vaporisation of the material occurs at all these velocities as the peak temperatures occur in the region of the peak pressures and compressions at the particle-target interface. Material phase change, if it occurs, occurs at the periphery of the particle-target interface where the temperatures reached are lower but the pressures and compressions are also low.
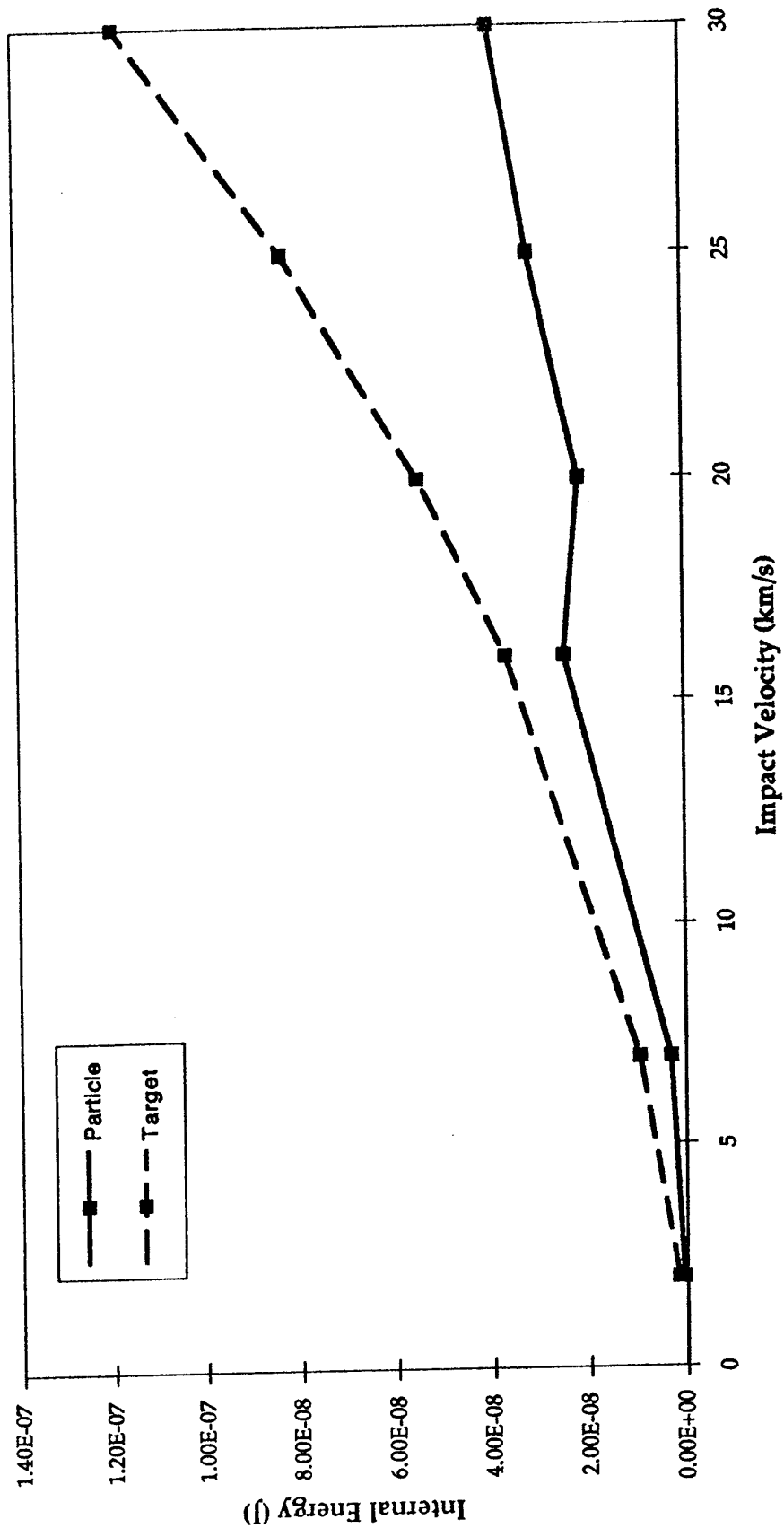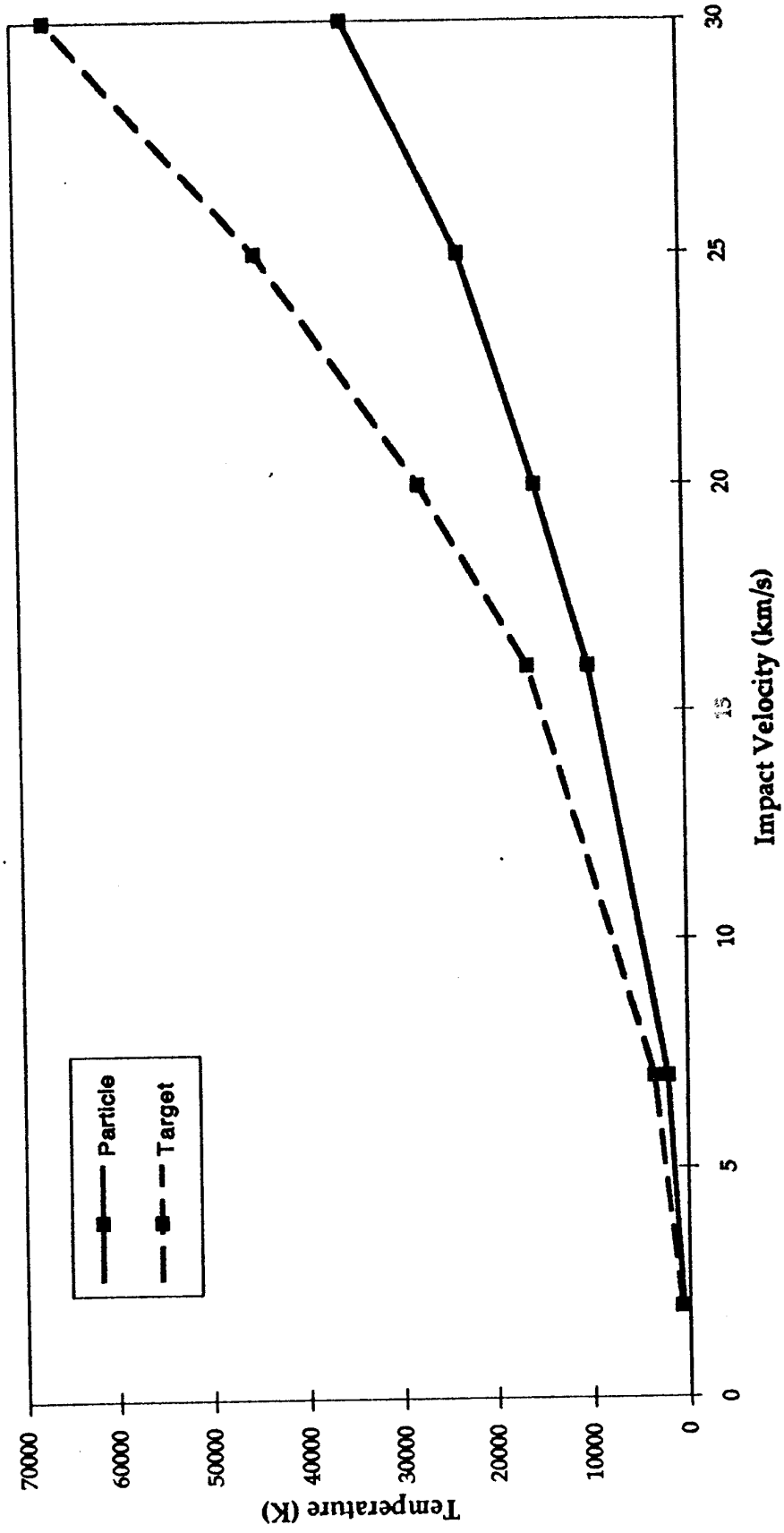
Figure 3.5. Peak Internal Energy

Figure 3.6. Peak Temperatures

34

3.4.1.2.2 Material Phase Change

As mentioned in Section 3.4.1, the Tillotson equation of state was used in this study. This is a two-phase model (solid and gas), but uses four mathematical descriptions of material in different states, which may be loosely thought of as:

i) 'ground state' - unshocked material - elastic;
ii) shocked material that will return to the ground state - 'plastic';
iii) shocked material with no strength - 'liquid';
iv) ideal gas.

It must be stressed that these interpretations of states i to iii are just visualisations and are not physical or even mathematical. The transition from state iii to state iv is, however, physical, and represents the onset of vaporisation.

The peak phase (expressed numerically) experienced by the projectile and target material is shown in Figure 3.7. For the aluminium target, the onset of vaporisation occurs between 20 and 25 kms⁻¹, while for the iron particle it occurs between 25 and 30 kms⁻¹. This threshold velocity for the production of iron vapour is in line with experimental observations using time-of-flight spectroscopy of impact plasma (Section 3.4.2.1). The threshold velocity for aluminium is difficult to establish experimentally because of the ambiguity between aluminium and C_2H_3 (both mass 27) in impact plasma mass spectra. The hydrocarbon is a readily formed and stable molecule resulting from vaporisation of contaminants which are very difficult to eradicate in a practical system.

3.4.1.2.3 Vapour Temperature

An interesting parameter for comparison with experimental results is the temperature of the evolved vapour, which can also be estimated from experimental measurements of impact plasma characteristics. The characteristic temperature (i.e. the average over time and location) has been derived separately for the projectile and target material, and is shown in Figure 3.8. Characteristic temperatures are of the order 10^4 K, considerably below the peak temperatures experienced by the target and particle material in other locations. Further implications of these results will be discussed in Section 3.4.2.1.

3.4.1.2.4 Final Internal Energy

The total internal energy of the system is monitored by AUTODYN throughout the calculation. However, this includes not only the energy dissipated in heating material ('thermal energy') but also the work done overcoming material strength (i.e. in comminution and compaction). The final values of the internal energies of the particle and target material, and the sum of the two, are expressed in Figure 3.9 as a percentage of the initial kinetic energy of the particle, that is, of the total energy in the system.
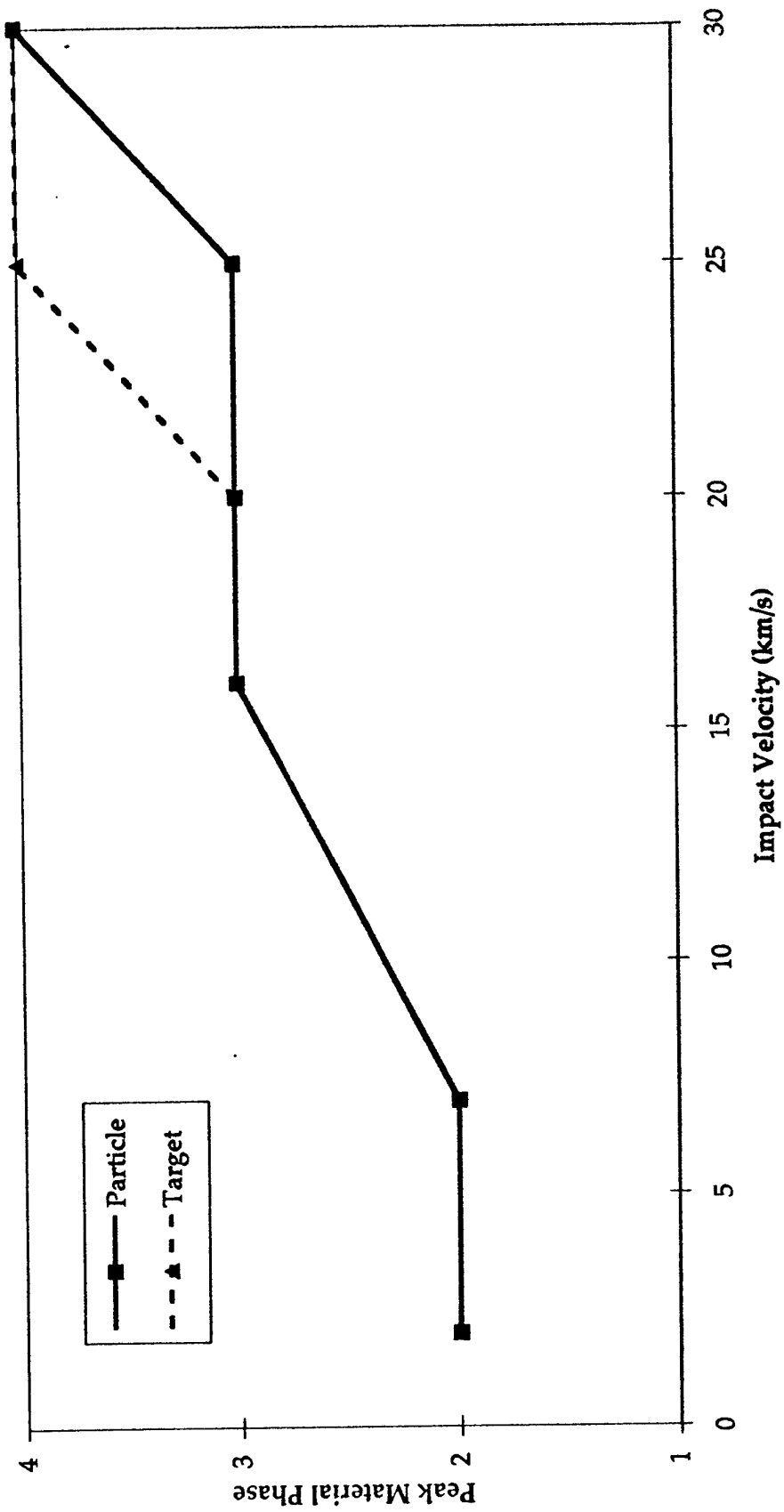
Figure 3.7. Tillotson Phase

36

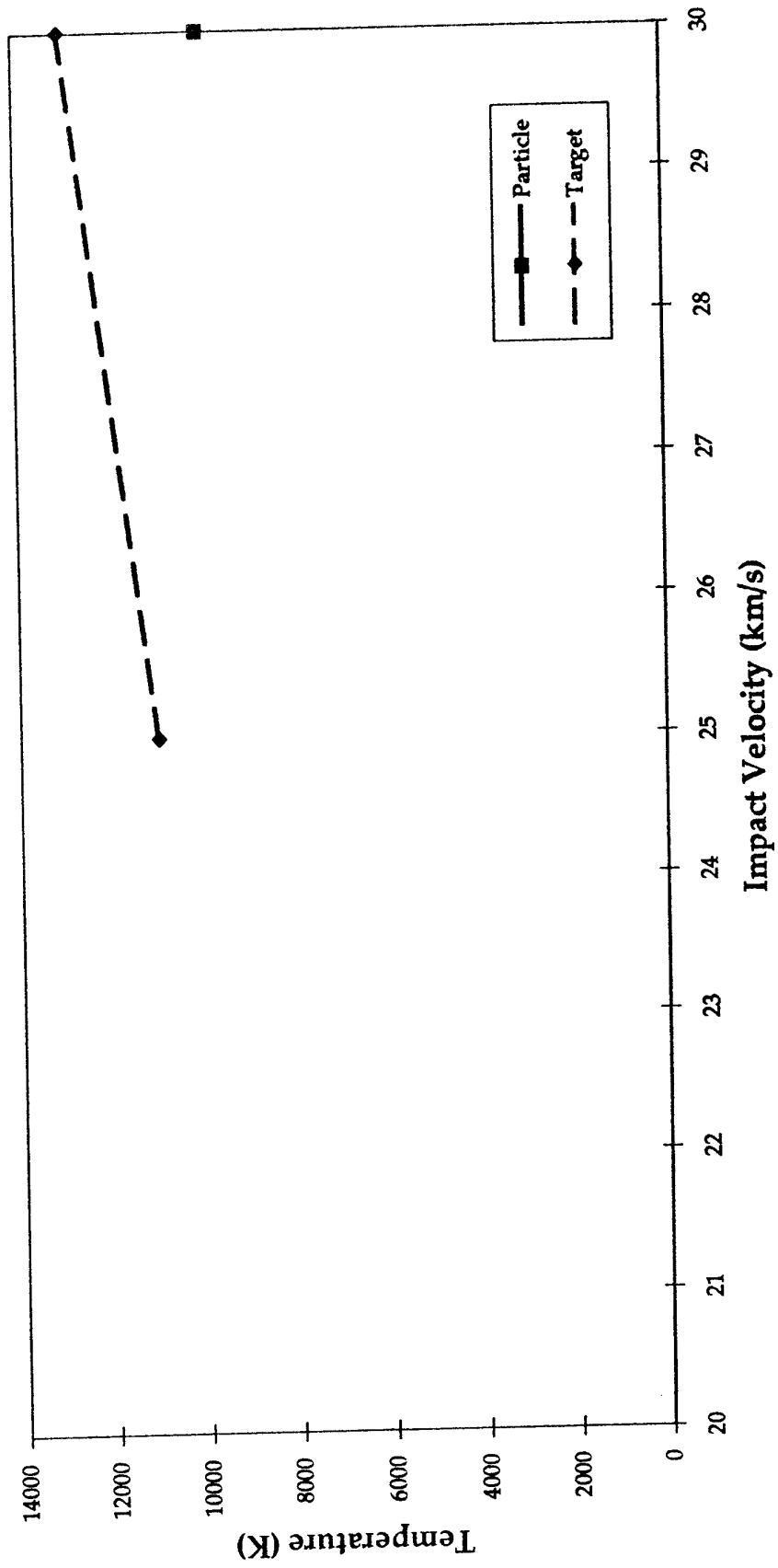Figure 3.8. Characteristic Vapour Temperatures

Figure 3.9. Final Internal Energy
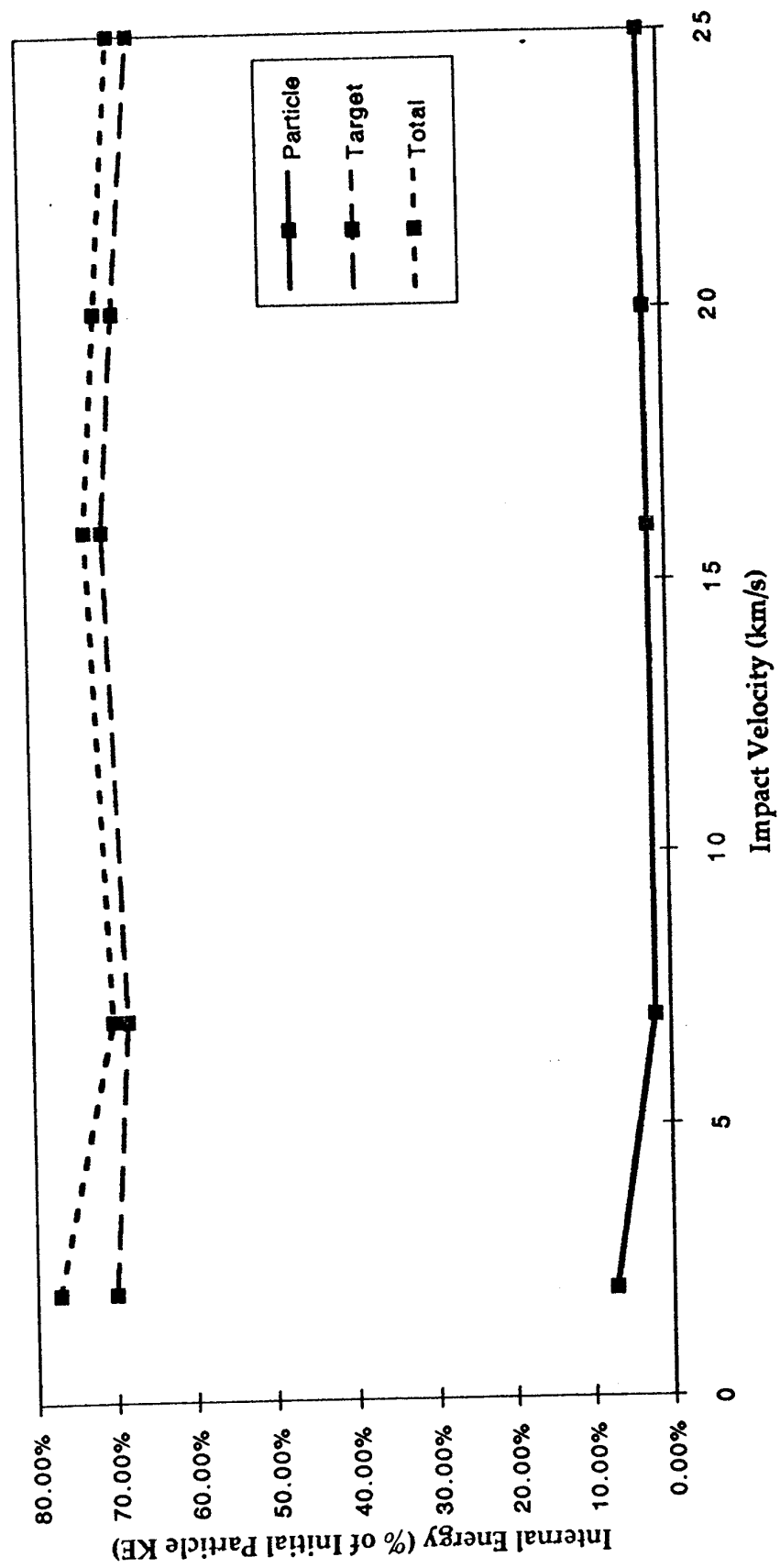
The dominance of the target internal energy over that of the particle is, of course, simply reflecting the much greater mass of target material than particle material involved in the impact process at these high velocities. This ratio is lower at lower velocity (particularly at 2 kms^{-1}) due to the smaller volume of target material affected.

There is surprisingly little velocity dependence observed in the results, which are fairly consistent at around 70%. One would expect a significant increase in the 'thermal energy' passing from the subsonic through the supersonic impact velocity regime as the relative importance of the shock wave increases compared with the acoustic wave. However, this is apparently balanced by an inverse trend in the compaction/comminution energy. Variations in the energy in other paths is discussed below.

3.4.1.2.5 Ejecta Kinetic Energy

The ejecta kinetic energy is not directly monitored by AUTODYN, but can be deduced by two methods:

a) The ejecta particle masses and velocities can be measured manually. This gives a true measure of the kinetic energy in the ejecta observed, but since ejecta is produced in very late stages of the impact process (associated with the final forming of the crater lips, well beyond the time at which the crater itself has adopted its final dimensions) it is difficult to run a simulation for long enough to be sure of seeing all the ejecta. This method thus provides a lower bound to the true value.

b) AUTODYN does monitor the kinetic energy of the system. Initially this is the kinetic energy of the particle. As the impact proceeds and the energy is converted to other forms, the total kinetic energy falls, and asymptotically approaches a limiting value when all motion in the target has ceased. The remaining kinetic energy is that of the ejecta. The value of the asymptote is increasingly difficult to determine at higher velocities due to the greater computation time needed, and so the deduced values represent upper limits.

The absolute values of the ejecta kinetic energies are shown in Figure 3.10, and the values relative to the initial particle energy in Figure 3.11. For an impact velocity of 2 kms^{-1} no ejecta is produced, and so the recorded system kinetic energy is the residue in the bulk material. As would be expected, the absolute values show a strong velocity dependence, but the relative values do not, suggesting a value of ~2% throughout the velocity range. This value is low compared with studies of ejecta from brittle materials (such as the 40-50% reported for basalt and sand, (e.g. Housen at al., 1983, Fechtig et al., 1978)), but lower values would be expected for ductile materials. It should also be remembered that the production of ejecta by hydrocodes is not independent of the mesh grading and it is possible that a finer mesh may increase the ejecta production.

Figure 3.10. Ejecta and System Final Kinetic Energy
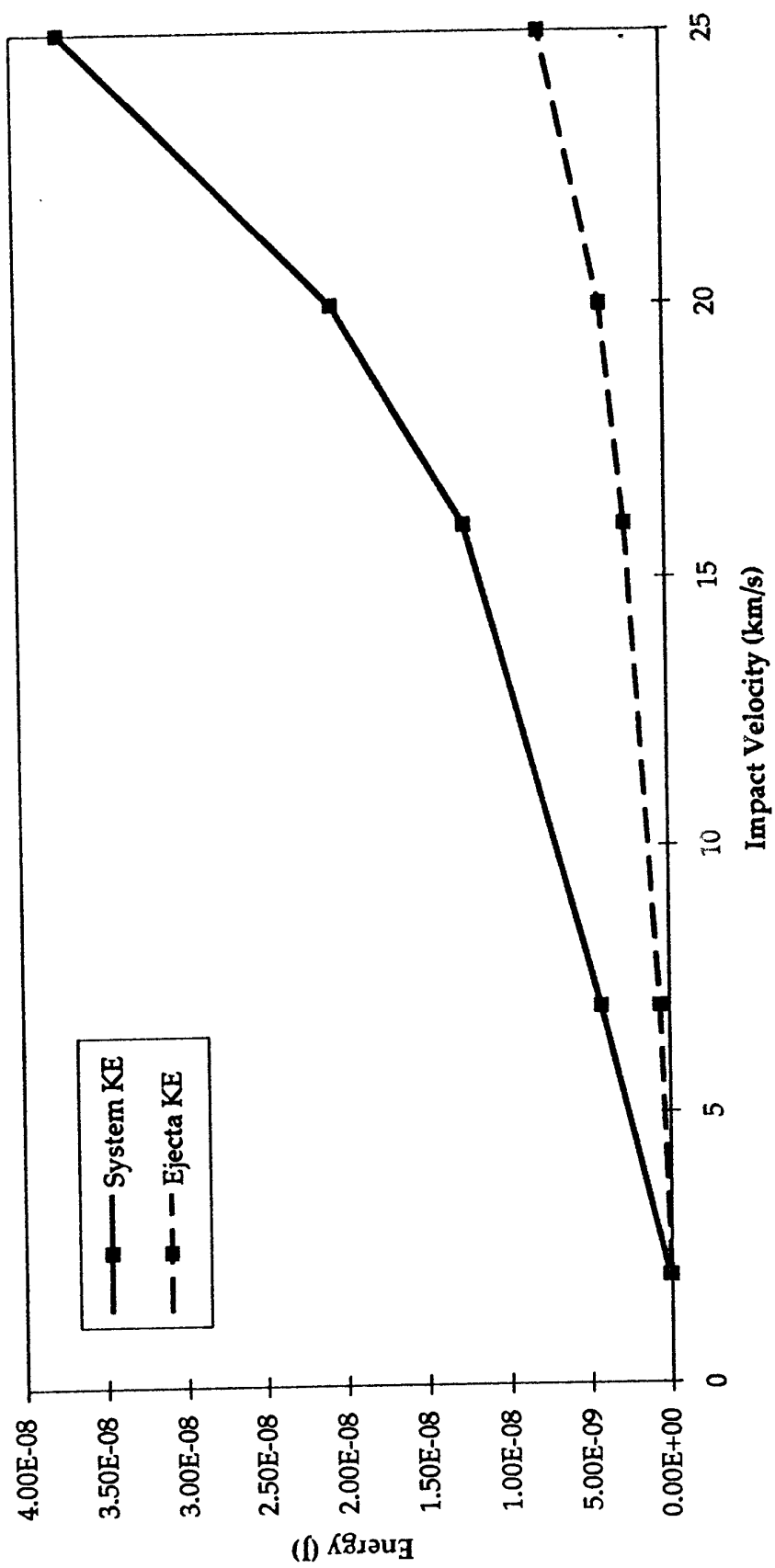
Figure 3.11. Ejecta Kinetic Energy
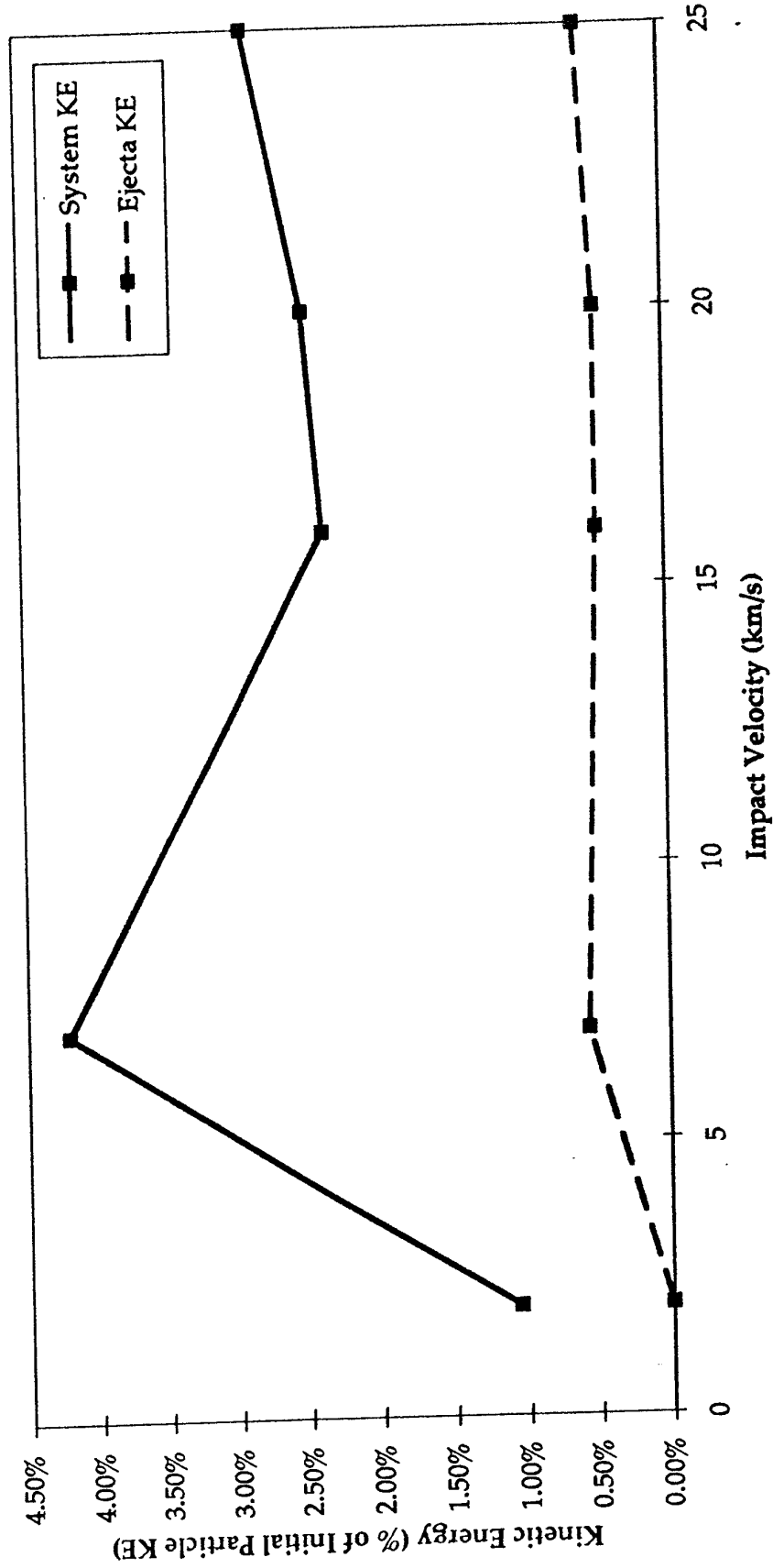
3.4.1.2.6 Ejecta Momentum

The ejecta momentum has also been calculated by two methods:

a) by manual investigation of identifiable ejecta particle masses and velocities ('Ejecta Momentum' in Figure 3.12), which represents a lower bound as per the ejecta energy measurement;

b) from the momentum tracking within AUTODYN ('AUTODYN' in Figure 3.12). This makes no distinction between ejecta momentum and that in the rest of the material, and thus provides an upper bound to the true value.

Figure 3.12, compares these derived values with momentum enhancement measurements of Slattery and Roy (1970) and Rembor (1993). As may be expected, the upper and lower bounds calculated here bracket both experimental data sets. Allowing the AUTODYN simulations to run for longer would cause the calculated values to converge. However, since investigation of momentum enhancement is not a primary objective of this study, and the simulations already take ~ 5 days to complete, this has not been attempted.

3.4.1.2.7 Summary

The data on energy partitioning that has been derived from these hydrocode studies is summarised in Figure 3.13. The velocity dependence of the internal and ejecta kinetic energies are shown, for the particle and target materials individually and for their sum. The energy in forms that can not be individually identified is shown by the curve 'Other'.

3.4.2 Experimental Measurements

Experimental measurements of energy partitioning have been performed using the 2 MV Van de Graaff dust accelerator facility at UKC. Much of the data used here was taken during the pilot tests described under the Workpackage P4 section of this report, other data was taken with comparable impact plasma experiments in the course of other investigations performed at UKC over the last few years (in particular during the design and development of a time-of-flight mass spectrometry system for the Cassini/Huygens mission).

Although the hydrocode simulations were performed for impacts on aluminium, for the reasons described above, most of the experimental work in the pilot tests has been performed for impacts on molybdenum as this is advantageous for light flash measurements. Some data has also been taken with aluminium and silver targets (see Workpackage P4).

The parameters that can be derived from experimental measurements are not the same as those that can be readily determined from hydrocode simulations. The yield of impact plasma and light can be measured directly, and the energies of the plasma ions can be derived by two different methods. One of these methods was

Figure 3.12. Momentum Enhancement

43

Figure 3.13. Energy Partitioning

Legend: Internal Energy, Particle Int. E, Target Int. E, Ejecta KE, Other

Y-axis: Percent (0.00% to 100.00%)
X-axis: Impact Velocity (km/s)

44

developed and applied to the analysis of the plasma produced by a single 94 kms⁻¹ impact. This method is precise but extremely time-consuming. The second method was developed during this study, and has been applied to a much wider data set. The second meth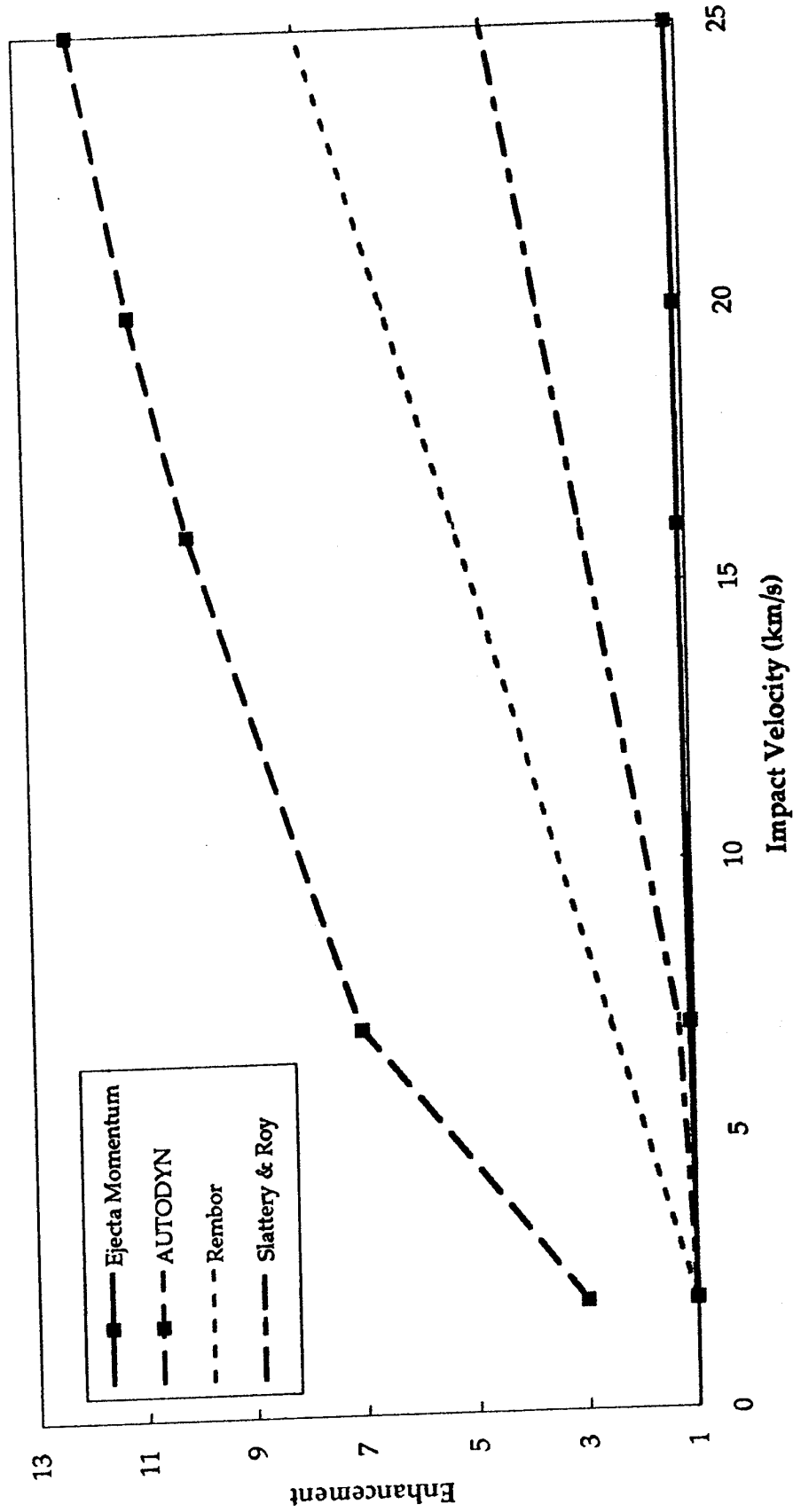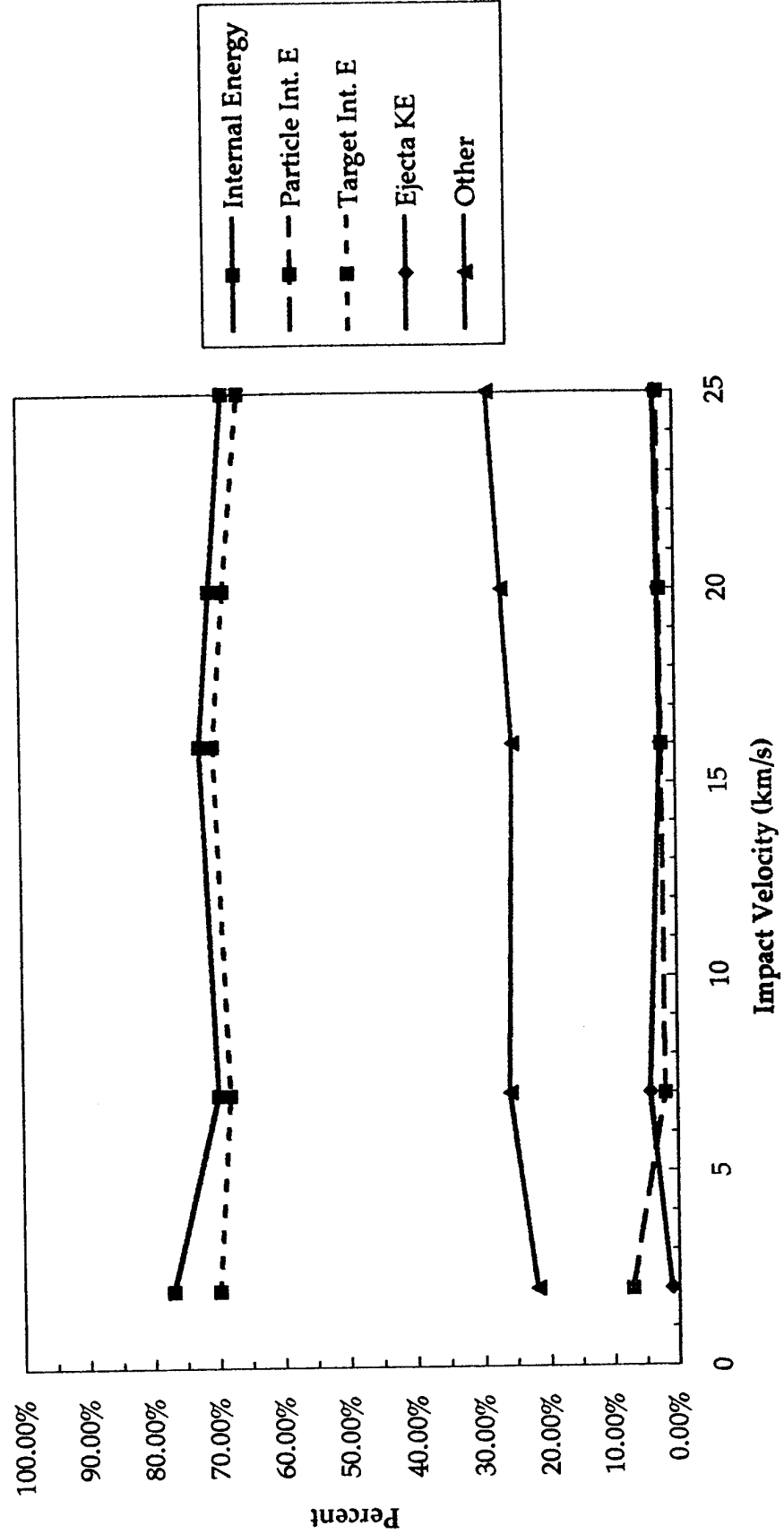od is described in Appendix D, the former has been described by Ratcliff and Allahdadi (1994), a preprint of which is included as Appendix E. Ejecta momenta can be derived from momentum enhancement measurements, and a new method has been developed to calculate ejecta energies.

3.4.2.1 Plasma Energies

3.4.2.1.1 Ion Species Characteristic Energies

The technique described in Appendix D has been applied to derive the energies of the ion species observed in 99 impacts of iron microparticles on molybdenum. The velocity range covered is from 1.63 to 42.1 kms⁻¹. The results are shown in Figure 3.14 for all the ion species consistently observed, namely hydrogen, carbon, sodium, "mass 27", potassium, calcium, iron and molybdenum. For greater clarity, Figures 3.15a-h show the results for each species individually. The data are averaged over velocity bins, and the error bars in both energy and velocity are the errors on the mean values. The iron and molybdenum ions observed are obviously from the impacting particle and the target respectively. The other elements are present either as impurities in the materials (at a parts-per-10,000 level) or as surface contamination. The curve labelled "Mass 27" could represent either aluminium (which may be present in the molybdenum as a contaminant), or perhaps more probably (or perhaps additionally) C_2H_3, a stable hydrocarbon cluster ion formed from organic contaminant material and which is commonly seen in impact mass spectra (Kissel 1994).

The occurrence of the different ion species are in line with expectation - sodium and potassium, and to a lesser extent calcium, (which are the most readily formed ions and which are almost impossible to eradicate as contaminants) are seen from velocities of 1.6 kms⁻¹ upwards, while the other species have higher velocity thresholds. The threshold velocities observed for each species are shown in Table 3.1. The two values given are the lowest velocity at which the line was observed and the velocity above which the line was consistently observed. Only one value is given for sodium and potassium as these velocities are the same. Those species with a question mark for the upper value are not seen consistently at any velocity covered, but this is influenced by their low yields which makes them difficult to identify reliably. The values in Table 3.1 may not be readily apparent from Figures 3.14 and 3.15 as only data with a statistically significant number of points in each bin is plotted.

Naively, one would expect increasing ion energies with increasing impact velocities, but this appears only to be the case for sodium and potassium ions at low (<10 kms⁻¹) velocities, which rise to peak values of 84 and 75 eV respectively. At higher velocities their energies fall. This may be associated with the onset of vaporisation of the other species, with the higher energy sodium and potassium ions, which are well past their creation velocity threshold, 'sharing' energy with the lower energy ions through collisions. This is inconsistent with the standard theory of impact plasma mass spectrometry which assumes a low density collisionless plasma separated rapidly by the intense electric field. However, the basis of this theory is

Figure 3.14 Average Ion Energies
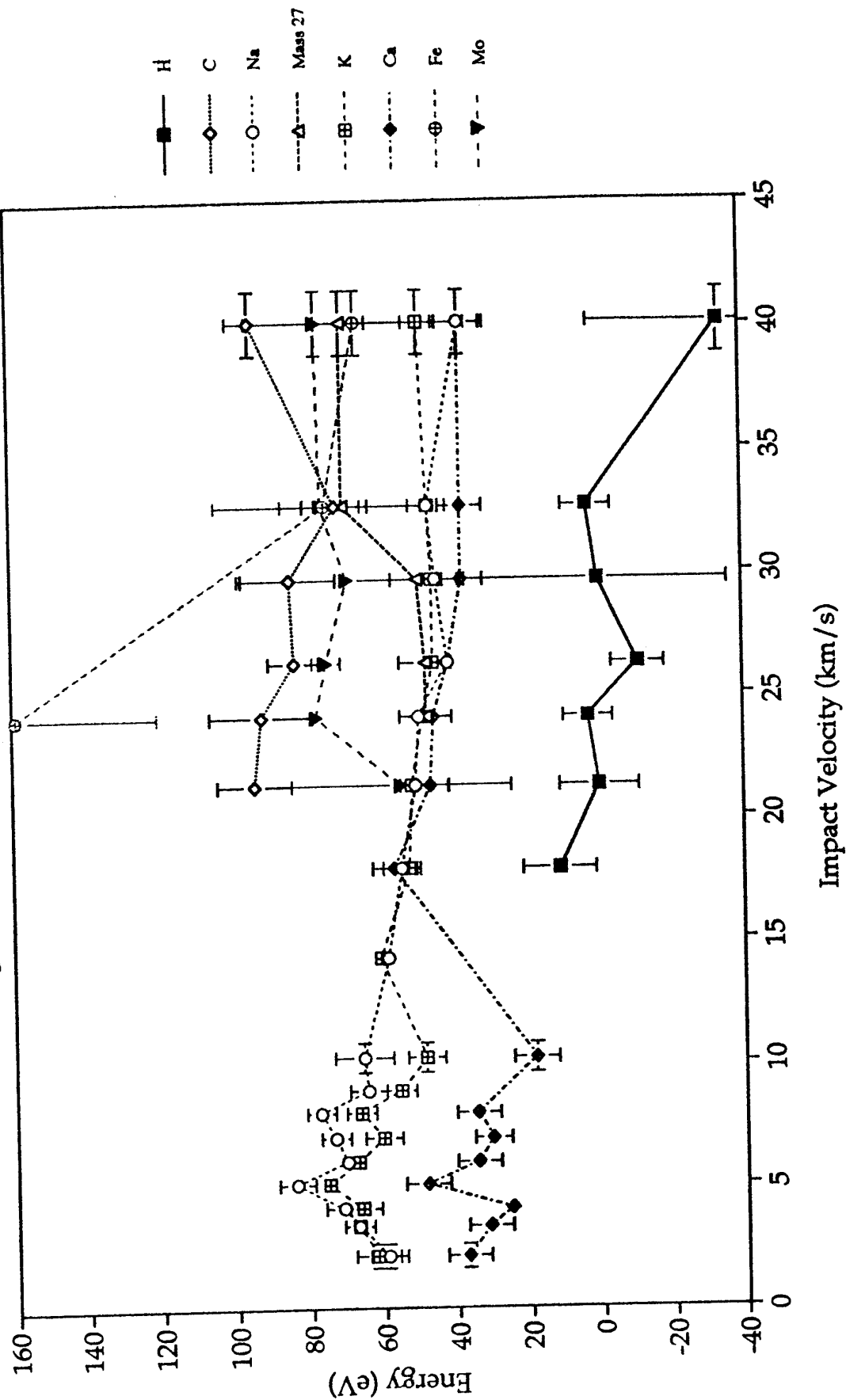
Figure 3.15a Hydrogen Ion Energy
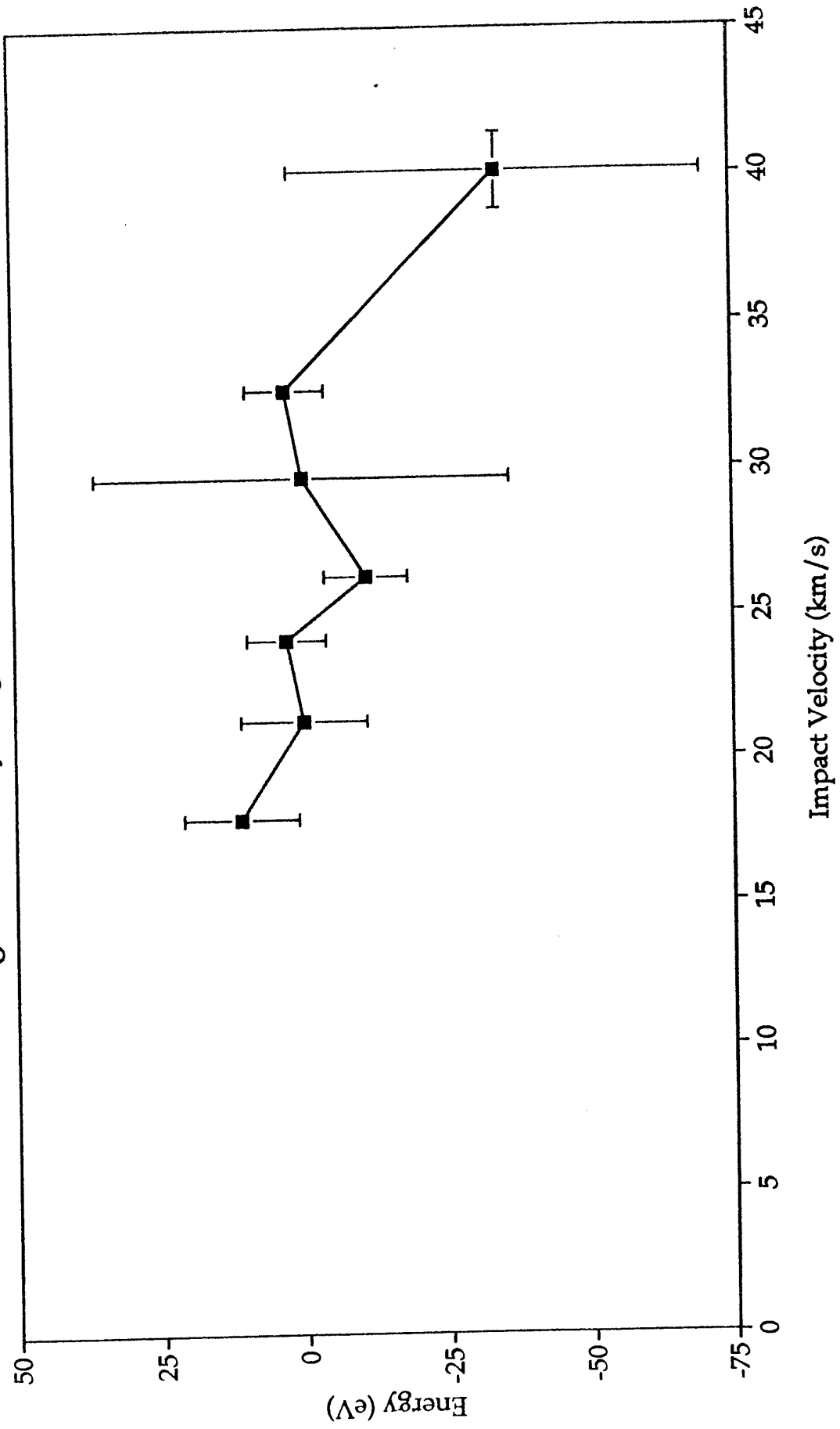
Figure 3.15b Carbon Ion Energy
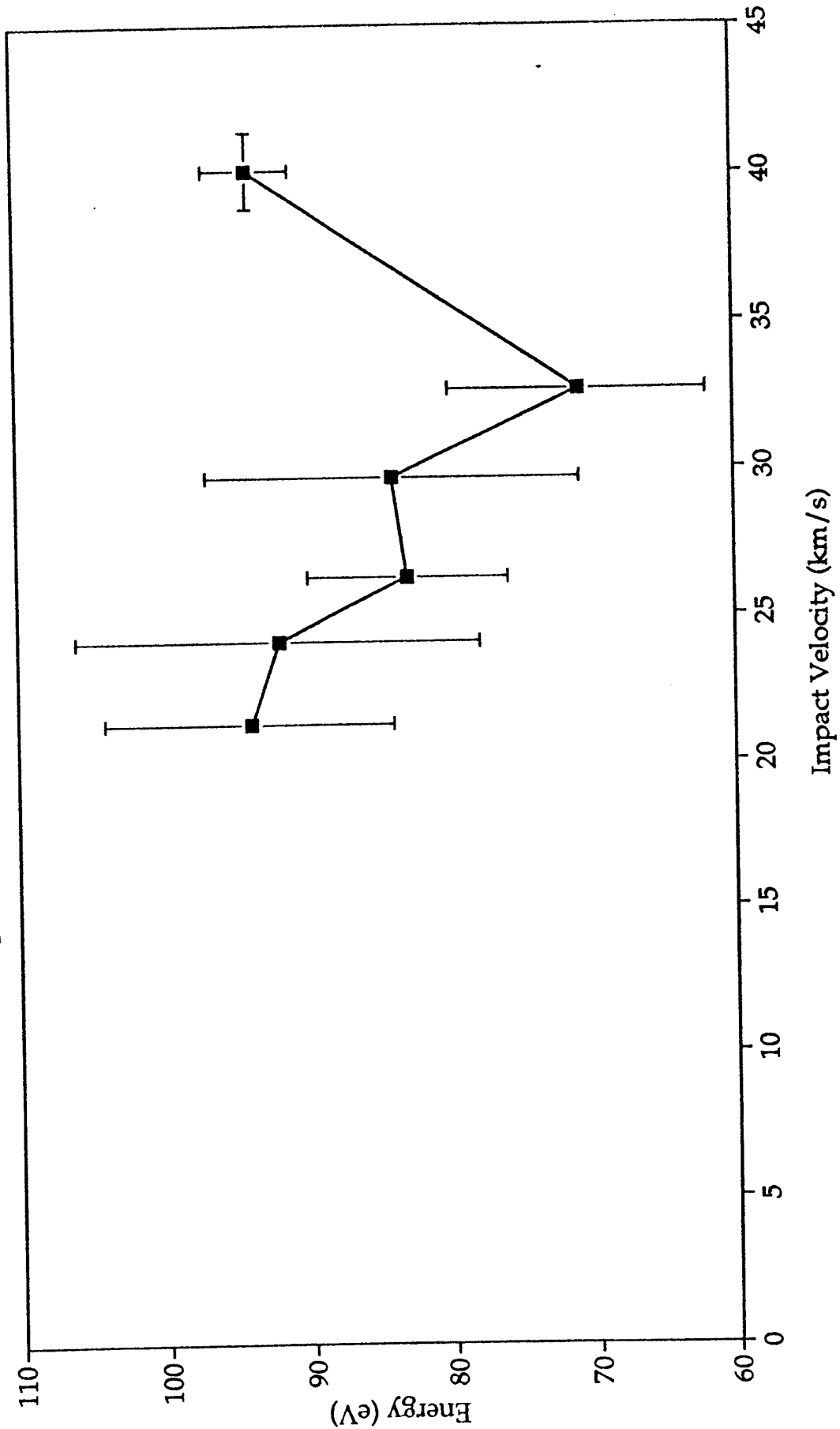
Figure 3.15c Sodium Ion Energies

Energy (eV) vs Impact Velocity (km/s)
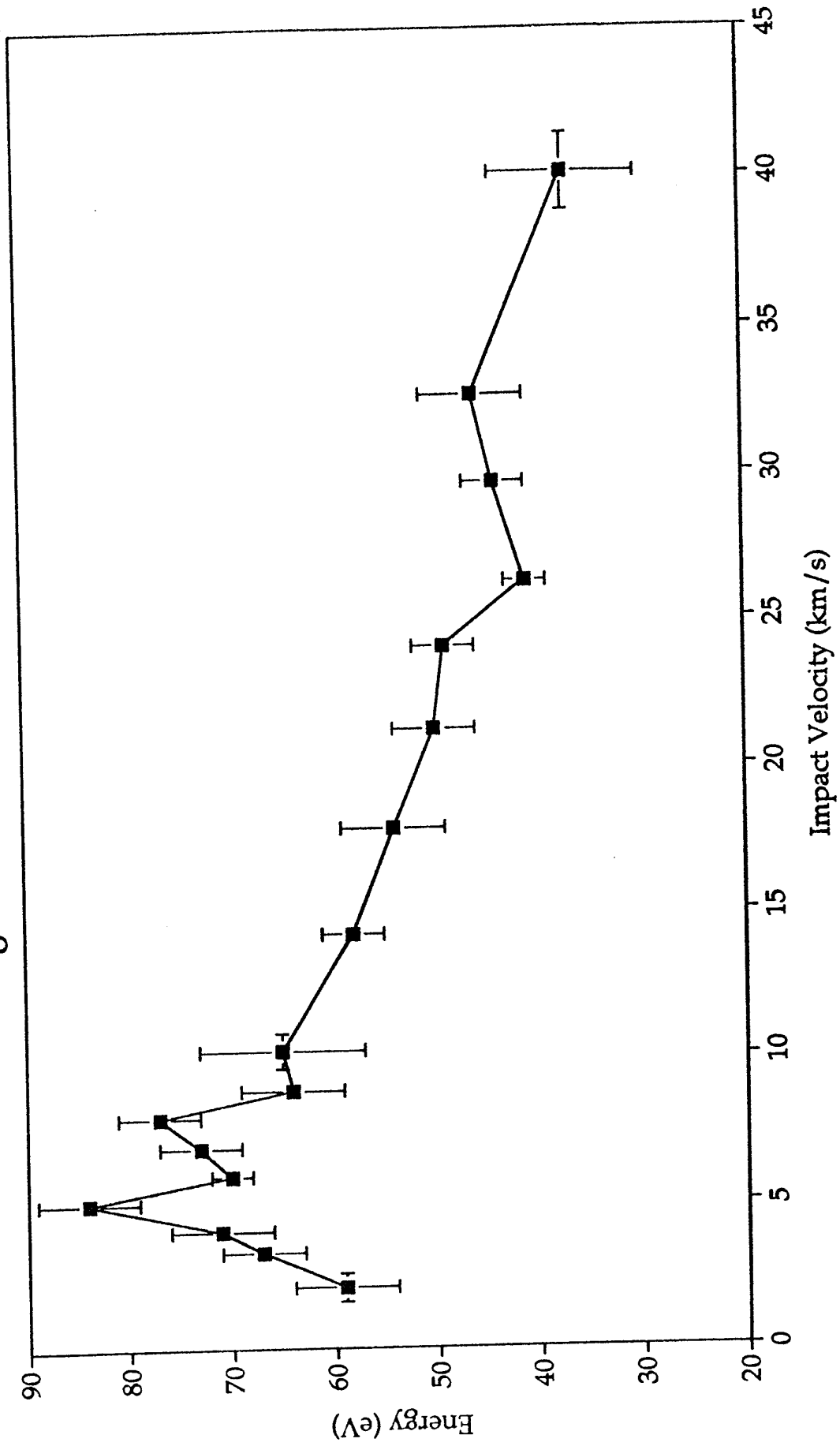
Figure 3.15d "Mass 27" Ion Energies
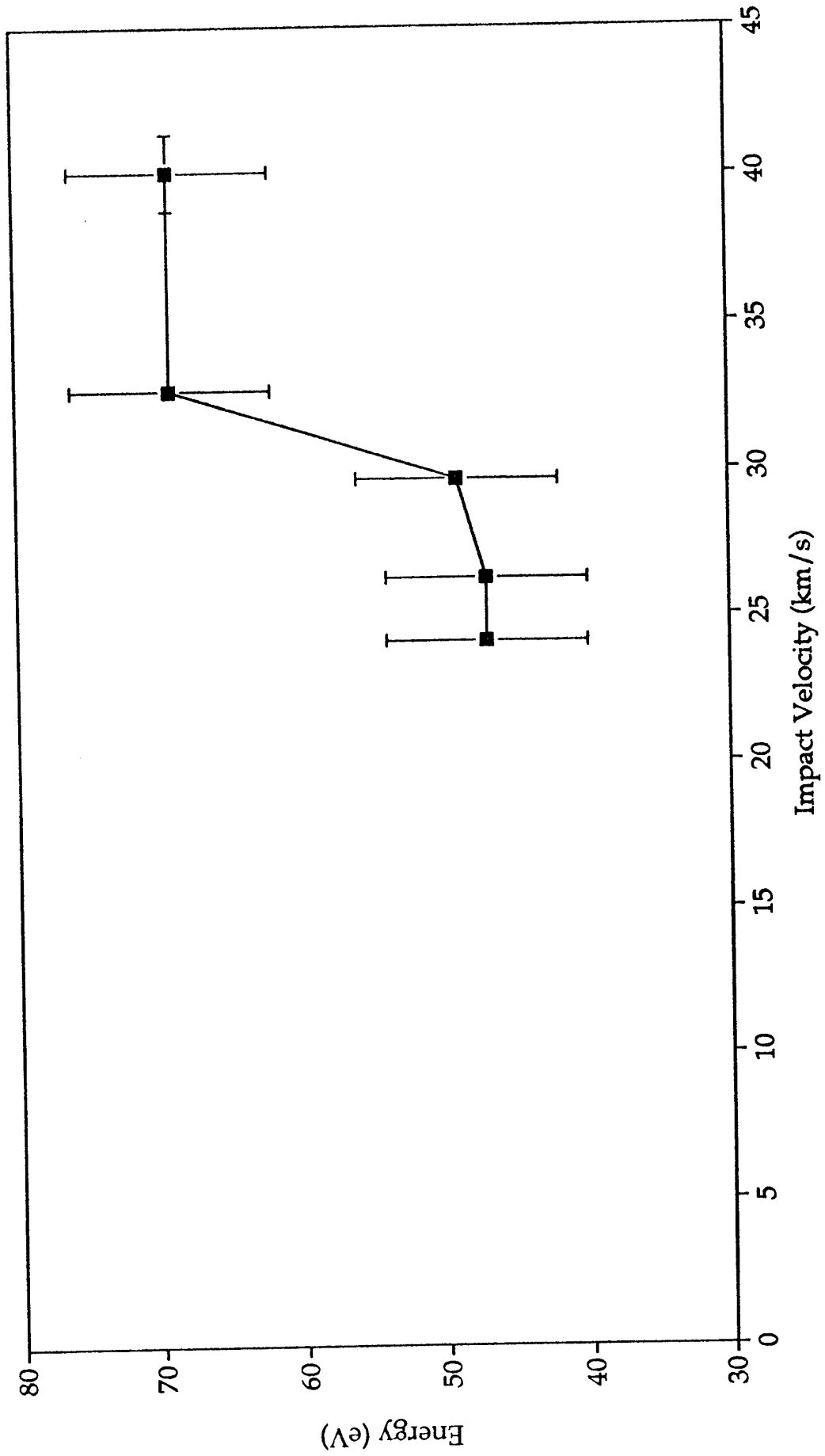
Figure 3.15e Potassium Ion Energies
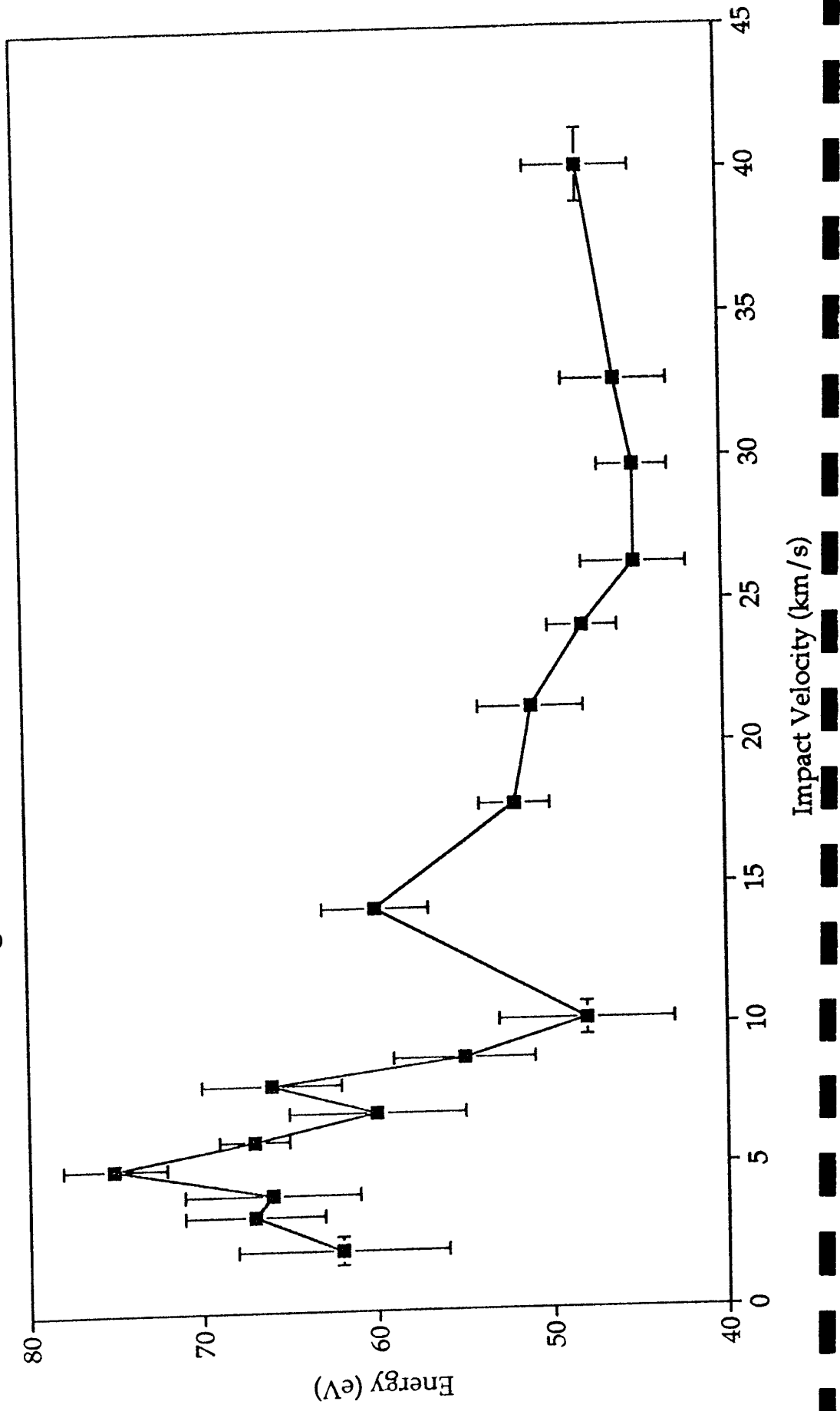
Figure 3.15f Calcium Ion Energies
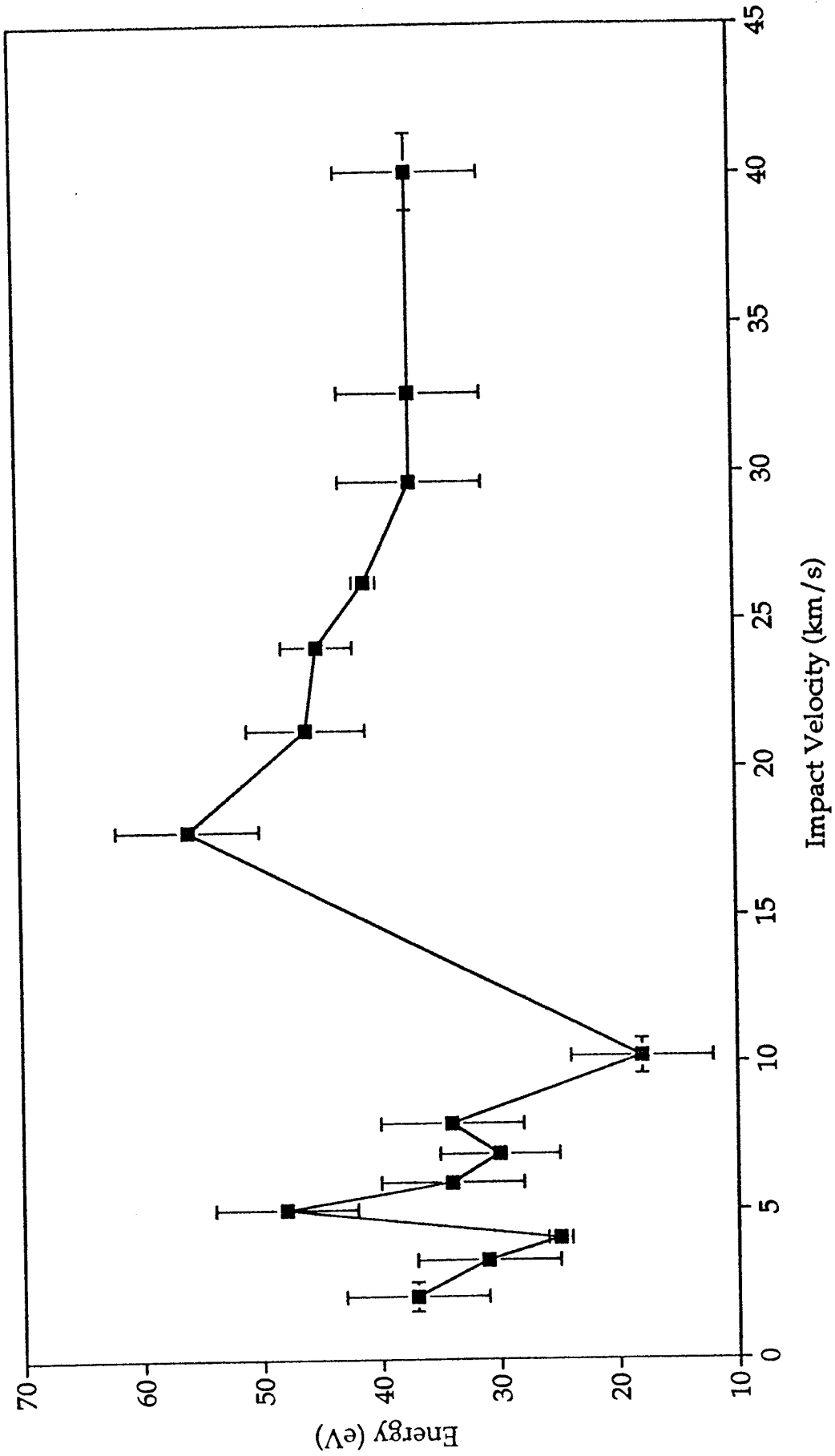
Figure 3.15g Iron Ion Energies

Energy (eV) vs Impact Velocity (km/s)
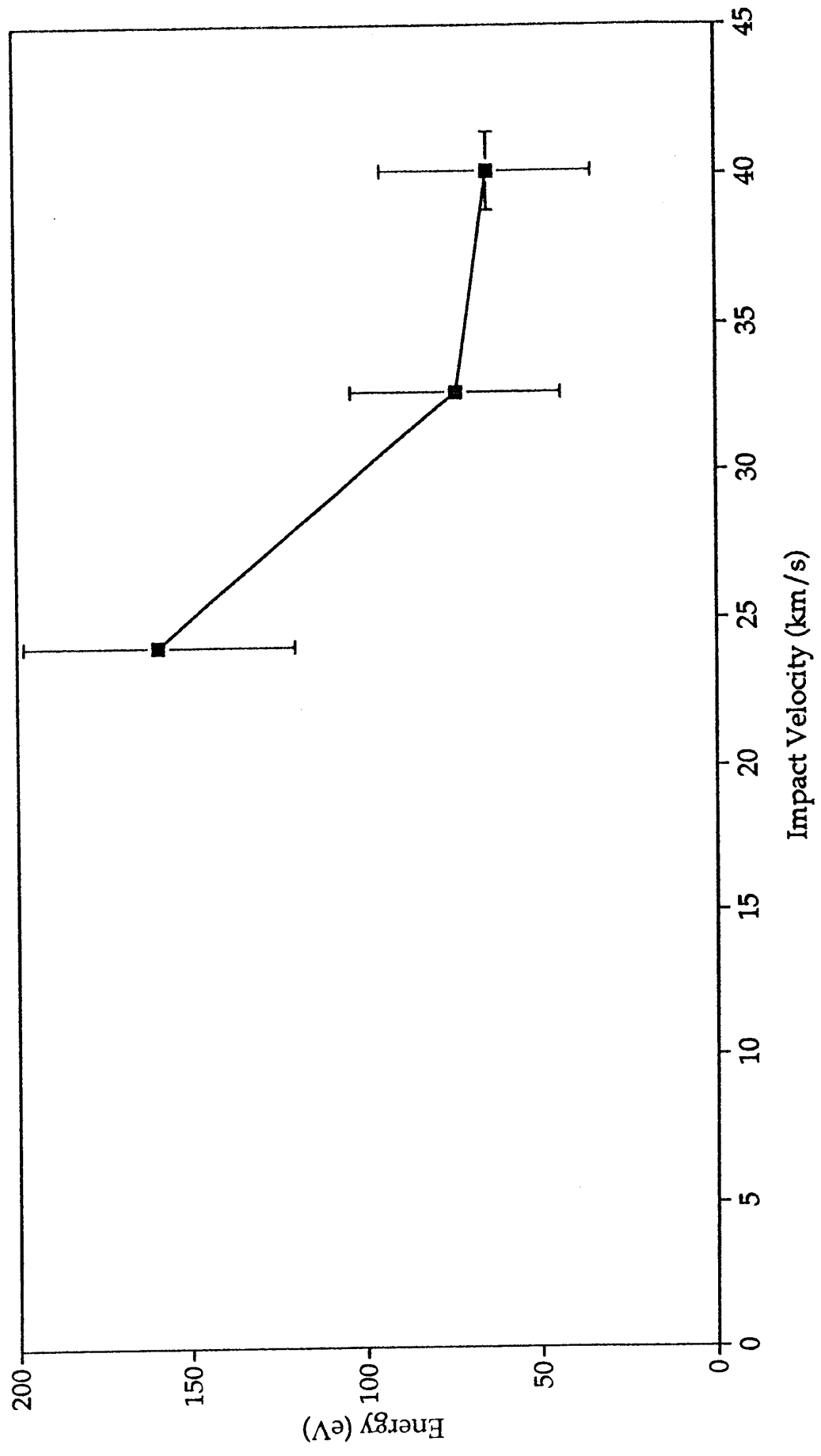
Figure 3.15h Molybdenum Ion Energies
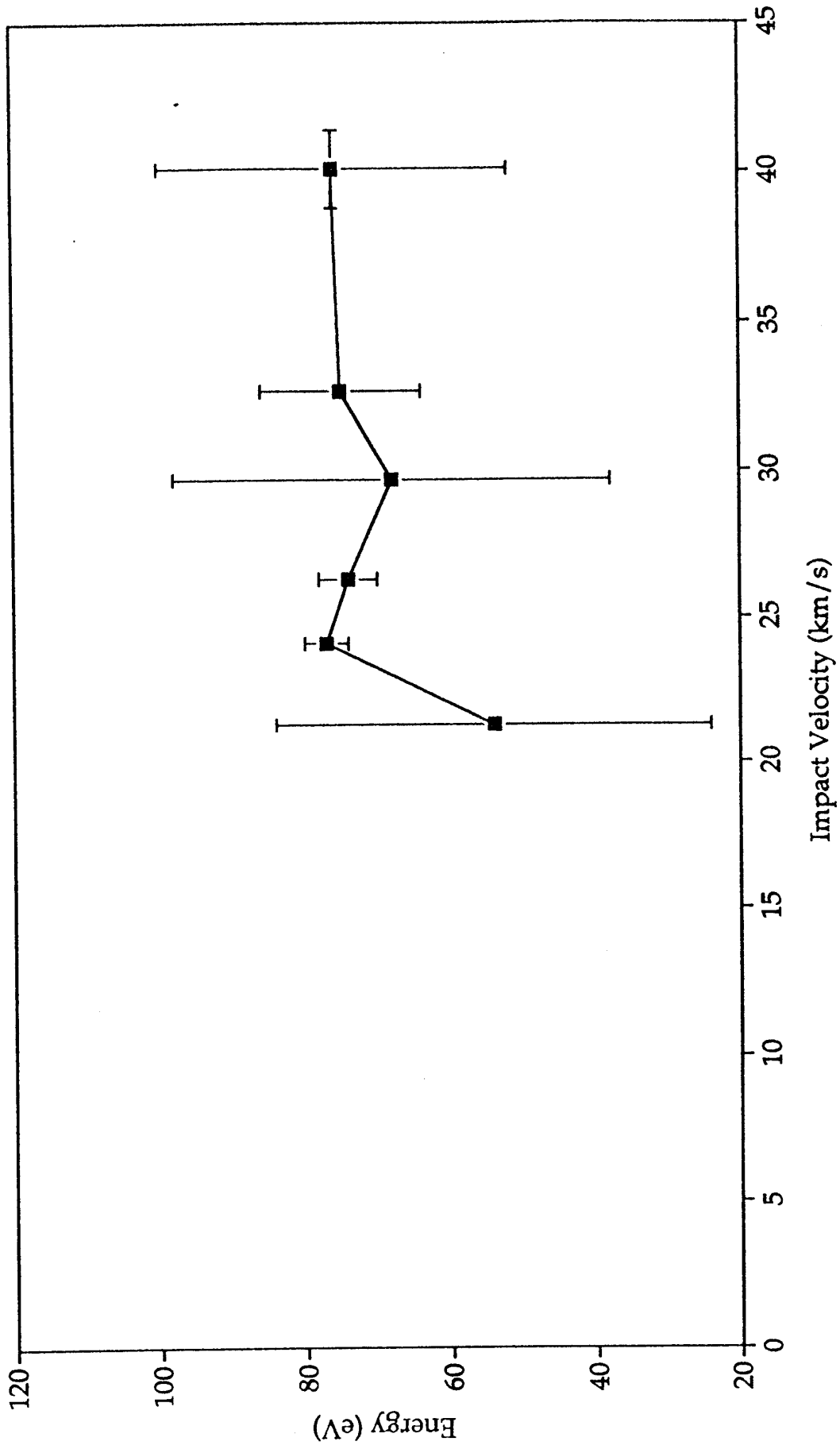
Ion Species	Threshold Velocity (kms^{-1})
Hydrogen	17.1-18.3
Carbon	22.1-26.0
Sodium	1.63
"Mass 27"	8.8-?
Potassium	2.6
Calcium	2.6-?
Iron	19.8-?
Molybdenum	18.9-24.7

Table 3.1. Ionisation threshold velocities observed for iron impacts on molybdenum.

expediency rather than strict validity, and we need not rule out the principle of collisional redistribution of energy in the plasma.

Collisional redistribution of energy would be expected to increase in efficiency with increasing impact velocity in line with the increasing vapour and plasma density. We may be seeing some evidence of this with the convergence of the sodium, potassium and calcium energies at velocities above 15 kms^{-1}. The other species appear to have higher energies, with the exception of hydrogen which has approximately zero energy throughout the velocity range. Hydrogen is in many ways a special case as, although it may be present in the form of adsorbed water vapour (oxygen is occasionally seen in mass spectra, but the system only detects positive ions and so oxygen's electronegativity hampers its detection), its presence in metals is through absorption and occupation of inter-lattice spaces. Its release mechanism is thus different to that of chemically bonded species, as is its subsequent behaviour in atomic collisions due to its simple structure.

Ratcliff and Allahdadi (1994) report an energy of 160 eV for hydrogen liberated from a 94 kms^{-1} boron carbide particle impact on aluminium. This would not be expected from extrapolation of the iron-on-molybdenum result over the intervening 50 kms^{-1}. This may indicate the onset of a different regime of hydrogen energising at some intermediate velocity. Data from some of the other tests (awaiting analysis) using other target materials extend to velocities of 70 kms^{-1}, and may provide an answer to this.

3.4.2.1.2 Plasma Energy

Having derived the characteristic energies of the ions observed in the mass spectrum, the total kinetic energy of the plasma can be derived from the number of ions produced. For the later measurements in this study, the ion yield was a measured parameter, derived from the integrated negative ion signal on the target plate. In some of the earlier studies this was not measured, and so to make use of these data the yield was derived using an empirical ion yield equation derived from other data sets. This equation is

$$Q = 8.7 \times 10^{-11} mv^{3.27}$$

for the iron impacts on molybdenum.

Figure 3.16 shows the total energy of the impact plasma (kinetic energy of the ions plus the energy if ionisation) as a function of the impact velocity for each of the species which are observed in enough events to provide good statistics. The fraction of the impacting particle kinetic energy in the impact plasma increases with velocity, as would be expected, reaching a maximum of 0.35% at 42 kms^{-1}. These results are in line with expectation, as Ratcliff and Allahdadi (1994) report 3-4% for a boron carbide particle impacting on aluminium at 94 kms^{-1}. Also evident in Figure 3.16 is the increasing contribution of iron and molybedenum (and particularly of carbon and hydrogen) and the decreasing contribution of sodium and potassium, with increasing velocity.

Figure 3.17 shows the plasma kinetic and ionisation energies summed over the contributing species. The kinetic energy exceeds the ionisation energy throughout the velocity range, though the ratio decreases from 12 at 2 kms^{-1} to 1.4 at 40 kms^{-1}. The major factor influencing this change is the large yield of hydrogen ions at high velocities, which have a large ionisation energy (13.598 eV), but low kinetic energy.

In principle, the experimental data used in this study can provide information not only on the impact plasma (which is detected), but also on the evolved neutral vapour (which is not). If the plasma temperature is known, the Saha equation can be used to derive the degree of ionisation in the vapour, allowing the quantity of vaporised material to be determined from the ion yield. The energy required to vaporise this material can then be derived if the vaporisation energy is known. Unfortunately, contaminants are the dominant energy carriers except at extremely high velocities (above 50 kms^{-1}), and so the vaporisation energies generally can not be characterised. Also, the plasma temperature is not easily determined, though a crude estimate can be obtained by assuming that the plasma thermal energy is equal to the kinetic energy. This approach has been adopted by Ratcliff and Allahdadi (1994) in considering the 94 kms^{-1} impact. The typical energies derived for the plasma in the present study (~60 eV) corresponds to a temperature of ~5x10^5 K, approxiamtely 50 times the temperatures derived in the hydrocode studies described in Section 3.4.1.2.3. This is not surprising since by looking specifically at the ionised vapour in the experiments we are measuring the high temperature component of the vapour energy distribution, while the hydrocode calculates the average value of the finite cell size, thus suppressing peak values.

3.4.2.2 Measurement of Light Flash Energies

The derivation of light flash intensities is described under Workpackage P4 of this report, the energy of the flash being derived as:

$$E = 0.27 mv^{3.95}$$

where v is measured in kms^{-1}.

Figure 3.16. Plasma Species Energies

Figure 3.17. Plasma Energy
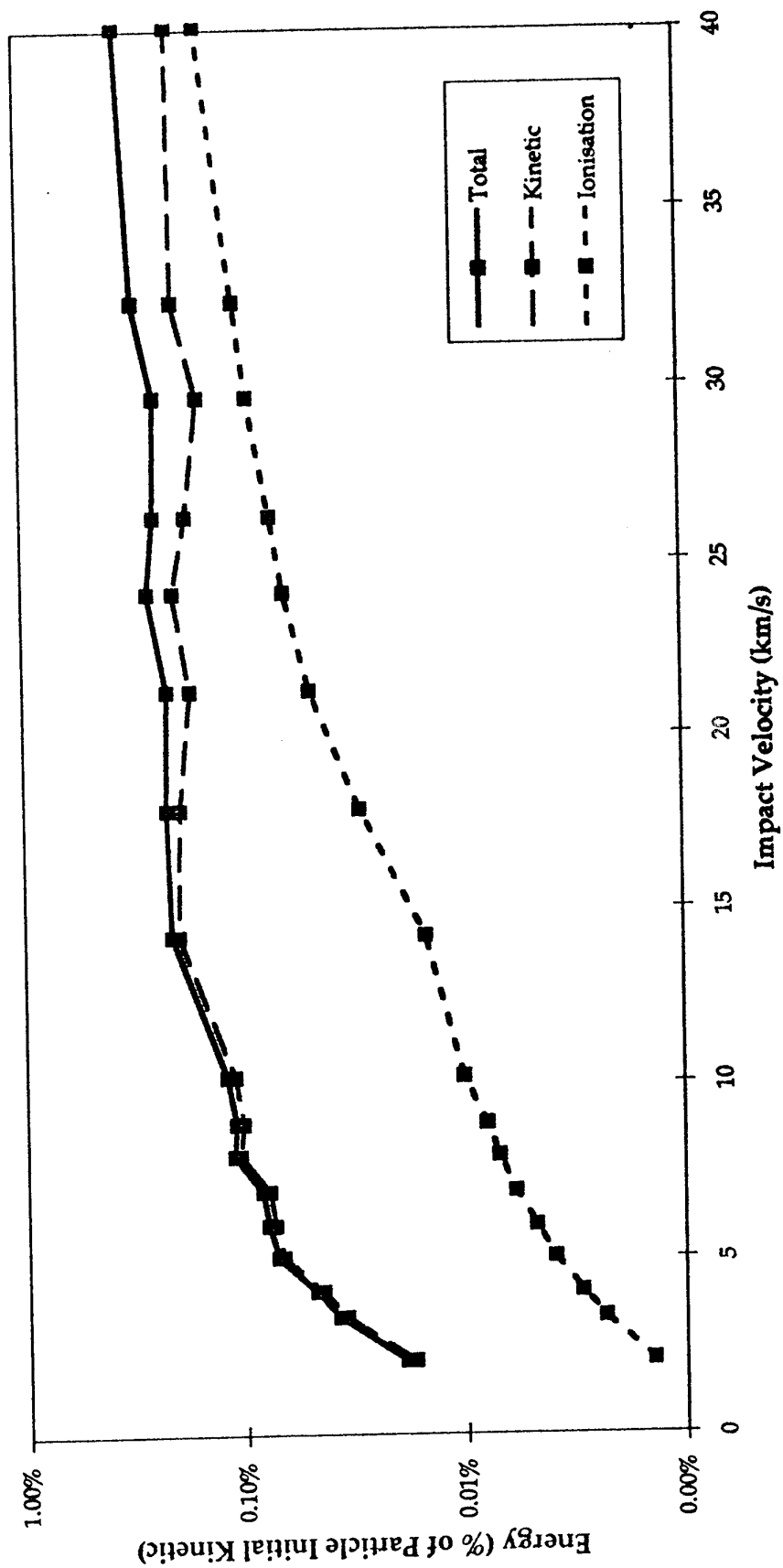
The energy in the light flash is thus about 10% of that in the impact plasma, and rises from ~10^{-3}% at 5 kms^{-1} to ~0.1% at 40 kms^{-1}.

3.4.2.3 Momentum Enhancement

Extensive measurements of momentum enhancement were performed on the UKC 2MV Van de Graaff accelerator by Rembor (1993) in the course of recalibration of the Giotto DIDSY PZT sensors for the encounter with comet p/Grigg-Skjellerup. Further measurements were not made during the pilot experiments performed in this study, though the ability to do so exists. Rembor's results (quoted in Section 3.4.1.2.6 above) are based on analysis of over 350 individual impact events, and thus constitutes a comprehensive analysis. He found that for normal incidence impacts of iron particles on aluminium, the momentum enhancement factor, ε, is given by:

$$\varepsilon = 1 + 0.3(v-2)$$

where v is measured in kms^{-1}.

3.4.2.4 Ejecta Kinetic Energies

The kinetic energy of ejecta particles is not directly measured by the current experiment configuration. However, detailed analysis of the impact plasma recorded on the target (see Workpackage P4, Figure 4.4b) reveals two components to the signal: a fast-rising component due to plasma produced by the primary impact, and a slow-rising component produced by the impact of ejecta particles on the accelerating grid. This grid is ~70% transparent, and so we are seeing plasma from approximately 30% of the ejecta particles. The rest pass unhindered into the body of the experiment chamber, where they will eventually impact on another surface at a time beyond the range of measurements.

As mentioned above, the yield of plasma from an impact is given by

$$Q = 8.7 \times 10^{-11} m v^{3.27}$$

so the yield of secondary plasma is dependant on the mass and velocity of the ejecta particles. Since the momentum enhancement study of Rembor (1993) gives a separate functional dependence on ejecta mass and velocity, we can solve these equations for both parameters, and hence calculate the ejecta energy. The results derived by this method will be 'characteristic' values representing a weighted average.

Figure 3.18 shows the average velocities derived by this method as a function of the impact velocity. The error bars are not shown, but are of the order ±2 kms^{-1}. The results thus show an increase with impact velocity, and are consistent with results obtained in other studies (e.g. Eichorn 1978).

Having derived the characteristic ejecta masses and velocities, the ejecta energy is readily determined. Figure 3.19 shows the ejecta kinetic energies, expressed as a

Figure 3.18. Characteristic Ejecta Velocities
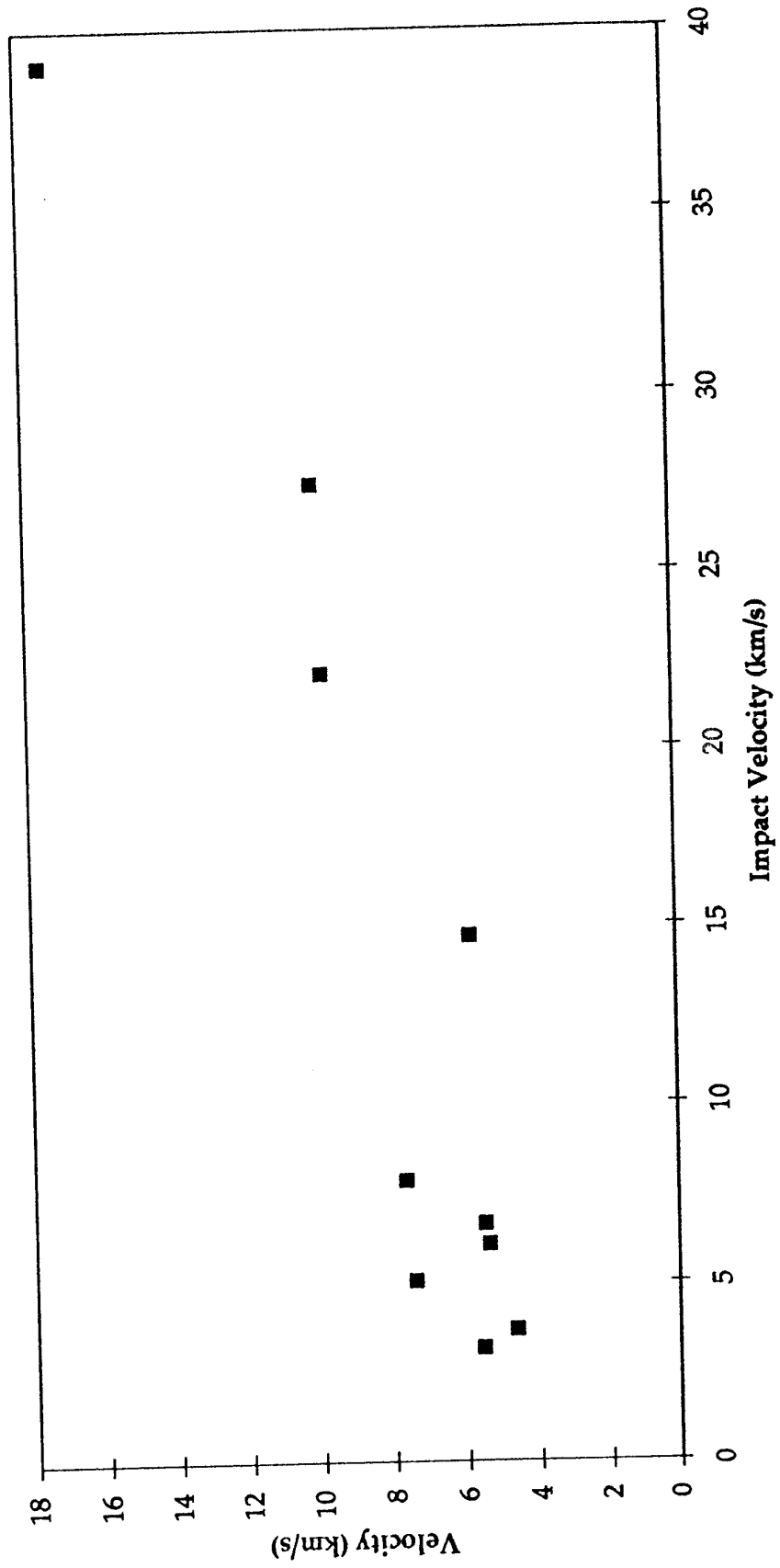
Figure 3.19. Ejecta Kinetic Energy
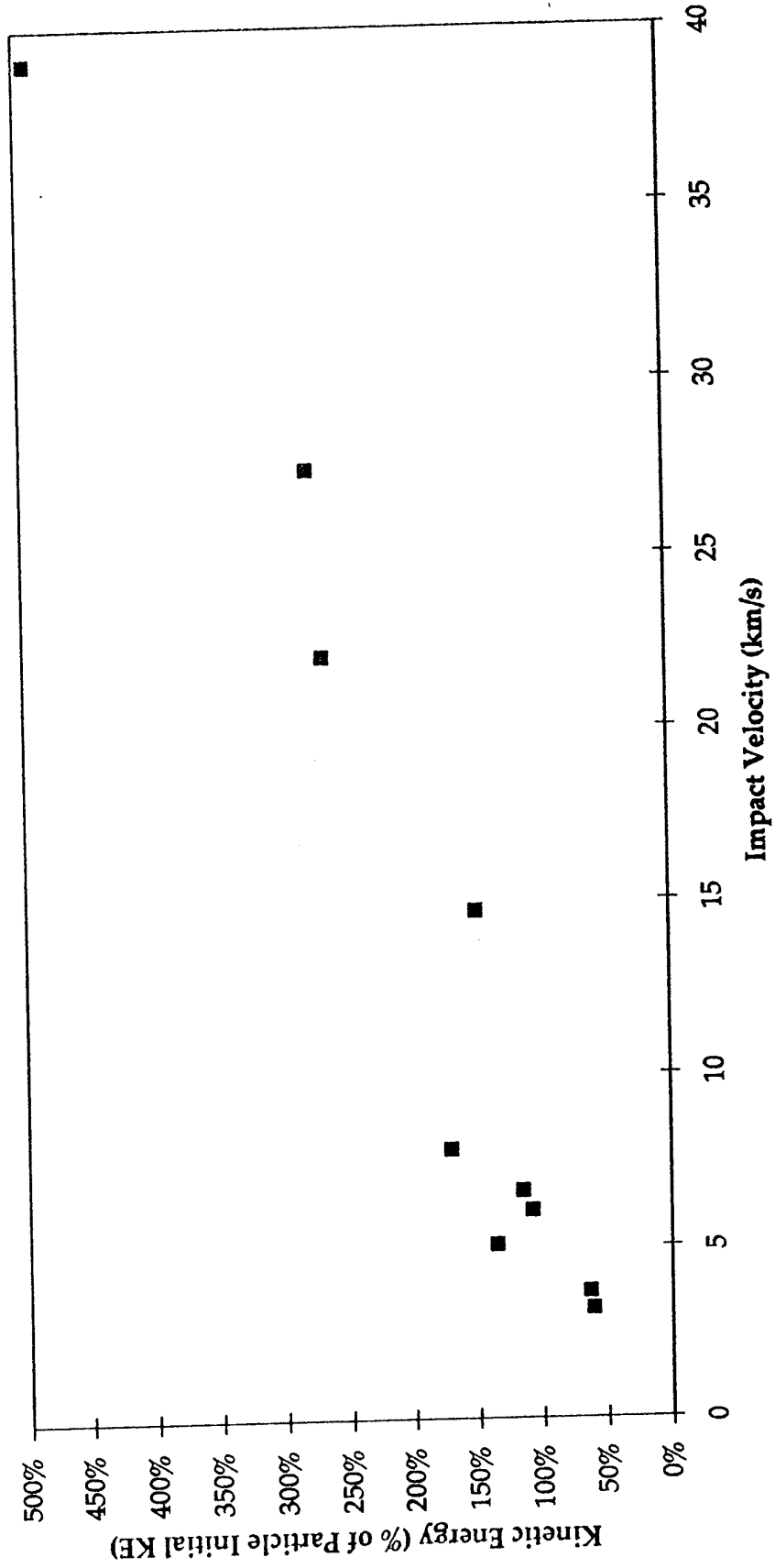
percentage of the incident particle kinetic energy, as a function of impact velocity. The results show a plausible trend, but the values are clearly erroneous as the calculated ejecta energies generally exceed those of the incident particle. The reason for this is believed to be that the plasma measurements (iron impacts on molybdenum) and the momentum measurements (iron impacts on aluminium) are not compatible. However, this technique of deriving ejecta energies is valid, PZT measurements can be incorporated simultaneously with the existing light flash and impact plasma measurements described under Workpackage P4, and so future studies are expected to produce valid results.

3.4.2.5 Summary

Figure 3.20 summarises the energy partitioning information derived from the present study. Unfortunately, due to the anomalous ejecta kinetic energy results, only the light flash and plasma measurements can be included.

3.4.3 Conclusions and Further Study

The work carried out so far has provided information on various aspects of energy partitioning including internal energy (hydrocode), ejecta kinetic energy (hydrocode), plasma production (experimentation) and light emission (experimentation). In addition, a method of determining ejecta energies by experimentation has been developed. Related subjects such as material temperatures and phase change and momentum enhancement has also been investigated.

A number of areas for future study have been identified. True cross-calibration of hydrocodes should be performed using as near identical simulation geometries and material models as possible, in particular to verify that CTH and AUTODYN provide similar predictions of the relationship of crater depth:diameter ratios with impact velocity for similar simulation geometries and materials. Further AUTODYN runs interpolating between and extending the velocities investigated in this study should be performed in particular to refine the derivation of vaporisation threshold velocities, and other materials should be investigated.

The pilot experimental investigations described under Workpackage P4, and the analysis of the resulting data above, show that simultaneous measurement of impact plasma, light flash, and PZT microphonic measurements allows characterisation of most of the important aspects of the impact process. Further data can be derived through spectroscopic measurement of the light flash (to give temperatures directly) and from measurement of crater dimensions. The 2MV Van de Graaff dust accelerator facility at the University of Kent is an ideal facility on which to perform such measurements due to the large range of impact velocities provided. As with the hydrocode investigations, experimentation is required with a variety of impactor and target materials, while the statistical nature of the accelerator performance and of random factors involved in the impact process (possible material inhomogeneity, variable surface contamination etc.) necessitates the acquisition of large data sets and averaging of results.

Figure 3.20: Experimental Measurement of Energy Partitioning
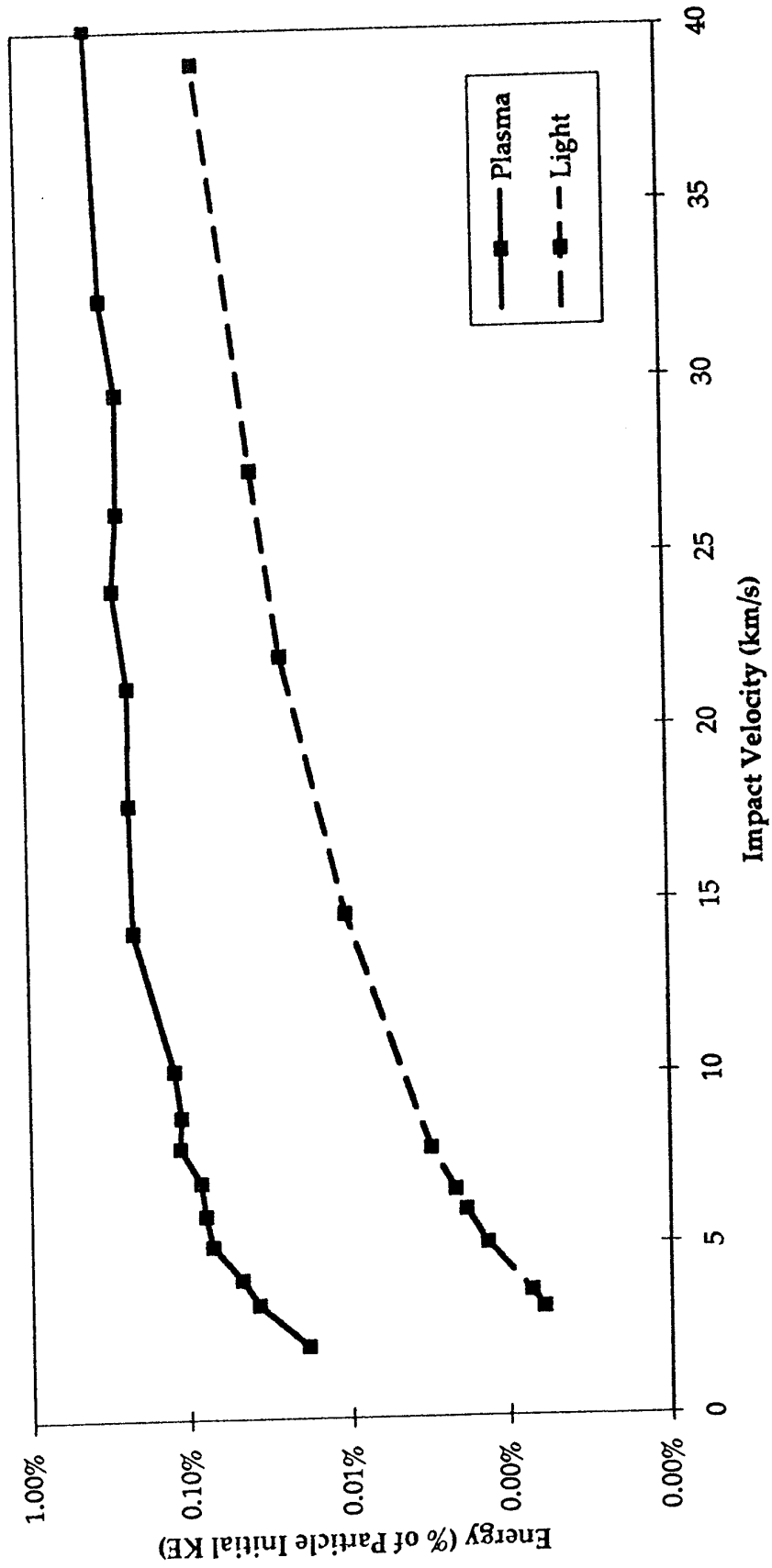
3.5 Generic Impact Damage Prediction Software

For analysis of spacecraft hazard, the most important parameter is the relationship between the impacting particle energy and the ejecta kinetic energy. There is a clear need for a relatively simple predictive software package to establish:

a) penetration vs non-penetration of the impacted surface;
b) ejecta kinetic energy in forward and rearward direction.

This software should not be over-complex in terms of input parameters - the particle should be characterised by no more than mass, velocity and density, the target by thickness, density and 'ductile or fragile'. A standard penetration formula would predict whether the event penetrates or not, and a generic energy partitioning function would give the ejecta kinetic energy (and directionality in the event of penetration). It is suggested that the McDonnell-Sullivan penetration equation (McDonnell and Sullivan, 1992) would be appropriate for determining whether the impact event causes penetration. Kinetic energy partitioning and directionality equations need derivation from hydrocode and experimental study.

4. Design of an Impact Diagnostic Chamber to Study Energy Partitioning in a Time and Spatially Resolved Manner - Dr. M.J. Burchell

4.1 Introduction

The aim of this part of the work is to design a chamber to permit simultaneous study of two aspects of hypervelocity impacts, namely the impact generated flash and plasma production. These phenomena are held to be sensitive to both projectile and target in an impact, and reflect underlying physical properties of the system. It is assumed that the projectiles are micron sized particles travelling at speeds in excess of 1 kms^{-1}. The design chosen is given complete with details of necessary peripheral equipment and apparatus. Such a chamber has been constructed, and results from typical experimental runs are shown. The chamber is designed as a stand alone unit which is both light- and vacuum tight. It is connected, via a beam line, to the exit of a 2 MV Van de Graaff machine, which is used to accelerate (charged) dust particles to hypervelocities. The accelerator (see Burchell et al, 1993 for a recent description) is one of only two such machines presently operational world wide.

4.2 Background

Both impact flash and plasmas have been studied previously. For micron sized projectiles the light flash work of G.Eichorn (1976,1977,1978a and 1978b) is usually taken as the standard reference. He found the flash had several components, a fast first flash (time scale of 100 nanosec) and a longer second flash (duration of up to 100 microsec). These two could merge (depending on projectile and target composition). The integrated flash energy is dependent on projectile/target composition and projectile mass and velocity. The peak flash intensity for a given projectile is also a function of how refractory the (metal) target is. He also probed the temperature of the flash using analysis of the wavelengths observed in his experiments.

Impact plasmas have also been studied for many years. Several instruments have been flown in space which make use of the plasma. Work such as that by B.Dalmann 1977 has shown that there is a velocity dependence of plasma production of various ion species (note: caution is needed when reading this paper, although a primary reference it is widely considered to contain errors of interpretation). Other authors (e.g. Ratcliff and Allahdadi, 1994) have shown that the plasma contains the signature of both target and projectile composition. A known (pure) target can thus be used to determine the projectile composition.

Further, studies of such phenomena, combined with computational simulation, will be a tool in achieving the goals of other parts of this contract, e.g. Objective 2: scaling laws and Objective 3: Energy partitioning. These objectives have considerable overlap, e.g. it is very important for development of improved scaling laws to achieve advances in knowledge of energy partitioning at very high velocities. The combination of facilities and skills at the University of Kent makes it the only centre able to simultaneously achieve all these goals.

4.3 Design Details

The features of light flash and plasma production reported by others were used to initiate the design of a chamber to observe both. This was combined with experimentation in the lab, testing various features of the design.

4.3.1 The Chamber

The chamber itself is a stainless steel pot, with a lid which rests on a flange at the top of the pot. The internal pot diameter is 30.4 cm, and its internal height is 49.0 cm. The walls are 0.3 cm thick, with the lid being 2.5 cm thick. The lid seals the pot under its own weight (compressing a rubber O ring resting in a channel cut in the lip of the pot created by the flange). This seal is both light and vacuum tight.

To permit viewing of the interior of the pot several holes were cut in the walls and lid of the pot. These had flanges attached so that similar fitted external devices could be connected in a light/vacuum tight fashion. A variety of stainless steel tubes were used as attachments. These were custom made to contain photo- or electron-multiplier tubes. Windows mounted in stainless steel flanges were also provided. The photomultiplier tubes were mounted such that they viewed the interior through these windows. The electron multiplier tubes were mounted with no obstruction between the tube and interior. The windows were of two standard sizes matching the viewing ports (6.0 and 10.0 cm dia.). To permit observation of different spectral ranges, some windows were of glass (transmission over typically 380 to 2100 nm), and some were of fused silica (extending transmission from 185 to 2700 nm).

The viewports in the pot walls are at two different heights. There is a ring of ports spaced at 90° around the pot at its half height, any of which can be used to connect the beam line. One of these ports has a 10 cm internal diameter, the others are 6 cm. A second ring of view ports is mounted 40 cm above the base of the pot. There are 10 equally spaced ports in this ring (36° apart). All are of 3.5 cm internal diameter. Again, one can be used to connect to the beam line, and the others for observations. Note that these arrangements always leave one viewport directly opposite the beam line. This can be fitted with a fluorescent screen. In the absence of any target in the pot the beam can impact this screen, providing a mechanism for aligning the beam with the pot.

The pot lid also has view ports. To best accommodate a variety of viewing arrangements, two lids were manufactured. One has four viewports, each 4 cm internal diameter. These are arranged a quarter of the way in from the pot edge along a pair of mutually perpendicular diameters. The second lid has a centrally mounted viewport of internal diameter 6.0 cm.

For safety reasons the lids are lifted on and off the pot by a winch. They are guided into position by studs in the upper lip of the pot with matching holes in the lid. A hinged lid arrangement was considered, but due to the great weight of the lid was discarded on safety grounds. The use of the winch also permits easy interchange of the two lids.

The pot is positioned on a stable metal table. Two such tables are used, to allow for connecting the beam line at different heights on the pot. Shelves are also attachable to the tables, to provide support at various positions for the external tubes containing the electron and photo-multipliers.

Not all the ports are used for observations during running. The rest are sealed with solid metal flanges. Some of these are equipped with electrical feedthroughs to permit power and electrical signals to be passed in and out of the pot.

All internal surfaces of the pot are lined with flexible black plastic to prevent reflections of light reaching the viewing ports. Vacuum black paint could be used instead. The attraction of the plastic is that it is easily rearranged to partition the interior and customize viewing conditions for each experimental run (i.e. which view ports to cover/uncover, helping define viewing geometries etc).

4.3.2 Interior Fittings

The target is mounted in the pot, as are any lenses, collimating devices, etc used to assist viewing of the target. Given the relative depth and height of the chamber, plus the fact that access is from the top, it was decided that the best arrangement is to suspend all interior fittings from a metal sheet fitted just below the pot lid. The sheet rests on four equally spaced lugs welded to the pot walls 2.0 cm below the top. The sheet is made of aluminium, 1.0 cm thick. It is a disk of 28.0 cm diameter, nearly filling the interior diameter. Holes are cut into the sheet such that the viewports in the lid can have an unrestricted view downward into the pot. A variety of rods were machined which can screw into the sheet at various positions and then hang vertically. These can be moved along diameters, and by rotation of the sheet, almost all of the interior can be reached by lenses or targets supported by these rods. The supports are (horizontal) metal bars which can ride up and down the rods. They are secured by screws which press against the rods. This arrangement permits the whole depth of the pot to be used. All the fittings are non-conducting and non-magnetic.

With such an arrangement the target and any lenses required can be set up on a bench external to the pot. They can then be lifted into position. This removes the need for trying to position apparatus directly into the confined volume of the pot.

4.4 Vacuum and Light Tight Seals

Earlier work on light flash has shown that a vacuum of at least a few times 10^{-4} mbar is needed to prevent generation of light by expansion of an impact generated ejecta cloud or shock wave into the surrounding atmosphere (Eichorn 1976, 1978a). The interior of the pot must thus be maintained at a lower pressure than this. Since the beam lines from the accelerator are maintained at 1 or 2×10^{-6} mbar the interior of the pot is also maintained at this vacuum. No special pumping system is used; the diffusion pump maintaining the vacuum in the beamline suffices. This level of vacuum is also more than sufficient to permit plasma studies.

Due to the many ports in the chamber, care has to be taken to ensure that no vacuum leaks occur. Rubber seals are sufficient where they can carefully be placed in position before making a connection. Where there is insufficient room for careful positioning, or where a long term seal is required, metal O-rings are used with knife edge seals. Few problems with seals have been encountered. Most such problems were solved by retightening the last altered joint. A helium leak testing system is ideal for tracking down any harder to find leaks.

In general there is no problem pumping down the system to the required level provided clean materials are used inside the pot. Any large surfaces are washed before insertion in the pot. No pourous surfaces (water rich) are used at all. No heating of the pot is necessary to permit pumping to the desired vacuum (achievable in 20 to 30 minutes after sealing the pot).

Although a vacuum of 1×10^{-6} mbar can easily be achieved, such a system was found not automatically to be light tight. This was not due to windows being used. Rather the vacuum seals themselves had light leaks. Also the electrical feedthroughs had light leaks. Care therefore needs to be taken to wrap all joints with light tight black tape, or to connect plugs onto the electrical feedthroughs.

As a test of light tightness, an arbitrary limit of less than 1 background pulse per second was required on the photomultiplier tubes in normal operation. This was easily achieved under the above conditions. In operating conditions, with the trigger on the photomultiplier set to be sensitive to light flashes from the target, one false trigger every few minutes was achievable.

4.5   Photomultiplier Tubes.

4.5.1   Type

Two main types of tube were used, an EMI 6097, and an EMI 9789Q. Both have high gain. The latter tube is equipped with a fused silica window so that it is sensitive to uv wavelengths. Both tubes are operated at 1.4 kV. The power supplies are standard laboratory equipment. Readout is in the integrating mode, i.e. there is a small time constant for accumulating the signal on the base of the tube, and a large time constant seen by the external circuitry. The signals out are viewed on LeCroy digital storage scopes operating at 100 Msamples/sec (100Ms s^{-1}). A typical bin width in the sampled data is 10 ns.

4.5.2   Cooling

The 9789Q tube is cooled so that it operates in a low noise regime. The cooling system is a 50/50 mix of ethylene glycol and distilled water (with an added antibacteriological agent to prevent growth of biological contaminants). This is liquid down to -35°C. The liquid is kept in an insulated bath complete with lid. Refrigeration coils from an industrial refrigerator are suspended in the bath. The temperature is monitored by a thermocouple which regulates the power supply of the refrigerator. A constant temperature can thus be maintained in the liquid. A pump is mounted in

the lid of the bath and the liquid is circulated round a closed loop from the bath to the photomultiplier. The mounting of this has a coil through which the liquid circulates. All pipes from bath to photomultiplier tube are insulated. Dry silica is used to prevent condensation forming on the electronics at the base of the photomultiplier tube. The front window of the tube has dry air blown across it to prevent condensation forming.

4.5.3 Calibration

The photomultiplier tubes were calibrated, both on a relative and absolute scale. This is essential when using several tubes simultaneously (relative calibration) and also when using the results to better understand the physics of hypervelocity impacts (absolute calibration).
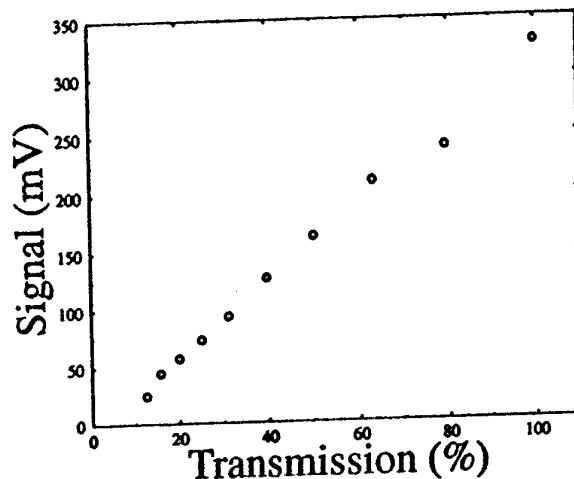
Figure 4.1. Response of pm EMI 6097 to an attenuated light signal.

The method was to have the tubes view a known light source. To this end a light tight box was constructed. It is a hollow cylinder of aluminum. The internal dimensions are: length 70.0 cm, diameter 30.0 cm. Both ends are removable. All interior surfaces were painted black. One end is solid except for an electrical feedthrough with 9 connections. The other end has a circular opening in its centre, 2cm in diameter. The ends are secured to the cylinder by screws, and all joints are sealed with black tape. A tube (length 10.0 cm, diameter 5.0 cm) is placed at the opening in one end, and contains slots into which neutral density filters can be placed. The photomultipler tube being studied is then placed against the end of this tube (and sealed in place with black tape). The result is that it has a collimated view of the interior of the cylinder along the main axis of symmetry.

In the interior of the cylinder is placed a calibrated tungsten lamp with a current stabilized power supply. The calibration is supplied by the manufacturer who claims it is accurate to 20% at a known temperature of operation of the filament. To

reduce the area of illumination the lamp is behind a lid which is viewed through a pinhole. An arrangement of three more pinholes is positioned near the end face of the cylinder with the viewing hole. Two of these pinholes are stationary, the third (which is between the other two) is on a disk which rotates at 36 Hz (the disk is attached to the spindle of a 6V motor). This rotation causes a pulse of light to be seen at the photomultiplier tube. The duration of the pulse is determined by the size of the pinholes and the distance of the rotating pinhole from the centre of the rotating disk (for a constant frequency of revolution). Pulse durations of 250 to 320 microseconds are typical.

The amount of light seen by the photomultiplier tube during a pulse is controllable by use of neutral density filters. The photomultiplier tube is read out as per normal onto a digital storage scope. Although the integrating readout has a long readout time constant (it was of approximately 247 microseconds), it is still comparable to the typical pulse durations. Therefore the signals seen on the scope had to be corrected for decay of the signal during the pulse length. This was done on a personal computer (section 4.7). The photomultipier tubes can then be calibrated to check for linearity of response. The linearity curve for the EMI 6097 tube is shown in Figure 4.1. The absolute calibration is found using the lamp manufacter's calibration, combined with geometric efficiencies, transmission efficiency of the filters and the response function of the photomultiplier tube combined with the emission spectrum of the lamp.

As a check on the absolute calibration the photomultiplier tube was replaced by an optometer (model 370, UDT Instruments, 12151 Research Parkway, Orlando, Florida, 32826, USA). This integrates the received light signal. Allowing for the number of pulses per integrating cycle and the response function with wavelength, the amount of light incident on the photomultiplier tubes could be found directly. The agreement with the other method was good to 40%. (It is the absolute calibration provided by this method that is used for example in Figure 4.3.)

4.6   Electron Multiplier Tube

The plasma is detected by the presence of signal ions incident on the surface of an electron multiplier tube (type EMI 9643/3B). For these measurements the target is connected to a 1 kV dc supply. An earthed grid is placed 0.7 cm above the target. This accelerates ions out of the plasma in a direction perpendicular to the target surface. The ions then drift in a region of zero electric field to the wall of the pot. The target is so aligned that the viewport is along a line perpendicular to its surface, centred on the optimum beam impact point. The electron multiplier tube is mounted in a stainless steel tube connected to this port. No window or obstruction prevents the ions reaching the electron multiplier which is operated at -3kV (relative to an earthed grid at its entrance).

The signal on the electron multiplier is read out on a LeCroy digital storage scope with 100 Ms s^{-1} sampling. 10 ns sampling intervals are standard. This scope is in turn connected to the data processing system of section 4.7.

4.7 Data Processing System

· The digital oscilloscopes used in this work were LeCroy models 9304 (a quad scope) and 9450 (a dual scope). Both are equipped with GPIB interface ports, and can thus be connected to an external device. We use a personal computer (486DX, 33MHz, 342Mb hard disk, GPIB interface). This pc runs the National Instruments LabView data acquisition system. This is a proprietary system, but permits users to develop their own system specific applications. We have developed several programs, each of which is run from a window on the pc. We transfer data from the scope to the pc, display it on the screen and can expand any region of interest for close study. The events are also saved on the pc's hard disk, and can be copied to floppy disk or any backup system.

Other applications can also be developed which read in the data from disk and process it with a variey of statistical tools.

The importance of such a system of storing and analysing data cannot be stressed enough.
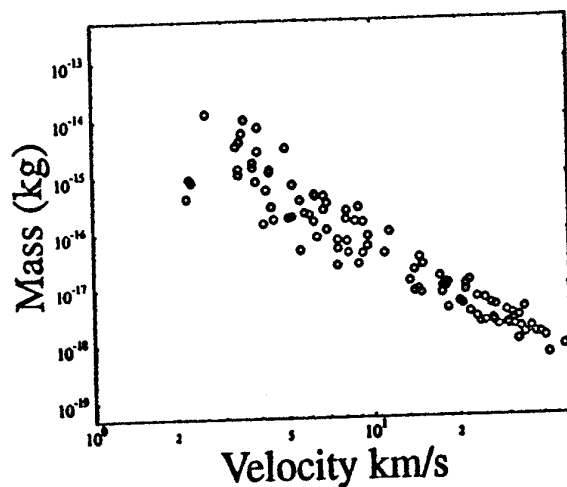
Figure 4.2. Mass vs velocity for iron particles used as projectiles in a typical data run

4.8 Experimental Runs

The system designed was tested in various experiments. The projectiles were micron sized iron particles. They are accelerated in the 2 MV Van de Graaff accelerator. This is one of only two such machines worldwide which are used for microparticle acceleration. In everyday operation particles are routinely observed up to 50km s^{-1}. Projectile mass and velocity (which is measured separately for each projectile) are shown for a typical run in Figure 4.2 (a one and a half day experimental run). In this report only iron particles are accelerated, but any particles which can hold a surface charge can be used. If we assume the particles are spherical, the data shown in Figure 4.2 corresponds to particles of diameter 0.05 to 1.2 microns. It can be seen that over a relatively short period of time data can be obtained for impacts of small

particles covering the range of velocities found in Earth orbit. This ability is a major asset of the research at the University of Kent, and the accelerator is extensively used for studies of hypervelocity impact processes and callibration of detectors for space use.

4.8.1   Light Flash Only

A variety of runs have taken place testing the setup described above. Targets of aluminium and molybdenum have been used. The targets have been viewed by photomultiplier tubes with different geometries. One tube has viewed the target through a lens positioned 5.0 cm (its focal length) away from the target. A second lens just above the photomultiplier surface then matches the beam of incident parallel light to the surface area of the tube. This was to improve light collection efficiency. Equally the target could be viewed directly by a photomultiplier tube at the wall or lid of the pot with no intermediate lens. Both systems (despite their different geometric acceptances) produced usable results.

Other runs were carried out viewing the target from different angles relative to the surface and incident projectile directions. In Figure 4.3 are shown the results of runs where the projectile is incident on the target at 36° from the normal, with the photmultiplier main axis parallel to the target surface. What is plotted is the total light flash energy (normalized to projectile mass) vs. projectile velocity. The solid curve found is the simplest parametrization describing the data; energy/mass = 0.27 * velocity$^{3.95}$ (J kg^{-1} and km s^{-1}). Such relationships were already known from the work of Eichorn 1976. The data clearly shows that the system operates well over a wide range of velocities.

Figure 4.3. Total light flash energy (normalized to projectile mass) vs projectile velocity for iron impacting molybdenum

Tests have been made changing the trigger conditions for data collection. Triggering on the light flash is found to be an efficient way of collecting data. We also record the velocity and charge of the incident projectile using pickups in the beam line just in front of 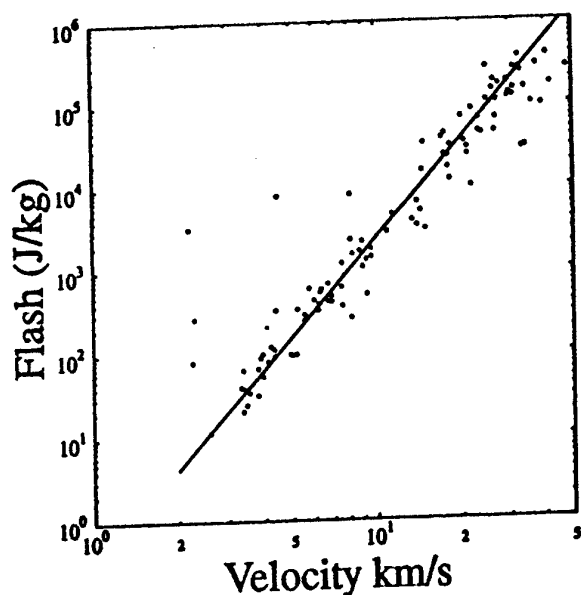the pot. Under good operating conditions 15 to 20 hypervelocity events an hour can be found, studied on the scope and transferred to the pc. In approx 200 such events only 1 was subsequently identified as a noise light signal falsely coincident with a particle entering the pot.

4.8.2 Plasma Studies

The results of operating the electron multiplier are independent of the use of photomultiplier tubes. Sufficient viewports are included that both can operate at the same time. For a typical event (iron impacting molybdenum at 21.4 km s^{-1}) the resulting electron multiplier signal is shown in Figure 4.4c. Using the signal from the target itself (which is connected to an amplifier and records both the arrival of the charge projectile and the electrons liberated in the plasma) to provide a t_0, the absolute times of each ion signal in an event are found. Assuming that each signal is from a singly ionized atomic species, the peaks in Figure 4.4c can be identifed using relative drift times to get an atomic mass scale. They are thus found to be C, Fe and Mo (in the example here).

4.8.3 Combined Light Flash and Plasma Studies.

The photo- and electron multiplier tubes can be operated simultaneously. Experimental results for plasma production and the integrated light output are found to be unchanged. Data from a typical event (iron impacting molybdenum at 21.4 km s^{-1}) is shown in Figure 4.4. We show (as displayed on the pc) the various features of the event. The horizontal scale is in units of 1 microsecond, the vertical scales are arbitrary depending on the electronics used (e.g. charge preamplifiers which must be calibrated). In Figure 4.4a are the signals from the pair of pickups in the beam line. From the height of these is obtained the particle charge, and from the relative separation the velocity. From these quantities, combined with the (known) accelerating voltage we obtain the particle mass. In 4.4b we show the signal from the target itself. In 4.4c we show the electron multiplier spectrum; each peak represents the arrival of an ion species (here identified as C, Fe and Mo). In 4.4d is the photomultiplier signal. All data is saved on the pc for later, detailed, analysis. Even if lenses are used inside the chamber to increase light collection efficiency, the spacing of the viewports is such that the electron multiplier tube still collects the same signal as before.

4.9 Spatial Resolution of Light Flash

Two main methods have been investigated to determine spatial resolution in the impact work. The first method is to build a beam position monitor. This device consists of two pairs of parallel plates and a ring at the entance and exit. All of these are conducting. The rings give an induced signal proportional to the total charge passing through them. The pairs of parallel plates follow each other in the beam line
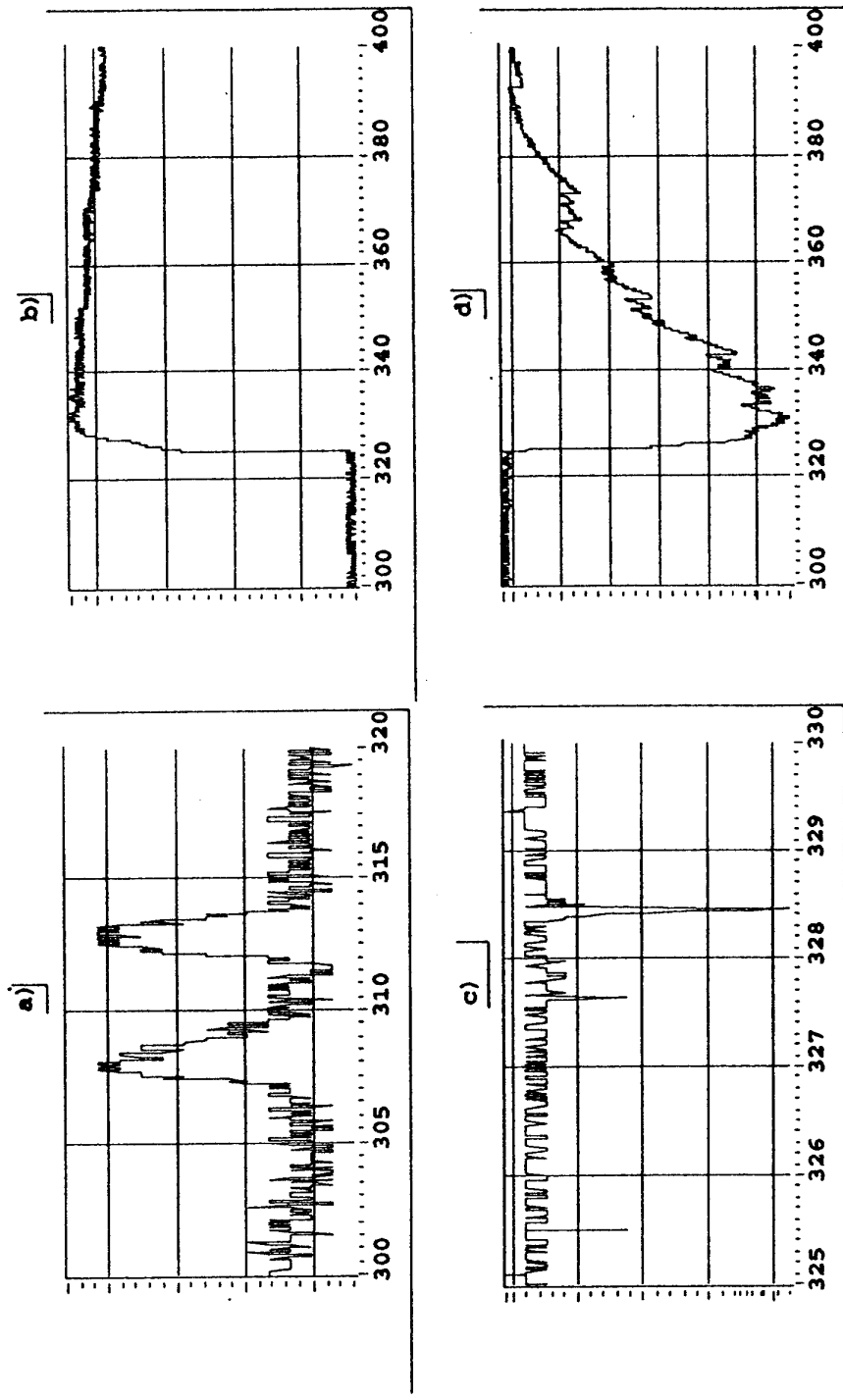
Figure 4.4   Data from iron impacting molydbenum at 21.4 km/s (a) is the signal from pickups in the beam line, (b) is the target signal, (c) is the plasma signal from the electron multiplier (identified from left to right as C, Fe and Mo), and (d) is the light flash (integrated signal on the photo-multiplier tube). Horizontal axes are time in microseconds.

and are rotated at 90° to each other. The signals on each pair of plates are proportional to how close the charged particle is to the plate being read out. Thus, by comparing to the total charge, the signals from the plates give a coordinate in a pair of orthogonal axes. Tests of this method have produced positions good to 1 to 2 mm. Assuming that the beam of particles is not diverging this can be projected to the target to locate the impact site with the same accuracy. Equally two such devices can be used to overcome the problem with beam divergence. If the population of impact sites on the target is less than one every few square mm, the target can be removed and the sites later studied and correlated with the measured flash or plasma production. The distribution of craters observed on the target during subsequent scanning is compared to the predicted distribution from the x-y detector to obtain the relative alignment.

An alternate approach is to use light flash measurement which is position sensitive. By use of pinholes or collimating slits, the photomultiplier tubes can be used such that they see only limited areas of the target. This method is slow and static. An improved method would be to use a segmented photocathode photomultipler tube. These are available from Phillips and Hammamatsu. They contain what are essentially a large number of separate photocathodes in a single tube (Comby and Meunier, 1988). Each is read out separately. The area of each is 1 to 2 square mm. If the target surface is focused directly onto the photmultiplier surface a position resolution of 1 to 2 mm is achieved. If a magnification of x10 is used it would be practical to achieve 100 micron accuracy. Whilst the impact craters from micron sized projectiles are smaller than this, such a system would be invaluable in studies of ejecta.

Such a system would cost approximately \$6,000 for a photomultiplier tube, plus the cost of reading out all 64, 96 or 256 channels (dependent on model). Some schemes exist for reducing the complexity of the readout system, but a separate channel per photocathode channel is the ideal. No changes would be required to the chamber design to incorporate such a system. Provision is already made for lenses inside the chamber, and the photomultiplier tube can be mounted as are the others. Due to the cost and complexity of the readout this scheme has not be tested, but presents no inherent difficulties.

4.10 Conclusions

A design has been prepared for the simultaneous observation of hypervelocity impact generate light flash and plasma generation. The light flash and plasma have been separately and simultaneously observed in a test setup. The timing resolution is good to 10^{-8} s. The wavelength range studied is 180 to 2700 nm. To obtain the maximum benefit of such a system various peripheral devices are needed. These include digital storage oscilloscopes with 100 Ms s^{-1} sampling and interfacing to a pc. A pc with a large capacity hard disk and a pc based data acquisition package (e.g. National Instruments LabView) are recommended. A separate arrangement needs to be provided for calibration of the photomultiplier tubes. The result is a flexible instrument which is easy to use and permits detailed study of these hypervelocity impact related phenomena.

The typical data runs described have already been used to produce results shown in conference (e.g. Burchell et al, 1994). Confirmation of previous observations of light flash and plasma studies have been the first goal of the published work. Present work focuses on the generation of light flash as a function of target material, on the critical velocities at which plasma production commences (compared to theorectical calculations) and the evolution of the energy carried by the plasma with impact velocity. There is considerable overlap here with objectives 2 (scaling laws) and 3 (energy partitioning) of this present report, demonstrating the applications of the chamber in such work.

References

Anderson, C.E., Morris, B.L. and Littlefield, D.L., 1992, A Penetration Mechanics Database, *South West Research Institute Report, 3593/001*, San Antonio.

Birnbaum, N.K., and M.S. Cowler, 1987, "Numerical Simulation of Impact Phenomena in an Interactive Computing Environment", International *Conference on Impact Loading and Dynamic Behaviour of Materials "IMPACT '87"*, Bremen, Germany, May 1987.

Birnbaum, N.K., Cowler, M., Itoh, M., Katayama, M. and Obata, H., 1987, AUTODYN - An Interactive Non-Linear Dynamic Analysis Program for Microcomputers through Supercomputers, *9th International Conference on Structural Mechanics in Reactor Technology, August 1987*, Lausanne.

Burchell, M.J., J.A.M. McDonnell, M.J. Cole and P.R. Ratcliff, 1993, The Hypervelocity Impact Facilities at the University of Kent at Canterbury (UK), *Workshop on Particle Capture, Recovery and Velocity/Trajectory Measurement Technologies*, Houston, TX, September 1993.

Burchell, M.J., Kay, L. and Ratcliff, P.R., 1994, Use of combined light flash and plasma measurements to study hypervelocity impact processes, *Adv. Space Res.* (in submission).

Christiansen, E.L., Cykowski, E. and Ortega, J., 1993, Highly Oblique Impacts into Thick and Thin Targets, *Int. J. Impact Engng.*, Vol. 14, pp.157-168.

Comby, G. and Meunier, R., 1988, Test of a new 64-channel PMT for imaging, *Nuclear Instruments and Methods in Physics Research*, A269, 246.

Cour-Palais, B.G., 1987, Hypervelocity Impacts in Metals, Glass, and Composites, *Int. J. Impact Engng.*, Vol. 5, pp681-692.

Dalmann, B.K., Grün, E. and Kissel, J., 1977, Ion composition of the plasma produced by impacts of fast particles, *Planetary and Space Science*, 25, 135.

Eichorn, G., 1975, Measurement of the light flash produced by high velocity particles, *Planetary and Space Science*, 23, 1519.

Eichorn, G., 1976, Analysis of the hypervelocity impact processes for impact flash measurement, *Planetary and Space Science*, 24, 771.

Eichorn, G., 1978a, Heating and vaporization during hypervelocity particle impact, *Planetary and Space Science*, 26, 463.

Eichorn, G., 1978b, Primary velocity dependence of impact ejecta parameters, *Planetary and Space Science*, 26, pp.469-471.

Fechtig, H., Grün, E. and Kissel, K., 1978, Laboratory Simulation, in *Cosmic Dust*, ed J.A.M. McDonnell, Wiley.

Hayhurst, C.J., Ranson, H.J., Gardner, D.J. and Birnbaum, N.K., 1994, Modelling of Microparticle Hypervelocity Oblique Impacts on Thick Targets. *Paper to be presented at 1994 Hypervelocity Impact Symposium*, Santa Fe, October 1994.

Holland, P.M., Gordon, J.T., Menna, T.L. and Charters, A.C., 1990, Hydrocode Results for the Penetration of Continuous, Segmented and Hybrid Rods Compared with Ballistic Experiments, *Int. J. Impact Engng.*, Vol. 10, pp.241-250.

Hörz, F., Cintala, M., Bernhard, R.P. and See, T.H., 1994a, Penetration Experiments in Aluminium and Teflon Targets of Widely Variable Thickness", *AIP Conference Proceedings 310 "Analysis of Interplanetary Dust"*, NASA/LPI Workshop, Houston, Texas, May 1993.

Hörz, F., Cintala, M., Bernhard, R.P. and See, T.H., 1994b, Dimensionally Scaled Penetration Experiments; Aluminium Targets and Glass Projectiles 50 μm to 3.2 mm in Diameter, *Int. J. of Impact Engng.*, 15, pp.257-280.

Housen, K.R., Schmidt, R.M. and Holsapple, K.A., 1983, Crater Ejecta Scaling Laws: Fundamental Forms based on Dimensional Analysis, *J. Geophys. Res.*, Vol. 88 B3, pp2485-2499.

Johnson, G.R., and Cook, W.H., 1983, A Constitutive Model and Data for Metals Subjected to Large Strains, High Strain Rates and High Temperatures, *Proc. 7th Int. Symp. on Ballistics*, The Hague, The Netherlands.

Kissel, J., personal communication (1994)

Mackay, N.G., Green, S.F., Deshpande, S.P. and Newman, P.J., 1993, Interpretation of Impact Crater Morphology and Residues on LDEF using 3D Space Debris and Micrometeoroid Models, *Proc. First European Conference on Space Debris*, ESA SD-01, pp.159-164.

Mandeville, J.C. and Vedder, J.F., 1971, Microcraters Formed in Glass by Low Density Projectiles, *Earth and Planetary Science Letters*, 11, pp.297-306.

Mandeville, J.C., 1972, Profile and Depth of Microcraters Formed in Glass, *Earth and Planetary Science Letters*, 15, pp.110-112.

Mandeville, J.C., 1993, Micrometeoroids and Debris on LDEF, *LDEF 2nd Post-Retrieval Symposium*, NASA Conference Publication 3194, Part 2, pp.303-307.

McDonnell, J.A.M. and Sullivan, K., 1992, Hypervelocity Impacts on Space Detectors: Decoding the Projectile Parameters, in *Hypervelocity Impacts in Space*, ed. J.A.M. McDonnell, University of Kent at Canterbury, pp39-47.

McDonnell, J.A.M., Gardner, D.J., Newman, P.J., Robertson, N.J. and Hayhurst, C.J., 1993a, Hydrocode Modelling in the Study of Space Debris Impact Crater Morphology, *Proc. 1st European Conference on Space Debris*, Darmstadt, Germany, 5-7 April 1993, (ESA SD-01) pp425-431.

McDonnell, J.A.M., Deshpande, S.P., Niblett, D.H., Neish, M.J. and Newman, P.J., 1993b, The Near Earth Space Impact Environment - An LDEF Overview, *Adv. Space Res.*, 13 (8), pp.87-101.

Niblett, D.H., Mullen, S., Neish, M.J. and McDonnell, J.A.M., 1993, Comparison of Flux Data Deduced from Observed Impacts on LDEF with Predictions from Meteoroid and Debris Models, *Proc. First European Conference on Space Debris*, ESA SD-01, pp.165-170.

Niblett, D.H., Gardner, D.J., Mackay, N.G. and McDonnell, J.A.M., 1994, Application of Hydrocode Modelling to the Study of Hypervelocity Impact Crater Morphology, *Adv. Space Res.*, (in submission).

Ratcliff, P.R. and Allahdadi, F., Characteristics of the Plasma from a 94 kms^{-1} Micro-Particle Impact, *Adv. Space Res.* (in press).

Rembor, K-M., 1993, An Application of the UKC Van de Graaff Accelerator: Momentum Exchange at Particle Impacts - a Calibration Study for the Giotto/DIDSY Momentum Sensors, Diploma Thesis, University of Kent at Canterbury, April 1993.

Robertson, N.J., Hayhurst, C.J. and Fairlie, G., 1993, Numerical Simulation of Impact and Fast Transient Phenomena Using AUTODYN^{TM}-2D and 3D, *Post-SMIRT Impact IV Symposium*, Bremen, Germany, August 1993.

Shanbing, Yu., Gengehen, Sun and Qingming, Tan, 1994, Experimental Laws of Cratering for Hypervelocity Impacts of Spherical Projectiles into Thick Target, *Int. J. Impact Engng.*, Vol. 15, No. 1, pp.67 - 77.

Stradling, G.L., G.C. Idzorek, P.W. Keaton, J.K. Studebaker, A.A. Hopkins Blossom, M.T. Collopy, H.L. Curling Jr., and S.D. Bergeson, 1990, Searching for Momentum Enhancement in Hypervelocity Impacts, *Int. J. Impact Engng.*, Vol. 10, pp555-570 (1990).

Stradling, G.L., Idzorek, G.C., Shafer, B.P., Curling, H.L. Jr., Collopy, M.T., Hopkins Blossom, A.A. and Fuerstenau, S., 1993, Ultra-High Velocity Impacts: Cratering Studies of Microscopic Impacts from 3 km/s to 30 km/s, *Int. J. Impact Engng.*, Vol. 14, pp.719-727.

Tanner, W.G., McDonnell, J.A.M., Yano, H. and Gardner, D.J., 1994, Meteoroids and Space Debris Hypervelocity Impact Penetrations in LDEF MAP Foils Compared with Hydrocodes Simulations, *Adv. Space Res.*, (in submission).

Tillotson, J.H., 1962, Metallic Equations of State for Hypervelocity Impact, *General Atomic Report AG-3612*, San Diego.

Vedder, James F., 1971, Microcraters in Glass and Minerals, *Earth and Planetary Science Letters*, 11, pp-291-296.

Vedder, James F. and Mandeville, J.C., 1974, Microcraters Formed in Glass by Projectiles of Various Densities, *J. Geophys. Res.*, 79, pp.3247-3256.

Appendix A

Workpackage P1

Optical Damage

Let x_p represent the diameter of a projectile and $z_p (x_p)$ represent the differential distribution function, i.e. the number of projectiles per unit range of x_p. We assume that the projectiles differ only in their diameters, i.e. they have the same velocity, shape and composition and are incident normally on the target.

For purposes of illustration only, we assume that z_p falls linearly with x_p from a value c at $x_p = 0$ to zero at $x_p = c/m$

$$z_p = c - m\,x_p \qquad\qquad x_p \leq c/m$$

$$= 0 \qquad\qquad x_p > c/m$$

The crater diameter x_c in a semi-infinite target is taken to be a simple multiple f times the projectile diameter:

$$x_c = f\,x_p \qquad \text{semi-infinite target}$$

The distribution function $z_c (x_c)$ for crater diameters in a semi-infinite target is then given by:

$$z_c = c/f - m\,x_c/f^2 \qquad x_c \leq c\,f/m \quad \text{semi-infinite target}$$

$$= 0 \qquad\qquad x_c > c\,f/m \quad \text{semi-infinite target}$$

where z_c and z_p are normalised to the same total number $(c^2/2m)$ of craters and projectiles respectively.

Now consider a target thin enough for penetration to occur, in the sense defined by Horz et al (1994a, 1994b). Denote the penetration limit for projectile and crater respectively by x_p' and x_c' where $x_c' = f\,x_p'$. We now assume that projectiles with diameter less than x_p' form craters identical with those for a semi-infinite target and that projectiles with diameter greater than x_p' form craters identical with those for a very thin target.

$$x_c = f\,x_p \qquad x_p \leq x_p' \qquad\qquad \text{finite target}$$

$$= x_p \qquad x_p > x_p' \qquad\qquad \text{finite target}$$

To calculate z_c for the finite target, we first note that 2 non-trivial cases exist:

case 1: $\qquad\qquad x_c' < c/m$

case 2: $\qquad c/m < x_c' < f\,c/m$

and that the case $f\,c/m < x_{c'}$ corresponds to a semi-infinite target since no penetration occurs.

Case 1: $x_{c'} < c/m$

$$z_c = c/f - m\,x_c/f^2 \qquad\qquad x_c < x_p'$$

$$= c(1 + 1/f) - m\,x_c(1 + 1/f^2) \qquad x_p' < x_c < x_{c'}$$

$$= c - m\,x_c \qquad\qquad x_{c'} < x_c < c/m$$

$$= 0 \qquad\qquad c/m < x_c$$

Case 2: $c/m < x_c < fc/m$

$$z_c = c/f - m\,x_c/f^2 \qquad\qquad x_c < x_p'$$

$$= c(1 + 1/f) - m\,x_c(1 + 1/f^2) \qquad x_p' < x_c < c/m$$

$$= c/f - m\,x_c/f^2 \qquad\qquad c/m < x_c < x_{c'}$$

$$= 0 \qquad\qquad x_{c'} < x_c$$

The distribution function $z_c\,(x_c)$ is plotted in Figure A.1 for specific values of c, m, f and $x_{c'}$. It is seen that a trapezoidal peak occurs in case 1 and a triangular peak in case 2. We emphasise that this calculation is not intended to model closely the real case but is meant only to give mathematical substance to a mechanism by means of which peaks may occur.
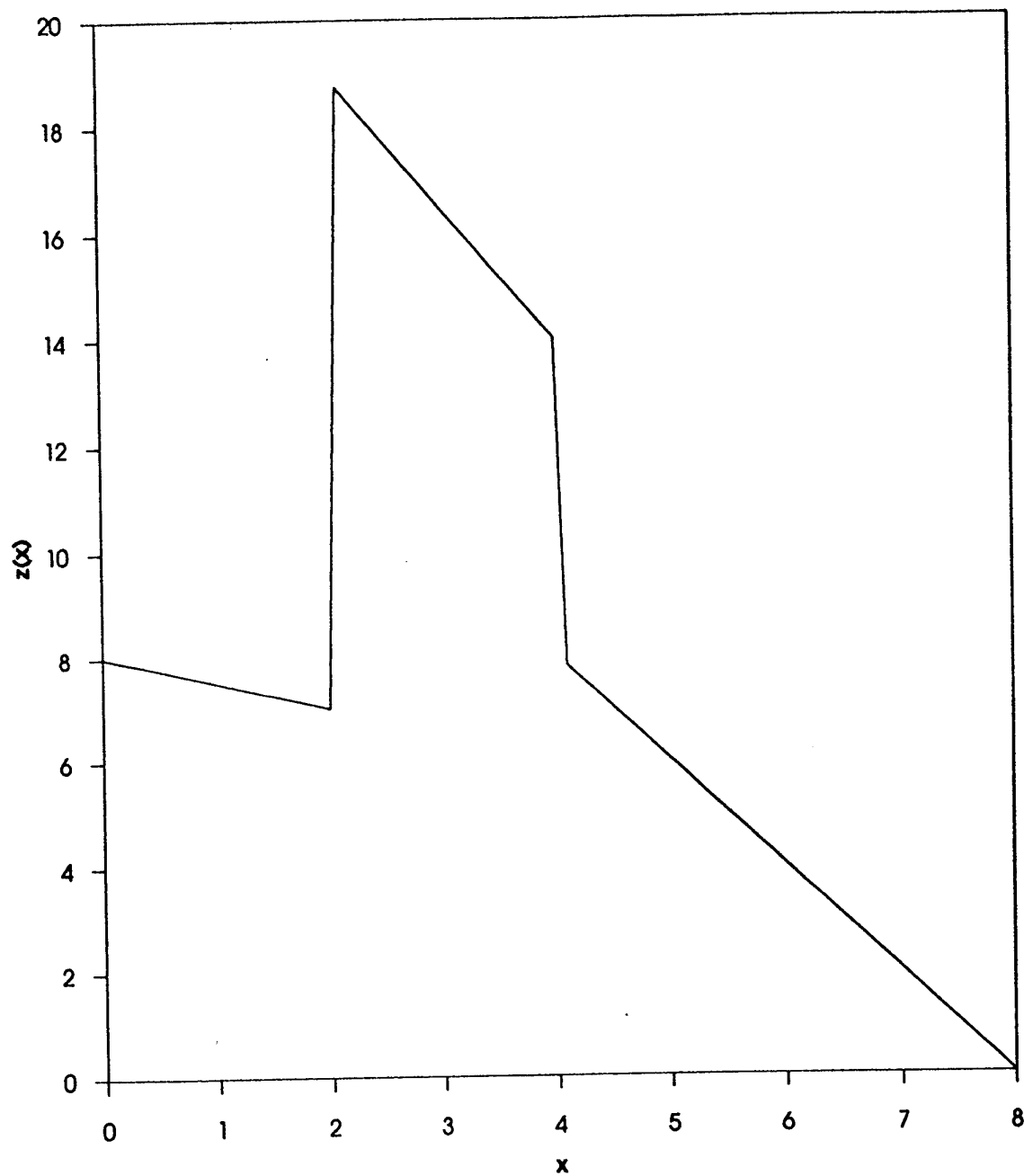
Figure A.1a Plot of z(x), the number of craters of diameter x per unit range of x, as calculated for case 1 in the Appendix.

CASE 2 with c=16, f=2, m=2, l=6.5
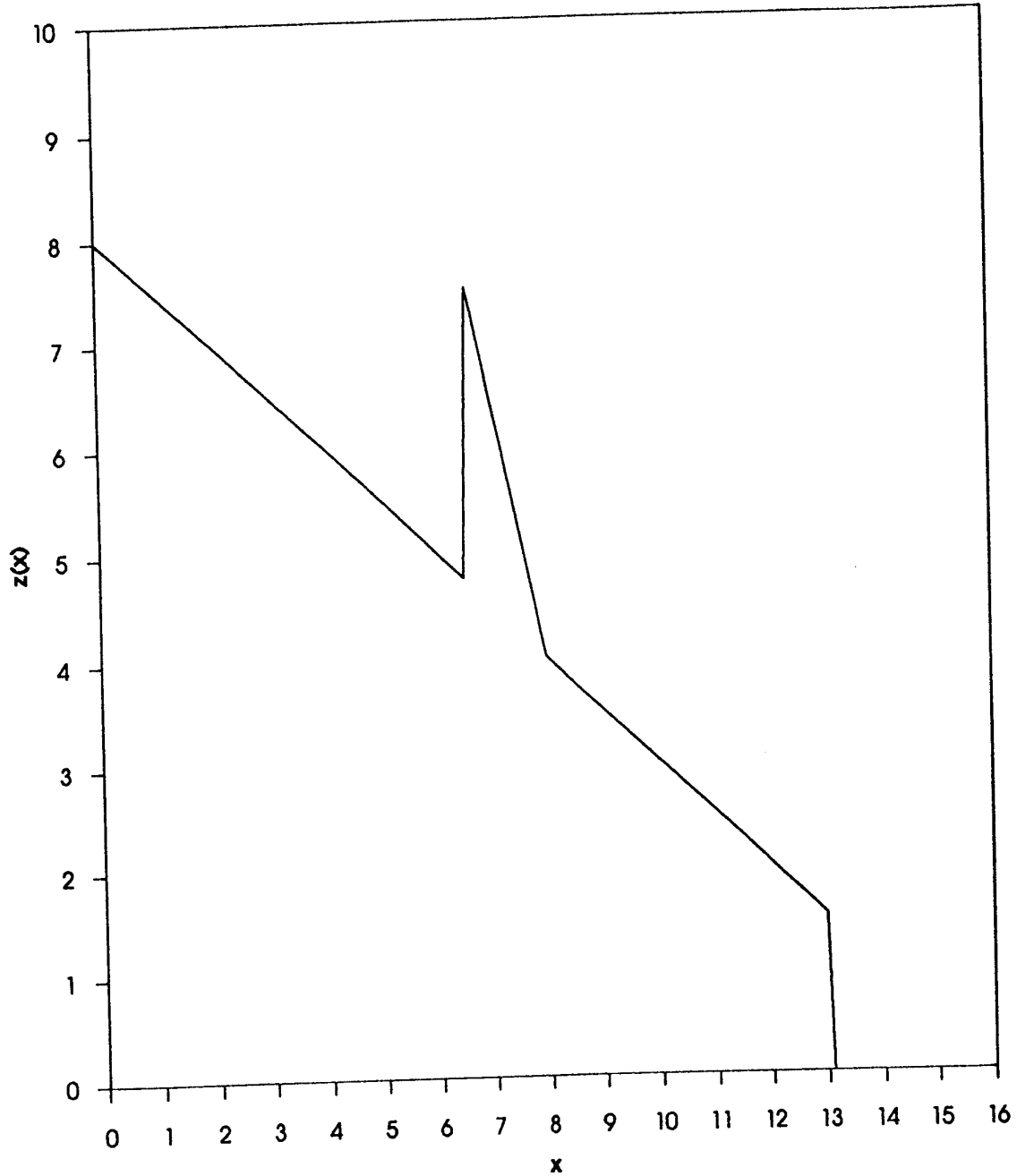
Figure A.1b Plot of z(x), the number of craters of diameter x per unit range of x, as calculated for case 2 in the Appendix.

Appendix B

Workpackage P3 - Energy Partitioning

Hydrocode Material Properties

The hydrocode simulations were performed using dimensions of μm, μs and pg, in order to aid computational accuracy by avoiding high value exponents in cell parameters. The equation of state and material model parameters were thus:

Aluminium 2024

Density	2.785
Hydro Tensile Limit	-1×10^{20}
Tillotson Parameter A	7.5×10^{7}
Tillotson Parameter B	6.5×10^{7}
Tillotson Parameter a	0.5
Tillotson Parameter b	1.63
Tillotson Parameter a	5
Tillotson Parameter b	5
Tillotson Parameter e0	5×10^{6}
Tillotson Parameter es	3×10^{6}
Tillotson Parameter esd	1.5×10^{7}
Reference Temperature	300
Specific Heat (C_v)	875
Shear Modulus	2.76×10^{7}
Yield Stress	2.65×10^{5}
Hardening Constant	4.26×10^{5}
Hardening Exponent	0.34
Strain Rate Constant	1.5×10^{-2}
Thermal Softening Exponent	0.55
Melting Temperature	775
Ultimate Strain	1×10^{20}

Iron

Density	7.86
Hydro Tensile Limit	-1×10^{20}
Tillotson Parameter A	1.279×10^{8}
Tillotson Parameter B	1.05×10^{8}
Tillotson Parameter a	0.5
Tillotson Parameter b	1.5
Tillotson Parameter a	5
Tillotson Parameter b	5
Tillotson Parameter e0	9.5×10^{6}
Tillotson Parameter es	2.44×10^{6}
Tillotson Parameter esd	1.02×10^{7}
Reference Temperature	300
Specific Heat (C_v)	452

Shear Modulus	8.0×10^7
Yield Stress	1.75×10^5
Hardening Constant	3.8×10^5
Hardening Exponent	0.32
Strain Rate Constant	6.0×10^{-3}
Thermal Softening Exponent	0.55
Melting Temperature	1811
Ultimate Strain	1×10^{20}

Appendix C

Workpackage P3 - Energy Partitioning

Cratering Equations

McDonnell-Sullivan:

$$\frac{f}{d} = 1.023d^{0.056} \left(\frac{\rho_p}{\rho_t}\right)^{0.476} \left(\frac{\sigma_{Al}}{\sigma_t}\right)^{0.134} v^{0.664}$$

Cour-Palais:

$$P = 5.24d_p^{19/18} \, H^{-0.25} \left(\frac{\rho_p}{\rho_t}\right)^{0.5} \left(\frac{v}{c_t}\right)^{2/3}$$

POD diameter:

$$(d_c/d_p) = 1.0857 \frac{(\rho_p/\rho_t)^{0.2857} \, (\rho_t/Y_t)^{0.2857} \, (c_t/c_p)^{0.2857} \, u_o^{0.5174}}{(1+(\rho_p/\rho_t)^{1/2})^{0.5714}}$$

POD depth:

$$P/d_p = (1/4)(4/3)^{1/3} \, (\rho_p/\rho_t)^{1/3} \, (\rho_t/Y_t)^{1/3} \left(c_{ot} + \frac{s(u_o - u_{t,crit})^2}{1+(\rho_t/\rho_p)^{1/2}}\right)^{1/3}$$

where:
$$s = (1+\Gamma)/2$$

$u_{t,crit}$ is a critical speed below which target material strength is not small compared with the impact stresses, given by:

$$u_{t,crit} = (2Y_t/\rho_p)^{1/2} \, (1+(\rho_p/\rho_t)^{1/2}$$

CTH diameter:

$$\frac{d_c}{d_p} = 0.468 \left\{\frac{(\rho_p/\rho_t)}{(1+(\rho_p/\rho_t)^{1/2})^2}\right\}^{0.33} (\rho_t/Y_t)^{0.258} u_o^{0.575} (c_t/c_p)^D$$

CTH depth:

$$P/d_p = 0.0275(\rho_p/\rho_t)^{0.60} \, (\rho_t/Y_t)^{0.263} \, u_o^{0.664}$$

In the all the above equations, the following symbols are used:

86

c = speed of sound
d = diameter
D = undetermined constant
f = maximum foil thickness penetrated
P = depth
u = impact velocity
Y= yield strength
Γ = Gruneisen coefficient

σ = density

and the subscripts denote:

Al = aluminium
c = crater
crit = critical value
p = impacting particle
t = target
o = initial state

Appendix D

Workpackage P3 - Energy Partitioning

Experimental Determination of Plasma Energies

Under the influence of an electric field, ions undergo an acceleration such that their change of velocity, Δv, is $\sqrt{(2Vq/m)}$ where V is the accelerating potential and q/m is the ion charge-to-mass ratio. The velocity is thus inversely related to the root of the mass, while the time-of-flight is directly proportional to the root of the mass. For the time-of-flight mass spectrometer geometry described under Workpackage P4, and indeed for any comparable linear system, it may be shown that this is true over each of the component sections of the instrument (acceleration region, drift region, detector entrance etc.), regardless of whether the field is planar, radial, or more complex. The ion times of flight in the geometry used for the pilot tests are thus

$$t = a\sqrt{m} + d\sqrt{m} + s\sqrt{m}$$

where a, d and s are constants for the accelerating region (i.e. between the target and the accelerating grid), the drift region (from the accelerating grid to the electron multiplier screen) and for the region between the electron multiplier screen and the collecting dynode.

The total times of light are thus simply

$$t = c\sqrt{m}$$

where $c = a + d + s$.

The values of a, d, s and hence c can be calculated if the geometry and field strengths are known precisely. However, if a large data set exists, it is simpler to derive the value of c. This was the approach adopted here.

The time-of-flight derivation above assumes that the ions have zero kinetic energy on formation, and that their velocities are determined purely by the accelerating field strengths. In practise, the actual energies of the ions on formation must have a component in the direction of the accelerating field (the opposite direction is precluded by the presence of the target plate), and so act to reduce the time-of-flight and the effective value of the constant c. The value of c may thus be calculated individually for every line in every measured mass spectrum, and the maximum value obtained is an approximation to the 'true' zero-energy value.

This zero-energy value of c may then be used to calculate the nominal line positions in the spectra, and hence derive the displacements, Δt, of each line from its nominal position.

The ion total kinetic energy

$$KE \propto v^2 \propto 1/t^2$$

and so

$$\Delta KE/KE = 2\Delta t/t$$

where ΔKE is the initial energy of the ion and KE is the energy imparted by the accelerating field. In our case, KE is effectively 1000 eV due to the 1 kV accelerating field as the 3 kV acceleration between the electron multiplier screen and the collection dynode only influences the last few nanoseconds of the ion flight.

It is thus straight-forward to derive the kinetic energy of each ion species in each spectrum individually from the displacement of the line from its nominal position. It should be remembered that the above treatment does not calculate the absolute energy of the ions, rather the energy relative to the lowest energy line in any of the spectra. However, if the data set is large enough and covers a wide range of impact velocities, the distinction should be negligible. This study is based on 99 spectra covering the range 1.6 to 42.1 kms^{-1}. Although the energy derived is the component in the direction of the target normal, Ratcliff and Allahdadi (1994) showed that ion trajectories are focused to a considerable extent ($\sim\cos^3$) in the direction of the target normal and so this component will be dominant.

Appendix E

Workpackage P3 - Energy Partitioning

Publication

The following paper was presented at the 30th Scientific Assembly of the Committee on Space Research (COSPAR), Hamburg, Germany, 11th-21st July 1994, and has been accepted for publication in Advances in Space Research.

Publication of other results of this Workpackage is under discussion.

CHARACTERISTICS OF THE PLASMA FROM A 94 kms⁻¹ MICRO-PARTICLE IMPACT

Paul R. Ratcliff[1] and Firooz Allahdadi[2]

[1]Unit for Space Sciences, University of Kent, Canterbury, Kent, CT2 7NR, U.K.

[2]PL/WSSD, Kirtland AFB, Albuquerque, NM, USA.

ABSTRACT

The energies of the positive ions produced by the impact of a 70 nm boron carbide particle on an aluminium target at a velocity of 94 kms⁻¹ have been derived for each ion species observed in the resulting time-of-flight mass spectrum. The results allow major conclusions to be drawn about the plasma energetics, and more tentative conclusions about the energy partitioning in the event.

INTRODUCTION

The phenomenon of plasma production by hypervelocity impact has been known for over 30 years /1/. A considerable amount of work has been published concerning the ion yield from hypervelocity impact events /eg 2, 3/ and in terms of the number of ions produced, the process is well characterised, at least empirically. However, there have been few studies of the energies of the plasma ions, particularly involving direct measurements and at very high velocities. Früichtenicht, Roy and Becker /4/ used the Saha equation to estimate the temperature of impact plasma (and hence the average ion energies) from the relative abundance of ions of different isotopes produced by impact on an isotopically well-defined target containing three metals. In the current work, however, the experiment configuration allowed the ion energies to be derived directly from the measurements.

EXPERIMENT CONFIGURATION

The data was obtained using a prototype of a large area impact plasma time-of-flight mass spectrometer that was under development on the dust accelerator facility at the University of Kent, and which has since been incorporated as a subsystem in the Cosmic Dust Analyser experiment on the Cassini/Huygens mission /5/. The experiment configuration was as shown in Figure 1. Dust particles were impacted on the target dish and the ions produced separated by the intense electric field sustained between the target and a fine grid (1 kV over 3 mm) such that the positive ions were focused on the electron multiplier. Since the energetics of a hypervelocity particle impact preclude multiply ionised states, the velocity imparted to the ions by the accelerating field is a function of the ion mass only, and the signal from the electron multiplier represents a time-of-flight mass spectrum.

In a conventional mass spectrometer, energy focusing is used to eliminate (at least to first order) the contribution of the initial thermal energy of the ions to their times of flight. In this system, due to the requirement for a large sensitive area and compatibility with simultaneous operation of other subsystems in the flight instrument, an adequate mass resolution ($m/\Delta m \sim 70$) is achieved by using an accelerating potential that is large compared with the thermal energy of ions from a typical impact.

The absence of energy focusing results in the line profiles in the mass spectra directly reflecting the initial thermal energies of the ions. The effect is small for most events (by design) but during the study one event was recorded with an anomalously high velocity of 94 kms⁻¹. Usually the dust accelerator only achieves such velocities for particles that are too small to be logged by the in-flight detection system. In this case the particle mass was measured as 4×10^{-4} pg (70 nm diameter).
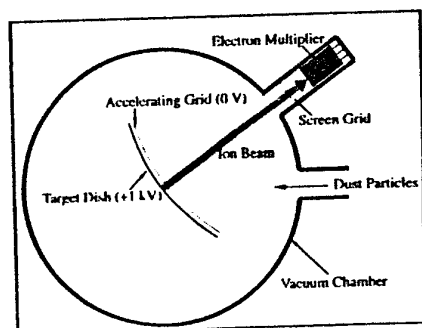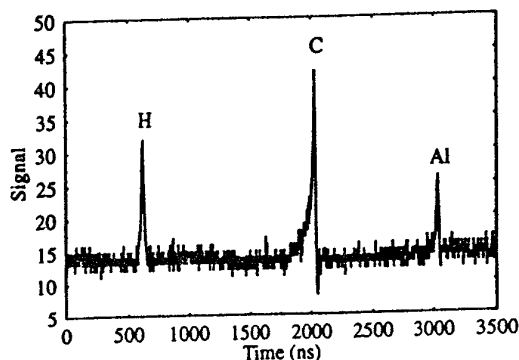

Fig. 1. Schematic of the experiment configuration.

Fig. 2. Mass spectrum obtained from the 94 kms⁻¹ boron carbide particle impact.

ANALYSIS

The mass spectrum obtained from the 94 kms⁻¹ impact is shown in Figure 2. The lines have been positively identified (from the timing signal provided by electrostatic detection of the incident particle) as hydrogen, carbon, and aluminium. However, the aluminium line may also include a contribution from C_2H_3 cluster ions (also mass 27) which are produced from hydrocarbon contamination of the target surface and are commonly seen in impact mass spectra. The most noticeable qualitative feature of the spectrum is the asymmetry of the aluminium and, especially, the carbon line.

The target plate was aluminium with an evaporation coating of (nominal 20 μm) silver. The presence of the aluminium line was thus expected, while the absence of the silver doublet is probably due either to poor coverage by the coating at the impact site, or to erosion of the silver by previous impacts. The carbon ions will be partly from the boron carbide particle and partly from hydrocarbon contamination of the target by vacuum pump oil as a clean vacuum system was not available at the time of the experiment. The hydrogen ions are also explained by this source, and by hydrogen adsorption. The boron line would occur on the leading edge of the carbon line, but there is no evidence for its presence as even a weak line should be resolvable. This is believed to be due its tendency to form negative ions, which are not detected by this system. Evidence to support this comes from other spectra where the boron line is missing, and spectra from iron particle impacts where the iron line shows a similar profile.

Comparing expanded views of the line profiles with the response function of the electron multiplier (10 ns width) (Figure 3), the strong influence of the initial ion energies is apparent, even in the case of the hydrogen line.
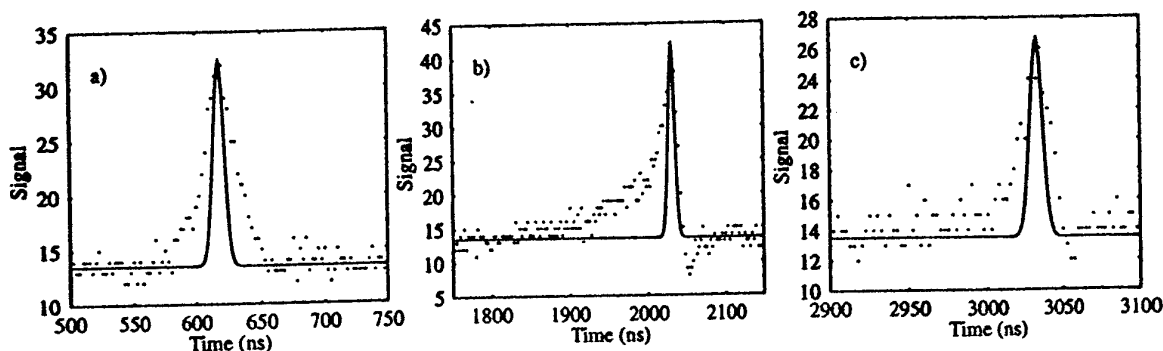

Fig. 3. Comparison of line profiles (dots) with the multiplier response function (lines): a) Hydrogen, b) Carbon, c) Aluminium

Using a computer program that accurately simulates the experiment configuration, the energy and angular distributions in the initial plasma required to produce the observed line profiles can be found. Those assessed in this study were Maxwellian distributions (implying thermal equilibrium in the impact plasma), Gaussian energy and velocity distributions, and an empirical energy distribution derived for laser-irradiation-induced plasma /6/. The physics of plasma production by laser irradiation is fundamentally different to production by particle impact, but the distribution is a methematically convenient function with a form intermediate between Gaussian and Maxwellian. These possibilities have been tried with a variety of angular distributions, including isotropic, cos, cos^2, cos^3, sin, sin^2, sin^3 (measured relative to the target normal) and Gaussians centred on the target normal and at 45 and 90 degrees.

The assumption has been made throughout the calculations that the time-spread of the plasma production is smaller than the time-resolution of the measurements (2.5 ns). This is supported by simulations of the impact using the CTH hydrocode which suggest that plasma production does not extend beyond ~1ns after the impact.

RESULTS

The hydrogen and carbon lines can be fitted best by a Gaussian energy distribution, ie by assuming that the ion energies are randomly distributed about a mean value and that the plasma is not in thermal equilibrium. The laser-ionisation distribution can provide a good fit to the carbon line only, while the other distributions can not reproduce the form of the leading flanks of the lines (Figure. 4).

The energies required to produce the optimum fits are 160 ± 16 eV for the hydrogen line and 40 ± 25 eV for the carbon line. These energies correspond to effective temperatures of 1.2×10^6 K and 3×10^5 K, and ion velocities of 180 kms⁻¹ and 25 kms⁻¹ respectively. The energies of the two species can thus be seen to be entirely different. Further, these values are extremely large, particularly for the hydrogen line -

Friichtenicht et al /4/ derived temperatures of metallic target ions of the order 6000 K for velocities of 17-47 kms⁻¹. However, it should be remembered that the impacting particle velocity here was 94 kms⁻¹ and that ejecta can be emitted with velocities greatly in excess of the impactor velocity /eg 7/, particularly during the early stages of the impact process and at low ejection angles (relative to the target plane). Since the hydrogen is presumed to be present only at or near the surface of the material, its production may be expected to be linked to this early-phase high velocity jetting. However, the angular distribution for the hydrogen line is of the form $\cos^3$, indicating a considerable degree of focusing along the target normal rather than near the target plane.
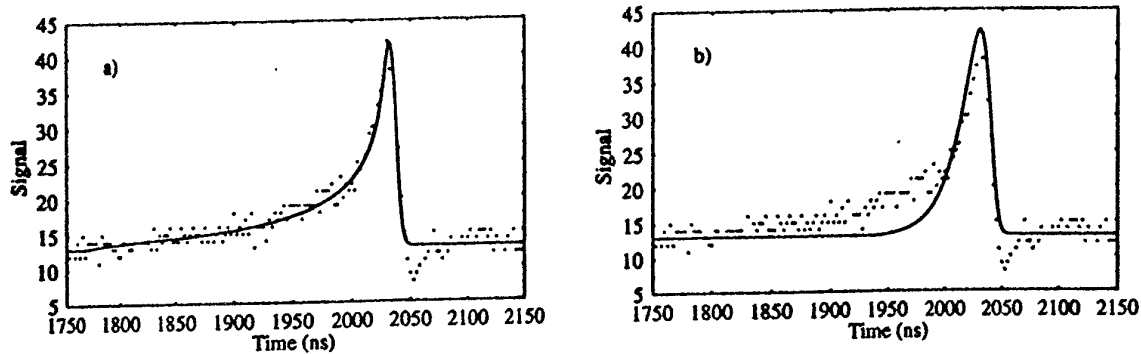
Fig. 4. Optimum theoretical fits to the carbon line: a) Gaussian energy distribution ($E = 40 \pm 25$ eV, $\theta = 0 \pm 30°$), b) Maxwellian distribution ($T = 40,000$ K, $\theta \sim \cos$).

The derived energy for the aluminium line, by contrast, is only 9.7 eV, corresponding to a temperature of 7.5×10^4 K and a velocity of 8.3 kms⁻¹. This is more in keeping with the results of Friichtenicht et al /4/, and is a more valid comparison as aluminium is the target material rather than a contaminant. The aluminium is quite possibly evolved at a later stage in the impact process, following consumption of the particle and contaminants, and thus at a lower energy. The angular distribution still shows focusing in the direction of the target normal, though to a lesser degree characterised by a $\cos^2$ distribution.

Since the carbon seen in the spectrum has more than one source (the particle itself and hydrocarbon contamination) its line profile may be characteristic of more than one energy distribution - the high energy early phase producing the flank, with the energy decreasing in the later stages to produce a narrower (and slightly later) superimposed peak. It should be noted that the times referred to here do not reflect varying positions on the time axis of this spectrum - the times involved are too small. It is the change in energy with time after impact that is important in this context.

Energy Partitioning

Having derived the characteristic plasma energetics, we can move on to consider some aspects of the energy partitioning in this event. The absolute number of positive ions of each species is given in Table 1, derived from the calculated electron signal and from the relative line strengths in the positive ion spectrum. Unfortunately the electron signal was not recorded, and so the total ion yield is derived from an empirical relationship based on other data taken with this experiment configuration. This data lies in the range 2 to 40 kms⁻¹, and so extrapolation to 94 kms⁻¹ involves a degree of uncertainty. The numbers of ions of each species are multiplied by their derived mean energies to give the total kinetic energy of the plasma - ~2.9% of the particle kinetic energy.

The number of aluminium ions corresponds to a solid phase volume of 1.1×10^{-16} cm³, or a crater ~4×10⁻² μm deep (assuming hemispheric form). Unfortunately the impact site can not be identified as there are thousands of impacts on the target, but using the Cour-Palais cratering formula /8/ we would expect a crater depth of ~1.6 μm, so the detected ions represent only a tiny fraction (0.4%) of the aluminium lost from the impact site. The remainder is presumably accounted for by ejecta.

The number of carbon ions corresponds to a volume of boron carbide of 4.4×10^{-15} cm³, or a sphere of 200 nm. This is three times the size of the original particle (70 nm), and so it is clear that the majority of the carbon ions come from contaminants.

The energy required to ionise all the ions is ~5.5×10^7 eV, or 0.5% of the particle kinetic energy. Although the ions are in not in thermal equilibrium, we may make a tentative estimate of the degree of ionisation in the evolved vapour from the Saha equation for the derived effective temperatures. The result is ~100% ionisation in each case. Assuming this, the energy required to vaporise the aluminium can be

estimated as 2.9×10^6 eV, or 0.03% of the particle kinetic energy. Since the original chemical forms of the hydrogen and carbon ions are not known the same estimate can not be made. However, of the possible forms of the carbon, that with the greatest heat of fusion will be boron carbide, and so an upper limit to the energy can be calculated as ~8.6×10^7 eV, or ~0.9% of the particle energy. It is reasonable to assume total vaporisation of the particle at this extreme impact velocity, which provides a lower limit to the energy of ~2.9×10^7 eV, or ~0.3%.

DISCUSSION

TABLE 1 Summary of results. All energies are in eV. Figures in brackets are the percentage of the incident particle kinetic energy.

	Characteristic Ion Energy	Emission Angular Distribution	Number of Ions	Total Ion Energy	Total Energy of Ionisation	Total Energy of Vaporisation	Total Energy
H	160	~$\cos^3$	1.2×10^6	1.9×10^8 (1.7%)	1.6×10^7 (0.15%)	Undefined	$\geq 2.1 \times 10^8$ (1.9%)
C	40	~$\cos^3$	3.1×10^6	1.2×10^8 (1.1%)	3.5×10^7 (0.32%)	$\geq 2.9 \times 10^7$ (~0.3%)	$\geq 1.8 \times 10^8$ (1.7%)
Al	9.7	~$\cos^2$	7.0×10^5	6.8×10^6 (0.06%)	4.2×10^6 (0.04%)	2.9×10^6 (0.026%)	1.4×10^7 (0.13%)
Total			5.0×10^6	3.2×10^8 (2.9%)	5.5×10^7 (0.50%)	$\geq 3.2 \times 10^7$ (~0.3%)	$\geq 4.0 \times 10^8$ (3.7%)

Table 1 summarises the results obtained in this study. Certain conclusions can be drawn with confidence:
a) Impact plasma trajectories are focussed to a considerable degree in the direction of the target normal, although the angle of incidence of the particle was 36° from this. The degree of focusing is lower for the lower energy species.
b) The ions are not in thermal equilibrium and can be characterised by a random energy distribution.
c) The different ion species have different characteristic energies. These differ by over an order of magnitude, and may reflect the difference between early stage surface effects and later vaporisation and ionisation of the bulk material.

Extension of the analysis to calculate the crater volume and the energy partitioning in the event involves a number of assumptions and extrapolation of formulae from lower velocity regimes. However, reasonable confidence can be placed in the results. So, about 4% of the particle kinetic energy has apparently gone into impact plasma production. This is the only such measurement for such a high velocity impact although at much lower velocities (~6 kms⁻¹) the percentage is believed to be <1% /9/. However, other events in this data set are available for analysis, covering the velocity range 1.7-25 kms⁻¹, and other data sets extending the range to ~40 kms⁻¹. These will allow the velocity dependence of impact plasma ion energies to be investigated, and will be published at a later date.

ACKNOWLEDGEMENTS

REFERENCES

1 J.F.Friichtenicht and J.C.Slattery, Ionization Associated with Hypervelocity Impact, NASA TN D-2091 (1963).
2 J.Kissel and F.R.Krueger, Ion Formation by Impact of Fast Dust Particles and Comparison with Related Techniques, *Appl. Phys. A*, 69-85 (1987).
3 F.R.Krueger, Thermodynamics of Ion Formation by Fast Dissipation of Energy at Solid Surfaces, Z. Naturforsch. Vol.38a, 385-394 (1983).
4 J.F.Friichtenicht, N.L.Roy and D.G.Becker, The Cosmic Dust Analyzer: Experimental Evaluation of an Impact Ionization Model, in: Evolutionary and Physical Properties of Meteoroids, NASA SP-319, 299-310 (1971).
5 P.R.Ratcliff, J.A.M.McDonnell, J.G.Firth and E.Grün, The Cosmic Dust Analyser, *J. British Interplanetary Society* Vol.45, 355-358 (1992).
6 R.Dinger, Energie- und Winkelverteilung Lasererzeugter Plasmaionen, Diploma Thesis, University of Kaiserslautem, 1980.
7 G.Eichom, Primary Velocity Dependence of Impact Ejecta Parameters, *Pl. Sp. Sci.* 26, 469-471 (1978).
8 B.G.Cour-Palais, Hypervelocity Impacts in Metals, Glass, and Composites, *Int. J. Impact Engng.* Vol.5., 681-692 (1987).
9 D.E.Gault and E.D.Heitowot, The Partition of Energy for Hypervelocity Impact Craters formed in Rocks, *Proc. 6th Hypervelocity Impact Symposium* Vol.2, 419 (1963).

Appendix F

Workpackage P4

Publications

There has already been one paper (Burchell et al, 1994) generated during this work. This is to appear in the proceedings of COSPAR 1994. A copy is attached. We also include Burchell et al, 1993, which contains a description of the hypervelocity impact facilities at the University of Kent.

As stated in the conclusions (above) data is currently being collected using the chamber. This should result in at least 2 publications during the next year.

USE OF COMBINED LIGHT FLASH AND PLASMA MEASUREMENTS TO STUDY HYPERVELOCITY IMPACT PROCESSES

M.J.Burchell, L.Kay and P.R.Ratcliff
Unit for Space Sciences, University of Kent, Canterbury, Kent, CT2 7NR, United Kingdom.

ABSTRACT

We present new measurements concerning generation of light flash during hypervelocity impacts. We use iron particles (10^{-13} to 10^{-17} kg) with velocities over the range 1 to 42 km/s impacting semi-infinite targets (aluminium and molybdenum). The main results of previous work in the field are found to be reproduced with some slight deviations. For iron projectiles with given mass and velocity the energy of the flash (normalized to mass) is proportional to velocity to the power of 3.5 for aluminium targets and 3.9 for molybdenum targets. The duration of the flash is of order 1 microsecond. Simultaneous measurements of the generation of impact plasma do not change this. The onset of plasma generation of the bulk target material does not affect the total light flash energy. We discuss the duration of the flash compared to the temperature in the target and plasma vs time.

INTRODUCTION

For hypervelocity impacts involving small, dust-like particles on semi-infinite targets the standard experimental results on light flash are often taken as /1,2,3,4/. There it was found that: the light flash comprises two parts, that of the main impact, and that from secondary impacts of ejecta; that the flash lasts on time scales of 100 microseconds; that the light energy (normalized to projectile mass) is proportional to the incident velocity to a power in the range 3.0 to 3.6 (dependent on projectile and target composition); that the intensity is related strongly to the melting temperature of the target material (for a given projectile); and that the temperature related to the flash is in the range 2500 to 5000 K. Recently there has been renewed interest in light flash from hypervelocity impacts of dust particles. Accordingly we have carried out a program of work checking previous results and addressing new issues.

EXPERIMENTAL SETUP

The hypervelocity impacts are produced in the Accelerator Laboratory at the University of Kent. We use a 2 MV Van de Graaff accelerator which contains a dust source which can be electrostatically charged. After acceleration the dust particles enter a target chamber evacuated to 1 or 2×10^{-6} mbar. Metal targets are placed in the chamber and can be viewed through windows by photomultiplier (pm) tubes. Particle charge is measured by means of pickups in the beam-line. Two such pickups with known separation give the particle velocity (good to 2% at 3 km/s, and 5% at 40km/s). The particle mass is found from the particle charge and velocity combined with the accelerating voltage (relating energy of acceleration to kinetic energy). The accuracy of the mass is typically 1% at low velocity, rising to 5% at higher velocities. The range of velocities and masses used is illustrated in Figure 1 (a genuine data run).

During the studies two pm tubes were used, an EMI 6097, operated at 1.4kV and room temperature and an EMI 9789Q, operated at 1.4kV and cooled to -20°C. Various geometric arrangements of target and pm were used, i.e. varied angle of incidence of the projectile and varied viewing angle of the pm (normal and parallel to the target surface and other angles between). No preferred geometry was found, nor was one pm found to provide results not available from the other. During studies of plasma production the metal target had an earthed grid placed 0.4 cm above it, with a potential difference of 1000V between the two. An electron multiplier was placed at the wall of the chamber, with its main axis normal to the target surface. An earthed grid is front of the electron multiplier which is operated at -3kV. With this arrangement ions liberated in the hypervelocity impact are accelerated away from the target surface, then drift in a straight line to the electron multiplier. For any ion species the drift time is inversely proportional to the square root of the mass. The relative positions of the signals (compared to each other and the start drift time) thus permit identification of the ion species.
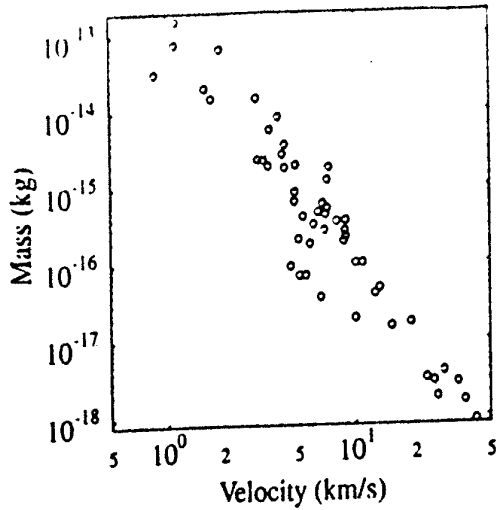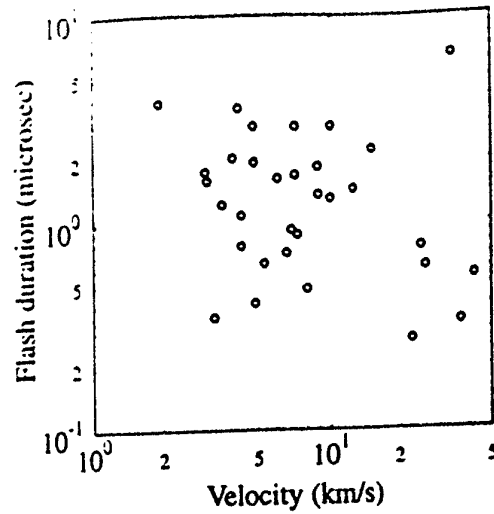
Fig.1 Mass and velocity in data used.

Fig. 3 Duration of flash.

RESULTS

The pm tubes have been operated with integration of the charge collected on their base, so the total magnitude of their signal is proportional to the total light energy (E) of the event. In Figure 2 we show light energy normalized to particle mass (E/m) vs velocity for impacts of iron (Fe) particles on aluminium (Al) and molybdenum (Mo) targets. It is clear that a relationship holds over the range 1 to 50 km/s. For Fe on Al we find the data well described by $E/m = a_i*v^{3.5}$, for Fe on Mo we find $E/m = a_i*v^{3.9}$ (a_i differs for each target-projectile combination). These curves are shown on Figure 2. For Fe impacting Al the fit shown was made at just high velocities, and is shown extrapolated to the low velocity data points with good results. Separate runs for Fe -> Al with the bulk of the data at low velocity show similar slopes. From the results for both targets we can see the relationships hold good even though E/m varies by 6 decades in magnitude over the observed velocity range. This is in line with /1,2/ where similar results were found with typical powers of 3.0 to 3.6. The power found here is not sensitive to which pm tube is used, and is stable with repeated runs. For the data in Figure 2b (Fe on Mo) there is a hint that a shoulder is present in the range 7.5 to 9 km/s. This data is replotted in Figure 2c with separate fits above and below this region. The power law behaviour is again found in both regions, but below 7.5 km/s the power is 4.4 and above 9 km/s it is 4.05. This fit is somewhat better than the single fit, but it does not include the region around 8 km/s, automatically improving the quality of the fit. The suggestion made previously is that such kinks in the E/m vs v data represent kinematic regimes where the temperature in the target reaches its melting point /2/. We also note that, as shown below, generation of Mo plasma occurs from approximately 19 km/s upward, not coincident with any feature in the data.

Since the pm signal is integrated, the rise time of the signal represents the total duration of the flash. In Figure 3 we show the rise times of the integrated pm signal for Fe on Mo. These are typical of the results also obtained for the Al target, and are again not dependent on pm tube. Although a large scatter is present, two general results stand out. The first is that the time scale of the impact flash is of order 1 microsecond. Second, there is possibly a weak inverse dependence of flash duration on impact velocity. It is interesting to note that when the set-up for plasma measurements is used simultaneous with light flash observation, the flash duration shows no change larger than the scatter observed in Figure 3.

For impacts of Fe on Mo simultaneous light and plasma signals were recorded. In each event plasma signals were searched for. The time of the impact is as given by the start of the rise of the pm signal. This provides a t_0 for the event good to 10 nsec. By taking the observed centre of the signal for a species in a given impact, and comparing to the value predicted solely by mass (i.e. with zero initial energy), we obtain estimates of the initial energy. This is shown in Figure 4 for each species found in the impacts studied. Molybdenum is not shown in Figure 4, as the time of flight signals are so wide that the centre of the peak is accurate only to the same scale as the expected deviation in peak position. Although Fe and Mo are the expected signals, surface contaminants are also present and explain the hydrogen, carbon, sodium, aluminium and potassium observed. Not all species are seen at all velocities, with a velocity
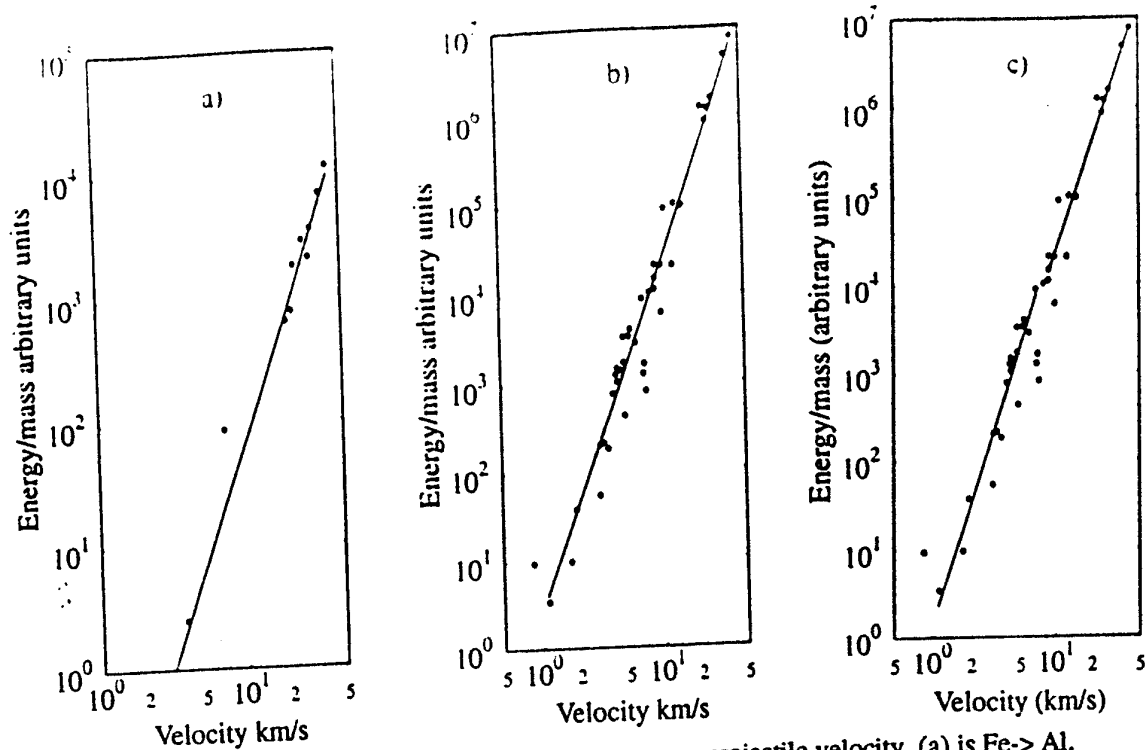
Fig.2 Total light energy normalized to projectile mass vs projectile velocity. (a) is Fe-> Al, (b) and (c) are Fe -> Mo. See text for details of fits.

threshold effect being present /5/. Mo for example is only seen in our data above 19 km/s. The lack of data continuous with velocity makes the exact threshold velocity hard to identify. Naively an increase in initial energy was expected with increasing velocity, but this is not supported by these initial results. A possible explanation is that at higher velocities the target and projectile species dominate the plasma, and energy is transferred to them from the lighter ion species by inelastic collisions. hence at high impact velocities seeming to reduce the energy at production for the contaminant species.

DISCUSSION OF RESULTS

The data show clear relationships for E/m vs v. This varies with target material, and may also be assumed dependent on the composition of the projectile. The data does show a degree of scatter, it is traditional to assign this to the influence of ejecta and secondary impacts in affecting the observed light yield. When considering the origin of the light flash we focus on the duration of the impact flash. This is typically 1 microsecond. We consider the case of an iron particle of mass 3×10^{-16} kg incident normally on molybdenum with a velocity of 10 km/s. The impact and cratering proceed on time scales of a few nanoseconds. Assuming that all the incident energy is deposited in the target during this time (an over cautious approach as it ignores ejecta, vaporisation of material, etc), we have used a simple 3 dimensional model of heat flow in metals to calculate the persistence of elevated temperatures in the target. The model uses the normal 3-D heat conduction equation for heat transfer in homogeneous solids to let heat energy flow away through the target material, and ignores loss of heat from the surface (e.g. radiation, evaporation etc). The incident energy is applied to the target distributed with a Gaussian profile whose width can be varied. We quote this distance r in units of the projectile radius. Ignoring any concurrent changes of state. we find the following peak elevated temperature T for different choices of r: r = 1, T = 81.200 K; r = 2.5, T =5,900 K; r = 3, T= 2830 K; r = 5, T = 741 K. We find T has its peak value at the centre of the impact site and falls by 1/3rd at the edge. Within the first nanosec. at twice the radius of the site the temperature is 1/10th of the peak. After 100 nanosec the peak temperature found anywhere in any example is less than 30 K above ambient. Therefore. in such a simple model, light emission from the crater is limited to a period shorter than the observed light flash duration by at least an order of magnitude. One thus' has to consider some other source. e.g. plasma or ejecta. Using the initial energy of the plasma shown in figure 4. we can see that 10 eV is already well beyond the ultra violet region and into the soft x-ray region of the electromagnetic spectrum. Assuming black body emission the associated visible light flash would be of enormous magnitude. and correspond to a peak temperature of some 75,000 K (we simply assume the kinetic energy of an ion = 3kT/2). We therefore deduce that the
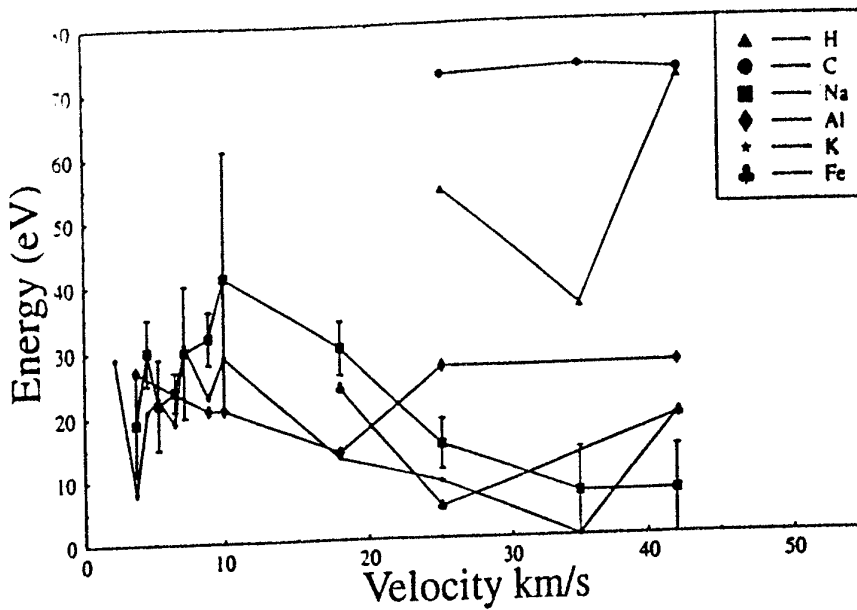
Fig. 4 Initial energy in the plasma for each ion species.

plasma is in a regime where radiant emission is decoupled from its internal energy. The time scale over which the plasma is maintained over the surface and the cooling rate would be of interest in persuing this line of thought further. We note that when we measure plasma production we do so by introducing an intense field above the target surface. This will separate the electrons and the ions in the plasma on very short time scales, preventing recombination being a prolonged source of the light flash. Yet total duration and magnitude of the light flash are observed as before. Ejecta are thus a more plausible source for the bulk of the light flash signal. Although some ejecta may show velocity enhancement, for discussion we simply assume that the typical ejecta velocity is that of the incident projectile. Thus for a 10 km/s impact, in 1 microsecond ejecta will travel 1 cm. certainly still within the field of view of the optics used in this paper. Further, in the vacuum the ejecta will only lose heat by radiation and evaporation. so will retain their initial temperature over large time scales.

CONCLUSIONS

Light flash in small dust particle hypervelocity impacts is shown to be a phenomenon whose characteristics (e.g. energy) follow clear relationships indicating underlying physics. It should therefore be possible for a succesful theory of emission which reproduces these relationships to be expounded. As indicated in the discussion section above the source of the light needs to be considered carefully when predicting its behaviour. For example. the data presented here is not dominated by either surface glow or light from the plasma.

REFERENCES

1. G.Eichorn, Measurement of the light flash produced by high velocity particle impacts. Planetary and Space Science. 23, 1519 (1975).
2. G.Eichorn, Analysis of the hypervelocity impact processes for impact flash measurement. Planetary and Space Science. 24, 771 (1976).
3. G.Eichorn, heating and vaporization during hypervelocity particle impact, Planetary and Space Science. 26, 443 (1978).
4. G.Eichorn, Primary velocity dependence of impact ejecta parameters, Planetary and Space Science 26, 469 (1978).
5. B.K.Dalmann, E.Grun and J.Kissel. Ion composition of the plasma produced by impacts of fast particles, Planetary and Space Science. 25, 135 (1977).

THE HYPERVELOCITY IMPACT FACILTIES AT THE UNIVERSITY OF KENT AT CANTERBURY (UK).

M.Burchell, J.A.M.McDonnell, M.J.Cole and P.R.Ratcliff. Unit for Space Sciences, University of Kent, Canterbury, Kent CT2 7NR, United Kingdom.

Abstract:
The University of Kent at Canterbury (UK) facilities for production of hypervelocity impacts are described. Micrometeroids are simulated by electrostatic acceleration of small (10^{-12} to 10^{-17} kg) particles using a 2 MV Van de Graaff accelerator. This machine has been operational for many years; both the machine and experimental area are currently being upgraded. Larger particles (10^{-10} to 10^{-4} kg) are accelerated using a more recently installed light gas gun. The status of all hardware (including experimental areas) is given, along with brief details of recent, current and future projects making use of them.

Introduction

The Unit for Space Sciences at the Univ. of Kent (UK) has an extended history of studies of micrometeroids. The design, manufacture and calibration of micrometeroid detectors has been one of the group's major activities. An important tool in this process has been the laboratory simulation of hypervelocity impacts on selected target materials. Traditionally the Unit has achieved this using electrostatic acceleration of (charged) microparticles in a 2 MV Van de Graaff accelerator (operational at Kent since 1974). More recently a light gas gun has been installed, explosively accelerating larger particles. This extends the projectile mass regime from micro (order 10^{-15} kg) to macro (10^{-4} kg) particle size. Details of these devices are given below, along with descriptions of their current use.

2. Van de Graaff Accelerator (2MV)

This has been operational at Kent since 1974. It is one of only two such installations which have been continuously available for microparticle acceleration over the years. The other is also a 2 MV machine, at the Max Planck Institut für Kernphysik, Heidelberg, Germany [1]. (Note also that a 6 MV machine was used at Los Alamos for similar work at the end of the 1980's [2]).

The machine has been described in detail previously [3], so only brief details or new information are given here. A dust reservoir is at the high voltage end of the machine (top terminal). This is kept at 15 kV above the 2 MV of the rest of the top terminal, and is pulsed at 1 Hz to just 1 KV above 2 MV. Charged dust is then directed onto a needle tip positioned in front of a small hole in the base plate of the top terminal. The most efficiently charged particles arrive at the needle tip and are exposed to the potential difference between the top terminal and the

earthed far end of the machine. They thus accelerate through the hole in the top terminal base plate and along a flight tube which runs the length of the machine. The 2 MV potential difference is linear along the length of the flight tube, and is maintained by 52 equally spaced ring electrodes. Between the top terminal and the first of these is a cylindrical tube maintained at a voltage set by the machine operator. The field at the entrance and exit of this cylinder serves as a focusing element for the beam. The main axis of the accelerator is horizontal, and the flight tube is approximately 2 metres in length. Whilst the flight tube is maintained under a vacuum of some 10^{-6} mbar, the rest of the accelerator is filled with a dry gas (20% CO_2 and 80% Nitrogen, mixed with a trace of SF_6) at 100 to 150 psi. This is to prevent sparking and breakdown of the potential.

Although the potential is 2 MV, due to the mass of the microparticles the acceleration is totally non-relativistic. Thus we can write that the kinetic energy is simply the energy gained by acceleration:

$$0.5 \, m v^2 = q V$$

where m is particle mass, v its final velocity, q its charge and V the accelerating potential. It can thus be seen that v is a function of q/m. For fully efficient charging, the charge is a surface effect, and thus (for perfectly spherical particles of a given type) q/m is fixed at a given mass. So (with a small spread) there is only one velocity for a given mass particle, and the highest velocities are associated with the smallest masses. This is shown in figure 1, where data for iron particles accelerated in the machine are given. Note that for a normal dust sample (one which has not been finely graded for particle size) the bulk of the population is at high mass, and hence low velocity. Figure 1 shows that the typical mass range for iron particles is 10^{-13} to 10^{-16} kg, with corresponding velocities 1 to 25 km/s. Iron is typically used in the accelerator, but other conducting materials can be used as required. Indeed, non-conducting materials can also be used, provided they can be coated with a conducting surface.

The accelerated particles (the flux above 1 km/s is typically 5 or so per minute) leave the Van de Graaff as a beam with diameter of up to 2 cm. Some dispersion of the beam is present, and typically represents a maximum opening angle to the beam axis of tan(theta) = 1/250. In part this can be controlled by the focusing element mentioned above.

In order to improve the understanding of the machine and ensure better operator control, a new top terminal monitoring system is currently being installed (Summer 1993). This consists of a programmable circuit board mounted on the top terminal. Via ADC's it can sample up to 8 inputs at a frequency of 15 kHz. Since the top terminal cannot be directly linked to earth via an electric cable, this monitor is read out via a fibre optic link connected to the base (earth) of the machine. Circuits to convert the electrical signals to light pulses (and

vice versa) are included at both ends of the cable. This permits a two way data flow. Voltages of components inside the top terminal are to be monitored, as is the voltage of the focus element and the temperature. Control of the system is via a microcomputer used by the machine operator.

The user area consists of three main elements linked by 6 cm diameter stainless steel tubes. Any or all of these main components may be present at one time. The first component is a stainless steel 'pot' (a cylinder of height 50 cm and diameter 30 cm). This is equipped with high vacuum flanges with electrical feedthroughs and view ports. It is positioned in the beam line with the cylinder's main axis vertical. It contains a stage, which can be moved vertically over a distance of 10 cm by an external crank. This is in the process of being changed, so that the new stage will be motorized, being capable of 10 cm movement vertically and 10 cm horizontally along an axis perpendicular to the beam. A motorized rotatable small stage will be mountable on the main stage if required. This system will be driven by the operator from a touch panel, and the position will be continually monitored, with the information available to the user. This should be installed and operational by end September 1993.

The 'pot' is used as close to the accelerator as possible, and is connected to it via a T shaped beam pipe. The extra outlet from the T junction leads to an oil diffusion pump which provides a vacuum of 10^{-6} mbar in both the accelerator flight tube and the 'pot'.

The second main component is a velocity selection unit. This has four parts. The first is inserted in the beam pipe. It consists of three tubes positioned sequentially along the beam axis. They serve as pickups when a charged particle passes through them. The induced charge is amplified by an Ortec charge sensitive amplifier (type 142A). The first and third tubes are 10 cm apart, and give signals, the leading edges of which serve to provide the timing information necessary for determining the velocity. The central tube is used to provide an accurate charge measurement (necessary when combined with the velocity to obtain the particle mass). The second element of this system is the hardwired electronics which takes the signals, looks for a leading edge above a threshold on the first and third signals and finds their time separation in units of 20 ns. This is then compared to a preset velocity window and a yes/no decision and the particle velocity and charge are then available on outputs. The third element is simply a 50 cm long tube, which serves to introduce a particle flight time sufficient to permit the electronics to reach a decision. The final element is a coffin shaped box, 165 cm long, 13 cm high and a maximum of 56 cm wide. An oil diffusion pump is mounted on the coffin to provide an interior vacuum of 10^{-6} mbar. The coffin contains two pairs of kicker plates which can be charged and discharged to deflect the beam particle. This system operates in two modes. The first is to keep the plates charged, and to

discharge them if the particle's velocity is acceptable (i.e the chosen particles suffer no deflection and travel straight through the system). The second method is to charge the plates only when a particle is selected and to deflect it a fixed amount into a new, off axis, beam line.

The final user component normally present is a large stainless steel 'churn'. This is a cylinder 2 m long, with a diameter of 1 m. It is positioned so that the main (2 m) axis is horizontal and perpendicular to the beam direction. It is equipped with view ports and high vacuum flanges with electrical feedthroughs. The vacuum is suppled by an oil diffusion pump mounted directly on the churn, giving a vacuum of 10^{-6} mbar. It is planned to replace this pump with a new cryopump. This will provide a vacuum of at least 10^{-7} mbar, and which, locally, should be free of any contaminating oil vapour. To reduce oil contamination from the rest of the system, a turbo-molecular pump will be mounted on the beam line just before the churn to provide an isolating vacuum region of at least 10^{-8} mbar. The specification for the cryopump has an over-capacity on the gas compressor, so that extra cold heads can eventually be installed to replace the other oil diffusion pumps in the experimental area.

Other improvements to the user area are also under way. A new more compact velocity selection system is being designed and built. The coffin will be replaced with a tube of length 50 cm, and diameter of 10 cm (slightly larger than the normal beam tubes). This will contain one pair of kicker plates of 35 cm length. This is under construction. The three element charge pickup will be replaced by a new two element device. The central element of the previous device is removed, and the last element used to provide not only a timing signal but also the measure of the charge. Again this is under construction. A new electronic decision making circuit is being designed and should make the system more flexible.

Beam position monitors are also being installed. These consist of parallel plates followed by a conducting tube, all inserted into the beam line. In each pair of plates, one is earthed and the other read out via an Ortec charge sensitive amplifier. The passage of a charged particle between the parallel plates produces an output signal whose magnitude is dependent on the particle's charge (measured by the tube) and its relative distance between the plates. The calibration of this is achieved by collimating the beam so that it passes along a known path between the plates, the resulting signals then being studied. This is checked by a calculation of the expected induced charge on the plates. One device, consisting of two pairs of parallel plates (the second pair rotated by 90 degrees around the beam relative to the first) has already been installed and calibrated. It provides position information on the location of a particle in two axes perpendicular to the beam direction good to 1 mm. Refinements in the calibration method are hoped to improve this. Two more such devices are being constructed.

One feature of these beam monitors is that the signals are read out not just on an oscillosope, but also into an IBM 486 compatible personal computer. The data acquisition system used is a software package from National Instruments called LABVIEW [4]. This is interfaced either directly to the data (via a standard DAQ board) or to the oscillosope (via an IEEE 488.2 standard GPIB board). The user writes his own application program using the LABVIEW software and can not only acquire the data (and store on 3.5 inch disk) but also display and analyse on-line. Thus in a time of order 1 sec after acquisition the x,y coordinates are available (as is a measure of the velocity). The LABVIEW language is not a text based system, rather it is symbolic, using icons and circuit drawing tools to permit operations upon the data similar to that which would occur in a hardwired electronic circuit.

3. Experimental Programs Using the Van de Graaff Accelerator

The Van de Graaff has been used for many years to support the activities of the Unit for Space Sciences at Kent. During the 1980's, data from the machine was used in the calibration or interpretation of data from the Space Shuttle STS-3 microabrasion foil experiment, the Long Duration Exposure Facility (LDEF) microabrasion foil experiment, the Giotto Dust Impact Detector System and Particulate Impact Analyser and for prototype work for several other projects. The recently retrieved ESA satellite EuReCa, carried an experiment (TICCE) built at Kent, the analysis of data from which will owe much to studies made using the accelerator. Indeed, the studies of thin foil penetration, and crater size and depth in semi-infinite (thick) targets which has been carried out at Kent has been widely published and used (e.g. [5]).

Similar programs of work are continuing. As is work studying the impact processes themselves, and comparing the results with the predictions of calculations. In particular, plasma production, the role of ejecta, the influence of oblique angle impacts and the energy partitioning occuring during impacts are all being studied.

Current detector work includes the design and testing of the Cosmic Dust Analyser [6] for the Cassini/Huygens mission to Saturn and its moons, scheduled for launch in October 1997. This is an elaboration of the dust detectors on the Ulysses and Galileo missions now operational [7]. The detector is an ionization sensing device. A schematic is shown in figure 2. The dust enters through the grids at the top of the device. Any charge is detected as a pulse in the electronics connected to the grids. The dust particle then impacts an ionization target (a curved surface made of gold) or a chemical analyzer target (a curved surface made of rhodium). The ions liberated in the impact are attracted to an ion detector (a discrete dynode electron multiplier) mounted at the focus of the curved surfaces. Over the 3 mm just above the chemical analyzer target surface an intense field of 1 kV is applied.

There is a further potential difference of 350 V between the entire target surface and the ion detector. For the chemical analyzer this combination is sufficient to make any initial ion momentum negligible, thus permitting a chemical decompostion of the ions by the time of flight method. After subtraction of the target contribution, the remaining chemical species present are a measure of the dust particle's composition. Due to the high field and small drift length, a fast digitization of the signal from the ion detector is required. A 100 MHz system is under separate development at the Rutherford Appleton Laboratory (UK). The incident particle velocity is found by one of several methods (listed in decreasing accuracy). If there is sufficient charge the shape of the pulse on the entrance grids yields the velocity. Next, if the particle impacts the ionization target (figure 2) the rise time of the pulses on the target and ion collector give the velocity. If the particle hits the chemical analyser, the rise time of the signal is too fast to give the velocity, however there is a broadening of the signals in the mass spectrum which can give velocity to a factor of two. The particle mass is found from the total ion yield, since this has been shown to be proportional to mass for a given velocity [6].

That the detector design was feasible was demonstrated with a prototype used in the Van de Graaff accelerator in 1989-1990. A typical mass spectrum is shown in figure 3. This was for an iron particle (25 km/s) impacting on an aluminium target doped with silver. Since the velocity and mass are independently measured for accelerated particles, the calibration of the detector for measuring these quantities can also be obtained. Testing and calibration of the project laboratory model of the detector is scheduled to take place during late 1993.

A new project which will shortly start to make use of the accelerator, is a proposal to construct a dust flux analyser for the Pakistani satellite Badr-B. This is scheduled for launch in December 1994. It is proposed to include on the satellite a plate for detecting dust impact. This will be multiply instrumented, including PVDF coatings which when penetrated are locally depolarized, producing a signal proportional to the incident kinetic energy. Piezoelectric Zirconium Titanate sensors and Lead Zirconite transducers will also be present, allowing both a confirmation of the impact and, by arranging several sensors on the plate, the relative timing of the signals will permit a position determination for the impact. This concept will be tested in the accelerator, making particular use of the new motor driven stage and beam position monitors. Although, the piezoceramic sensors require a relatively large mass impact to be fully sensitive, sufficient masses can be accelerated to make calibration and testing practical.

A separate program of work is also planned to observe the degree of degradation of optical surfaces after exposure to the micrometeroid population in earth orbit. This will involve use of both the accelerator and the light gas gun below.

4 Light Gas Gun

The Light Gas Gun was installed at Kent in 1989, and has since undergone development. It is approximately 6 m in length. At one end is a gun, firing a 32 g cartridge (diameter 2 cm). The volume of powder is typically 10 to 13 g. The expanding combustion gases causes a piston to advance down a shaft, compressing a chamber of hydrogen gas (initially at 40 bar). At the far end of this chamber is a pressure sensitive disc, which ruptures when a sufficient pressure has been reached. This then permits the acceleration of a nylon sabot (a cylinder 4 mm long, 4 mm diameter and mass of 80 milligrams). This can serve as the projectile and reaches velocites of up to 5.45 km/s. Alternatively it can be pre-cut and loaded with a chosen projectile. In this case, due to rifling in the barrel down which it initially travels, plus the cuts, the sabot is discarded and flies away from the projectile leaving it free to fly to the target by itself.

During the sabot's (or projectile's) flight its velocity is measured by the time interval between its passage through two light curtains These are from white light sources mounted perpendicular to the direction of flight, and are 50.5 cm apart. The flight through a curtain is detected from light scattered into a photomultiplier tube positioned perpendicular to the flight direction and at 90 degrees to the light source.

The target is mounted in a target chamber at the far end of the system. A target diameter of 10 cm can be accommodated. This chamber (as is all the system after the rupture disk) is pumped by a rotary pump to a minimum vacuum of 10^{-3} mbar.

The gun may be fired approximately once per day.

5. Light Gas Gun Experimental Program

The gun is being used for a variety of programs. Chief amongst these are studies of crater shape (in particular ellipticity and depth variations across the crater) for oblique impacts. The distribution (in both direction and mass) of ejecta is also being studied. Both these projects use the 80 milligram nylon sabot as the projectile. Recent firing of the gun for this work has consistently attained velocities of around 5 km/s, with the highest reliably recorded velocity being 5.45 km/s.

A separate project is underway where the sabot is loaded with small glass beads. The sabot has been successfully discarded in flight and a sample target bombarded with a cloud of the beads. These beads are typically around 50 to 200 microns in diameter (and thus mass ranges from 10^{-9} to a few 10^{-7} kg). It is clear that masses greater than those obtainable in the Van de Graaff machine are being accelerated. Fine grading of the beads by size will be carried out during the full program of work to produce impacts of just a limited mass range on each target. The targets to be used correspond to materials flown on previous space

flights, where interpreting the data has proved difficult due to suspect or questionable calibrations. Thus it is hoped to recalibrate the results of micrometeroid fluxes from past experiments, to check the results and to increase the size of usable data sets in such studies.

6. Conclusion

The hypervelocity impact (simulation) facilities of the Unit for Space Sciences at the Univ. of Kent (UK) have been described. Their main features have been given, along with indications of their typical performance and the use to which they are put. Although the internal program of work is a vigourous one, care is taken to ensure that, where possible, time is made available to external collaborators or to groups who wish to visit. This is essential given the limited number of such facilities.

References
[1] Fechtig H. et al. (1972), Naturwiss, 59, 151.
[2] Keaton P.W. et al. (1990), Int. J. Impact Engng, 10, 295-308.
[3] Green S.F. et al. (1988), Journ. British Interplanetary Soc., 41, 393.
[4] LABVIEW, a product of National Instruments. Contact the local sales office for details.
[5] McDonnell J.A.M. and Sullivan K. (1992), proc. of Hypervelocity Impacts in Space, ed J.A.M.McDonnell, pub Univ. of Kent, pp 39-47.
[6] Ratcliff P.R. et al. (1992), Journ. Brit. Interplanetary. Soc. 45, 375.
[7] Göller J.R. and E.Grün E. (1989), Planet. Space Sci., 37, 1197-1206.

Figure Captions

Figure 1: Measured Mass versus Velocity for iron particles accelerated in the 2 MV Van de Graaff Facility.

Figure 2: Schematic of the Cassini Cosmic Dust Analyser and representation of signals obtained [6].

Figure 3: Mass spectrum obtained by the Cosmic Dust Analyser for an iron particle impacting at 25 km/s a silver doped aluminium target [6].
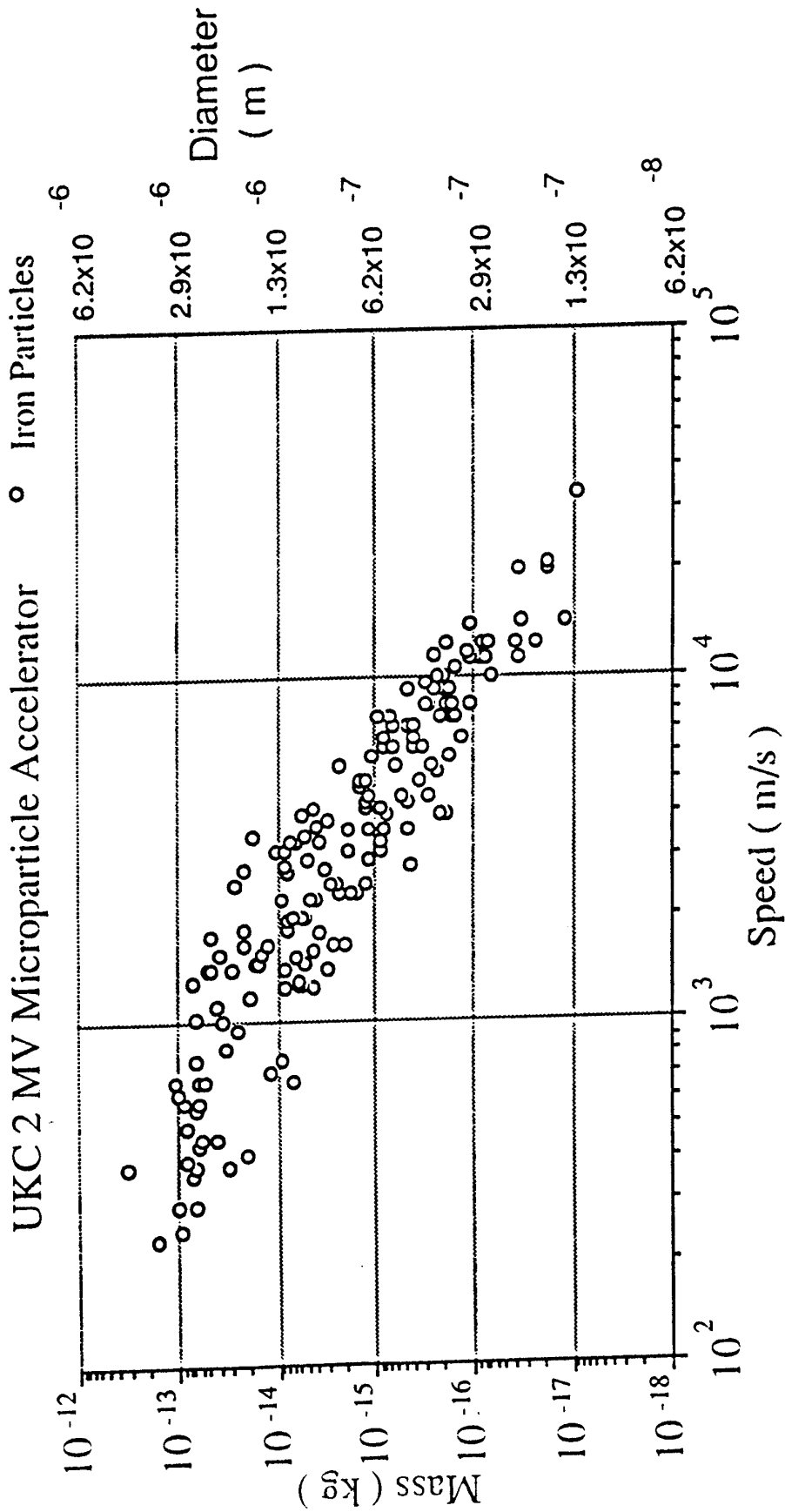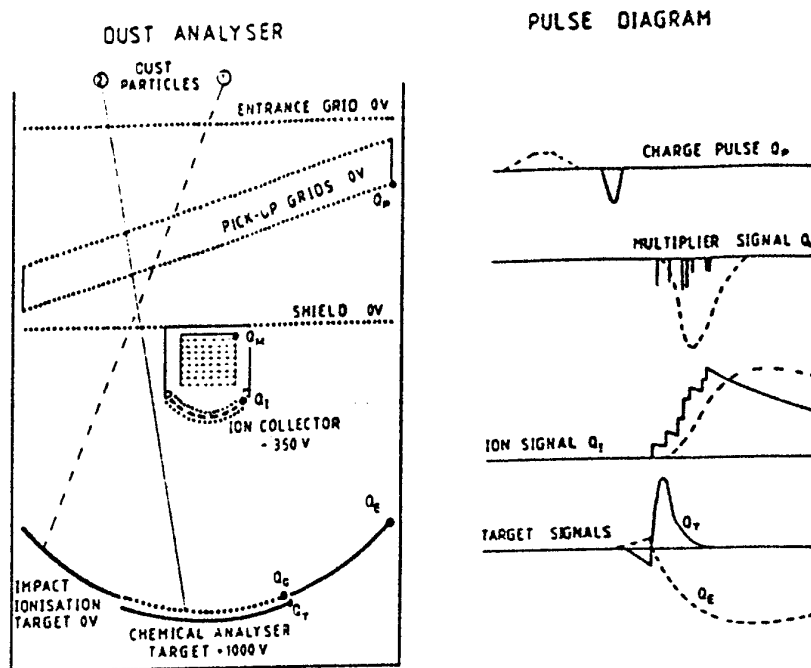
Figure 1: Velocity vs Mass (observed) for iron particles accelerated in the 2 MV machine

DUST ANALYSER

PULSE DIAGRAM

Figure 2: Schematic of the Cassini Cosmic Dust Analyser and representation of signals obtained [6].
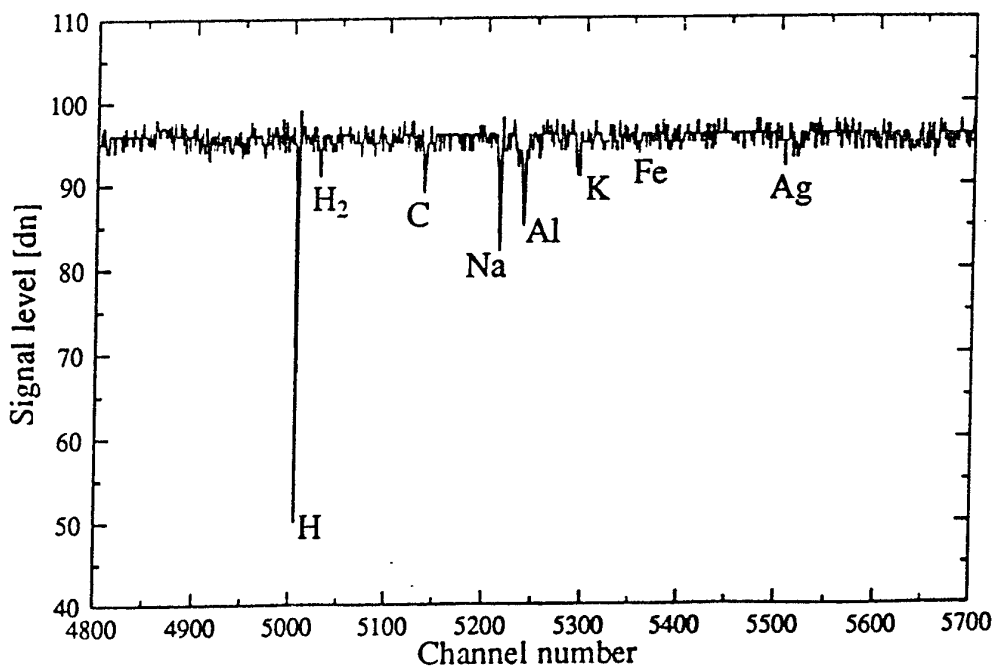

Figure 3: Mass spectrum obtained by the Cosmic Dust Analyser for an iron particle impacting at 25 km/s a silver doped aluminium target [6].